University of Southampton

Faculty of Physical Sciences and Engineering

Optoelectronics Research Centre

Coherent all-optical signal processing using fibre-optic metadevices

by

Angelos Xomalis

ORCID ID 0000-0001-8406-9571

Thesis for the degree of Doctor of Philosophy

May 2019

University of Southampton

Abstract

Faculty of Physical Sciences and Engineering

Optoelectronics Research Centre

Thesis for the degree of Doctor of Philosophy

Coherent all-optical signal processing using fibre-optic metadevices

by Angelos Xomalis

This Thesis merges the physics of metamaterials with optical fibre technology in order to demonstrate low-power, high-bandwidth signal processing applications. Control over optical absorption using linear coherent interactions of light beams with metasurfaces of deeply subwavelength thickness offers a range of novel opportunities. Here I report on:

- The first demonstration of a **fibre-optic metadevice for coherent all-optical signal processing**. The fibre metamaterial has been integrated and packaged resulting in a device that is compatible with standard fibre-optics components.

- **All-optical signal switching, effective nonlinearity and logical functions XOR, NOT and AND** performed within a coherent fibre network at wavelengths between 1530 and 1565 nm. The metadevice has been tested at up to **40 Gbit/s with energy consumption as low as 2.5 fJ/bit**.

- **Dark pulse generation, selective transmission/absorption of 1 ps pulses and all-optical pulse shaping** in the telecommunications C-band with **1 THz bandwidth in-fibre**.

- The first demonstration of a fibre-optic plasmonic/metamaterial device for **data security applications**. I introduced the **concept of coherent cryptography, an optical layer secure communication protocol** that does not rely on nonlinear optical processes but instead uses energy redistribution of coherent optical waves interacting on a metamaterial absorber. I demonstrated different types of **encryption modes and reported a scheme providing perfect secrecy**.

- **Nonlinear control of coherent absorption** in a nonlinear fibre network containing a metamaterial absorber. I exploited power-dependent phase retardation arising from the Kerr effect for **all-optical noise suppression, power-limiting, pulse restoration, pulse splitting and signal transfer between carrier wavelengths**.

In addition, I have **developed and fabricated fibre metadevices**, which have enabled:

- The first demonstration of **coherent perfect absorption and transmission for a single photons in a stabilized quantum fibre network** by collaborators.

To conclude, this Thesis investigates all-optical solutions provided by plasmonic metamaterials for coherent signal processing within fibre networks. The above proof-of-principle demonstrations show the appropriateness of such metasurfaces for fibre integration and illustrate application opportunities ranging from all-optical switching and pulse shaping to optical encoding and stabilization of fibre-optic classical and quantum information networks.

Table of Contents

Table of Contents

Table of Contents

Research Thesis: Declaration of Authorship

Print name:	Angelos Xomalis

Title of thesis:	Coherent all-optical signal processing using fibre-optic metadevices

I declare that this thesis and the work presented in it are my own and has been generated by me as the result of my own original research.

I confirm that:

1. This work was done wholly or mainly while in candidature for a research degree at this University;
2. Where any part of this thesis has previously been submitted for a degree or any other qualification at this University or any other institution, this has been clearly stated;
3. Where I have consulted the published work of others, this is always clearly attributed;
4. Where I have quoted from the work of others, the source is always given. With the exception of such quotations, this thesis is entirely my own work;
5. I have acknowledged all main sources of help;
6. Where the thesis is based on work done by myself jointly with others, I have made clear exactly what was done by others and what I have contributed myself;
7. Parts of this work have been published as journal papers and conference contributions listed in Appendix C.

Signature:	Angelos Xomalis	Date:	07/10/19

Acknowledgements

A PhD cannot be completed without help and support of other people. For all the scientific achievements reported here I would like to acknowledge their contribution, namely:

- Prof. Nikolay I. Zheludev and Dr. Eric Plum for the guidance and mentoring through the course of my PhD. More specifically, Prof. Zheludev for the scientific debates and Dr. Plum for the hours that he devoted to read my drafts and Thesis.
- Dr. Yongmin Jung for his valuable help and advice on metamaterial encapsulation. I am also grateful to Prof. Periklis Petropoulos and Prof. David J. Richardson for the guidance from telecommunications perspective and Iosif Demirtzioglou and Dr. Cosimo Lacava for the assistance they offered with all the telecommunications equipment.
- Dr. Anton Vetlugin, Salih Yanikgonul and Dr. Ruixiang Guo my collaborators at Nanyang Technological University in Singapore for pushing our technology down to the quantum regime.
- My parents, who unconditionally supported me in all scientific steps and for their love.
- Elena my loving partner, for her support and patience when I came home ridiculous hours.
- All other friends and colleagues for the time spent together.

Support from UK's Engineering and Physical Sciences Research Council (EPSRC) through the grant EP/M009122/1 is gratefully acknowledged.

Chapter 1 Introduction

1.1 Motivation and outline of the thesis

For almost twenty years metamaterials' research field revealed continuous breakthroughs and new exotic physical phenomena based on light manipulation [1-5]. Although, metamaterials have poor implementation to real life applications mainly because of their fragile geometry and small structure footprint. Thus, the necessity for bringing metamaterials with mature and established technologies seems imperative and it is the logical direction for its research community.

The aim of this thesis is to establish the knowhow for merging metamaterials and fibre technology. The motivation for this attempt is the wide use of optical fibres in today's communications. Optical fibres provide the fastest transmission of optical signals with the ultimate speed of light. This thesis presents, for the first time, fibre-integrated metamaterials that are compatible with standard fibre optic networks which are used in real life communications. The operation principle lies on linear interaction of light beams with strong phase correlation in ultrathin films resulting in all-optical signal processing and does not require conversion between optical and electronic signals that leads to speed limitations. Most importantly, the temporal bandwidth limitation of such metamaterials devices (metadevices) depends only on the quality factor of their resonance which can be engineered accordingly in order to reach tens of THz.

Energy sustainable technologies need devices with low power consumption in order to be truly efficient. For optical based approaches the lowest possible optical intensity is single photon level. This thesis presents metamaterial fibre devices that can perform all-optical signal processing functions with single photons. Such intensity levels are not compatible with any other signal processing schemes e.g. using nonlinearities. Furthermore, all-optical control of absorption showing that the transition from classical to quantum light does not affect the operation of the fibre integrated metamaterials.

Consequently, this thesis reports on fibre encapsulated devices that can operate with THz bandwidth and single photon signals. In details, the layout of the thesis is as follows:

Chapter 1 gives an introduction regarding the aim and the motivation of the thesis and introduces basic principles that are mainly used in the following chapters. Chapter 2 explains the mathematics of two wave interference, the importance of ideal optical parameters for efficient light manipulation and gives a detailed description of the fabrication and encapsulation of the fibre metamaterials. Chapter 3 reports on the first experimental observation of coherent control of optical absorption in fibre networks and all-optical signal processing based on logic functions at rates of tens of Gbit/s and with fJ/bit energy consumption. Chapter 4 explains the fundamental limitations of pulse propagation in terms of dispersion and nonlinear effects in fibre networks, shows all-optical switching at 1Tbit/s and presents an efficient way for dark pulse generation and pulse shaping. In Chapter 5, I introduce an all-optical encryption protocol based on dissipative metamaterial gates for secure communication. Furthermore, I discuss the implementation in fibre networks, challenges and advantages of the encryption protocol. Chapter 6 explores intensity dependent phase that derives from a nonlinear Kerr medium to control absorption in ultrathin plasmonic films for pulse cleaning and wavelength conversion applications. Chapter 7 investigates the potential of our platform for quantum all-optical switching and signal processing applications. Furthermore, this chapter proves that the fibre encapsulated metadevices can operate with quantum as good as with classical light without having limitations due to losses. Finally, Chapter 8 summarises the work presented in all previous chapters and proposes ideas for new fibre integrated metadevices based on multi-fibre and multicore fibre assembles for all-optical signal processing within multiple channels .

1.2 Basic principles

1.2.1 Metamaterials

Metamaterials are artificial materials for manipulation of waves. They derive novel or enhanced properties from structuring on the sub-wavelength scale. Thus, the metamaterial does not diffract and shows a homogenous response, different from its constituent materials and often going beyond the range of properties available in natural materials. Its name is derived from the Greek word μετά = *meta*, meaning "beyond", i.e. beyond-materials. Here we focus on electromagnetic waves and thus a homogenous response usually refers to homogenous electric permittivity (ϵ_{eff}) and magnetic permeability (μ_{eff}). It was first proposed by V. Veselago [6] at the end of 70's, as a theoretical concept only, that the above-mentioned values can be negative. Negative values of ε and μ lead to a negative refractive index (n), $n = (\varepsilon\mu)^{1/2}$.

For about three decades, the idea of media with negative ε and μ, and moreover, with negative n was sidelined. Until the breakthrough, an experiment by D. R. Smith [7] and colleagues, proved the experimental realization of negative n at microwave frequencies (see Figure 1-1). After that, many experiments and theoretical studies on metamaterials followed. Metamaterials meaning comprises not only negative-index materials but also manmade media with all sorts of other unusual functionalities that can be achieved by artificial structuring with a unit cell smaller than the wavelength of the external stimulus [8]. These considerations introduced metamaterials as a broad research field with huge potential for applications in many different scientific disciplines. An important contribution by J. B. Pendry introduced a way to create artificial magnetism with metamaterials [9]. Artificial magnetism is widely used in magnetic resonance imaging and spectroscopy systems. Moreover, metamaterials have enabled the observation of a plethora of exotic phenomena such as negative refraction [10], perfect lensing [11], optical cloaking [12, 13], directionally asymmetric transmission [14, 15], optical nonlinearities [16], magnetic mirrors [17] and many others.

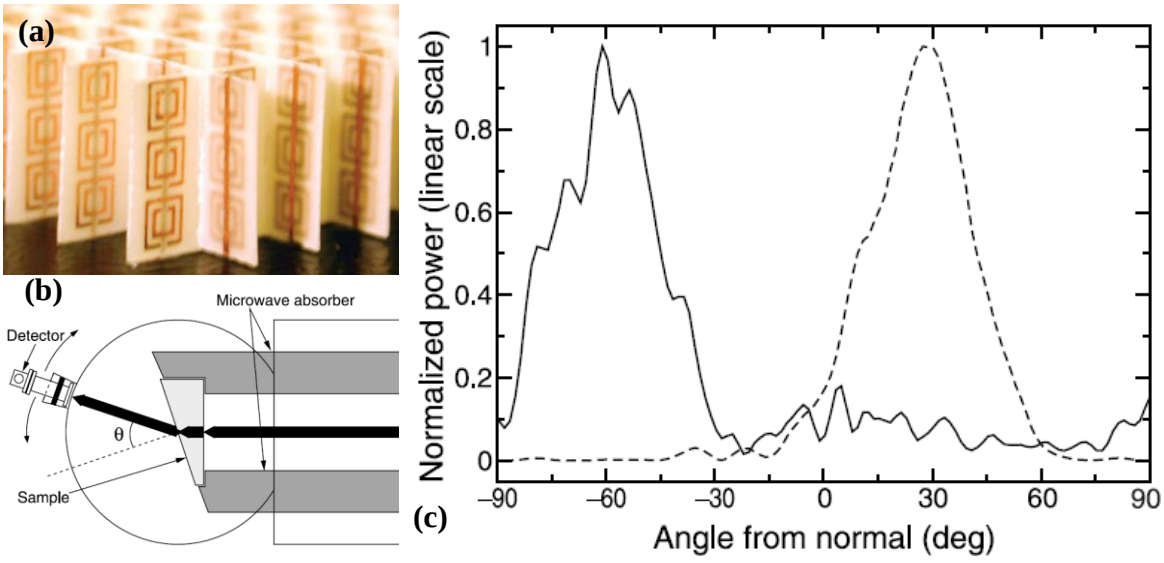

Figure 1-1 **First demonstration of negative refraction.** (a) The metamaterial structure that exhibits negative refraction. The unit cell consists of three main components: a split ring resonator, a wire strip and the substrate made of fiber glass board. (b) The experimental setup: a reference sample (light grey) refracts (black arrow) as positive index material. The detector can rotate around the sample in order to collect both positive and negative refraction. (c) The graph shows the transmitted power versus the refraction angle. The dashed line shows the response of the positive index reference material (teflon). The solid line shows the metamaterial response and, for the first time, the existence of negative refraction [7]. Figures **a**, **b** and **c** adapted from Ref. [7].

The next chapters mainly focus on two-dimensional metamaterials, also known as metasurfaces. There are - typically metallic - thin films, which are structured on the sub-wavelength scale and that are thin in comparison to the operational wavelength. Metasurfaces are important in the present project as they allow the realization of non-diffracting thin films with precisely engineered transmission, reflection and absorption characteristics.

1.2.2 From metamaterials to metadevices

A logical extension of metamaterials is metadevices. Metadevices concern metamaterials beyond a structure with fixed properties (e.g. negative refractive index). Metadevices are metamaterials that have dynamically controllable characteristics such as switchable and tunable optical properties. One can categorize such metadevices based on their operation principle.

Phase change metadevices: These exploit transitions between different structural phases of constituent materials to switch between different metamaterial properties. Examples include use of vanadium dioxide [18] and chalcogenide materials. Vanadium dioxide transitions between dielectric and metallic phases upon heating. Chalcogenide glasses are alloys of sulfur (S), selenium (Se) and tellurium (Te), mixed or bi-layered with other materials such as gallium (Ga), antimony (Sb), lanthanum (La), aluminium (Al), gold (Au) and others. Chalcogenides are known for their optical nonlinearities as well as for infrared transparency but more importantly for non-volatile switching between amorphous and crystalline states, where they have very different electronic and optical properties, with applications in rewritable optical disks i.e. CD-RW and DVD-RW. The switching between amorphous (high reflectivity and resistivity) and crystalline (low reflectivity and resistivity) states can be optically [19] (Figure 2-1 (a-b)), electrically [20] (Figure 2-1(c)) and thermally [21] (Figure 2-1(d)) induced. The first example concerns all-optical switching with pulses of different duration. Transition from crystalline to amorphous is a melt quenching process, thus a short pulse heats the material above the melting point then rapid cooling traps it in the amorphous state. The reverse step, the amorphous to crystalline transition, is an annealing process and thus a longer pulse of lower intensity is required. In this way, the material is heated above the glass transition but below the melting temperature and allowed to recover to the crystalline phase.

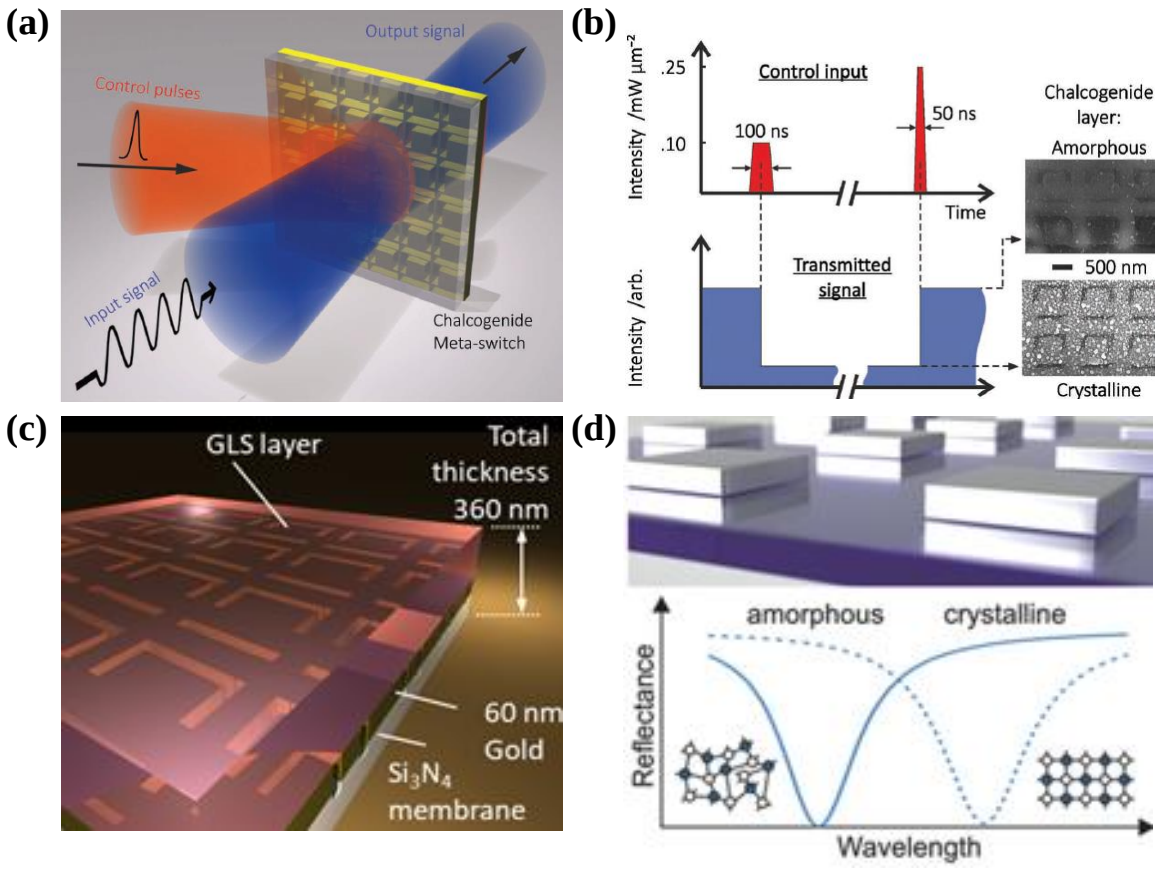

Figure 1-2 **Phase change hybrid plasmonic metadevices.** **(a)** An all-optical and non-volatile, hybrid chalcogenide glass-Au metamaterial switch. **(b)** Laser pulses of different duration convert a chalcogenide phase-change layer back and forth between amorphous and crystalline states [19]. **(c)** A metadevice switch based on electrically induced phase transition. The metadevice is a multilayer of Au metamaterial on a silicon nitride membrane, covered with GLS (gallium lanthanum sulphide) chalcogenide glass [20]. **(d)** Top: A switchable mid-infrared plasmonic absorber. Al nanoantennas are stacked above a spacer layer of the phase change GST (germanium antimony telluride) material, and an Al mirror. Bottom: Experimental measurements show that the amorphous to crystalline heat-induced phase transition in GST provide strong reflectance contrast at resonance [21]. Figures **a** and **b** adapted from Ref. [19]. Figures **c** and **d** adapted from Ref. [20] and Ref. [21], respectively.

The above-mentioned metadevices are plasmonic-chalcogenide hybrids, which have a number of drawbacks such as absorption losses in the metallic component, in the optical domain, and unwanted chemical interactions between the two layers (unless a buffer medium

used in between). Thus, the community shifted to exploration for other structure schemes i.e. all-dielectric chalcogenide metadevices [22].

Reconfigurable metadevices: Such metadevices change their optical response (i.e. light transmission) after nanomechanical structural reconfiguration of their unit cells. In the THz part of the spectrum one can achieve such reconfiguration using microelectromechanical systems (MEMS). As one pursues such response in the optical part of the spectrum where the unit cell size shrinks to hundreds of nm, this requires high level fabrication processes. With the decrease in the physical dimensions of a system, the electromagnetic forces between constituent elements grow, as illustrated by the repulsive force between electrons as their separation diminishes [23]. In the nanoscale, forces such as Ampere, Coulomb, Lorentz and optical forces become comparable to elastic restoring forces that occur in nanostructures when deforming them at nm scale. Therefore structural reconfiguration of appropriately designed photonic metamaterials can be induced by thermal [24], electrostatic [25], magnetic [26] and optical [27] control signals, see Figure 1-3(a-d).

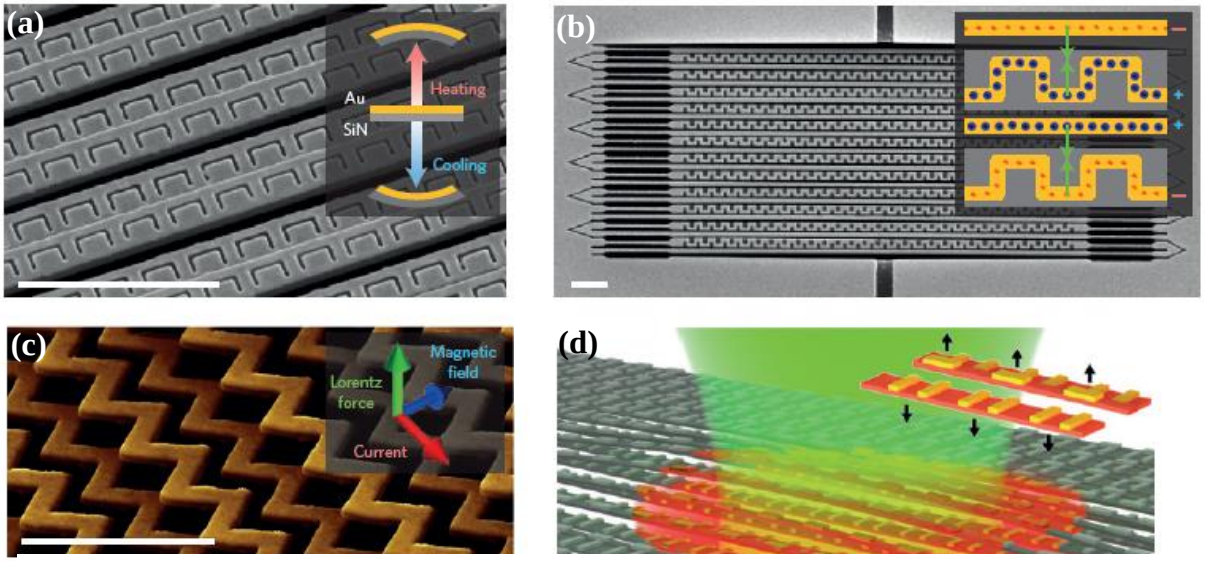

Figure 1-3 **Reconfigurable nanomembrane metadevices.** **(a)** A thermally reconfigurable metadevice based on different thermal expansion coefficients between metal (Au) and silicon nitride layers [24]. **(b)** A metadevice driven by electrostatic forces (green arrows) between oppositely charged nanowires can act as electro-optic modulator [25]. **(c)** A nanowire metadevice driven by the Lorentz force that is controlled by currents and magnetic field can act as magneto-optic modulator [26]. **(d)** A plasmonic metadevice actuated by light acts as all-optical modulator. A pump beam (red) reconfigures the nanostructure (inset) resulting in modulation of a probe beam (green) [27]. Scale bars in (a), (b) and (c) are 2 μm long. Figures **a**, **b**, **c** and **d** adapted from Ref. [24], Ref. [25], Ref. [26] and Ref. [27], respectively.

Liquid crystal metadevices: This category merges the physics of resonant nanostructures with the tuneable optical properties of nematic liquid crystals (LC). The optical properties of LC can differ significantly when switched from isotropic to nematic phase. LC molecules can change their orientation under the presence of external electric fields [this is how LC displays (LCD) work], see Figure 1-4 (a), and can act as polarizers. It is known that many metamaterial structures exhibit different optical responses for light with different polarization states (Figure 1-4(b)). More specifically, light with resonant incident wavelength and polarization (polarization that couples to the plasmonic mode), will be strongly attenuated, see Figure 1-4(b) upper panel [28]. On the contrary, incident light will be mostly transmitted for the other polarization state since it is non-resonant. The effect of the orientation of LC molecules is scalable, see Figure 1-4(b) bottom panel. One can see that for different applied voltages the LC molecules respond differently up to a saturation threshold (where the molecules are fully aligned). Thus, the multilayer hybrid metadevice can act as an electro-optic modulator where for higher voltages the LC molecules will deliver more light of the absorbed resonant polarization to the metamaterial. Moreover, the presence of the LC within metamaterials can change or modulate the effective refractive index (Figure 1-4(c)), due to molecular re-orientation caused by constant or time-variant external electric field. Consequently, the resonance frequency of the metadevice can be shifted (see Figure 1-4(d)) [29].

Multilayer hybrid and reconfigurable metadevices promise efficient light manipulation but exhibit limited modulation speed. Their operation principle based on either material's phase transition/molecular re-orientation or reconfiguration of the unit cell (as discussed above) cannot deliver truly ultrafast switching (few GHz in the best case). This Thesis explores the potential of another class of metadevices that uses light to control the interaction of light with a static metasurface. It is truly ultrafast as it does not rely on any change within the metamaterial. The concept may be illustrated for absorption of light. Metasurface absorbers were designed to absorb light for single beam illumination. However, absorption can be made more efficient by exploiting wave interference [30]. Recently, interactions of coherent light beams (see section 1.2.4) with a material (e.g. an absorber) that is thin, relative to the operation wavelength, were shown to be the ideal candidate for ultrafast control of the expression of metasurface properties (such as absorption) [30, 31]. In Chapter 2, we investigated the phenomenon of coherent absorption and its potential for integration with optical fibres resulting in fully-fiberized metadevices.

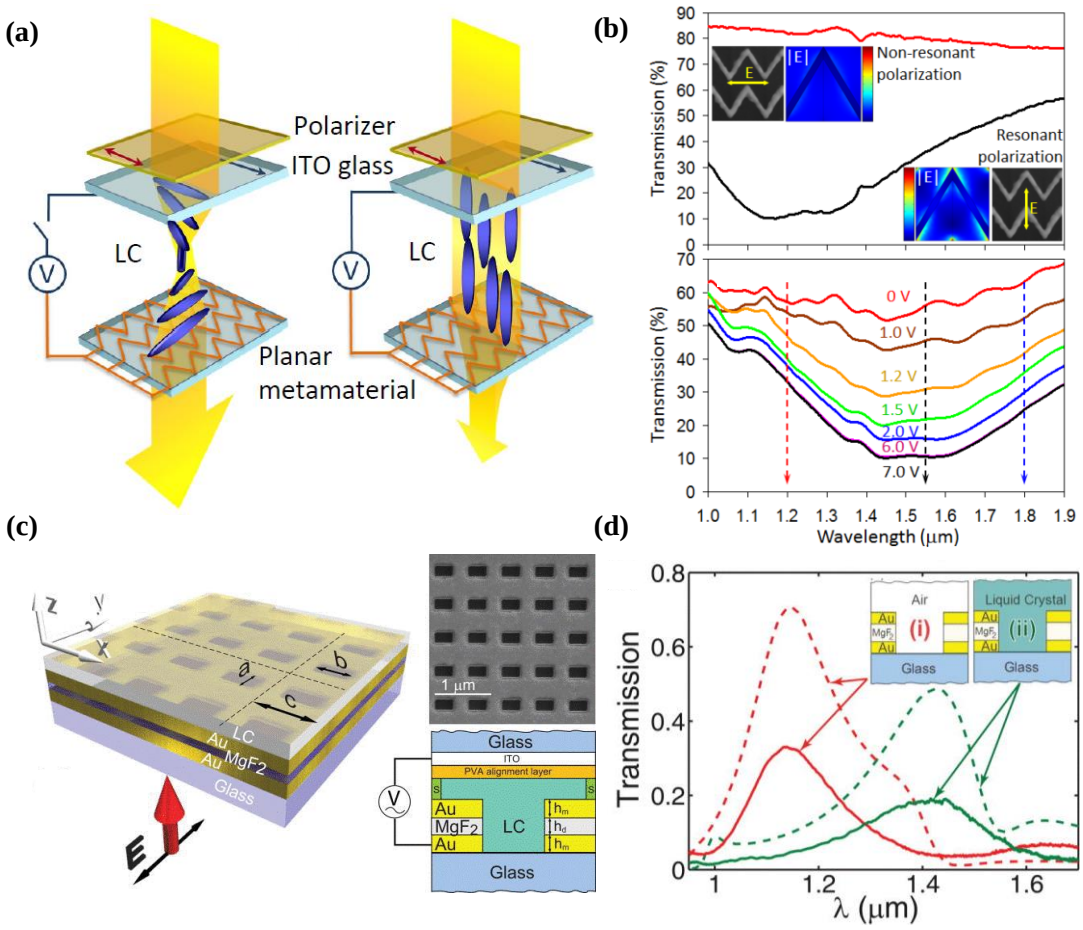

Figure 1-4 **Liquid crystal metadevices. (a)** Left: the hybrid cell in the OFF state. Right: the hybrid cell in the ON state. **(b)** Top: Transmission spectra of bare metamaterial of panel (a). Insets show orientations of resonant and non-resonant polarizations with respect to metamaterial structure and field maps of the corresponding near-field distributions calculated at a wavelength of 1.2 μm. Bottom: Transmission spectra of the metamaterial hybridized with a LC cell measured for resonant polarization under various levels of voltage [28]. **(c)** Left: Schematic of a LC infiltrated fishnet metadevice. Top right: SEM image of the fabricated fishnet metamaterial. Bottom right: Artistic impression of the hybrid metadevice. **(d)** Measurement of linear transmission of the Au-MgF_2-Au cell without (i) and with (ii) LC molecules. Solid and dashed lines correspond to experimental results and numerical simulations, respectively [29]. Figures **a** and **b** adapted from Ref. [28]. Figures **c** and **d** adapted from Ref. [29].

1.2.3 All-optical signal processing

Over the last two decades, great effort has been devoted to the investigation of "photonics circuits" where a light beam can control another light beam. This appears to be the Holy Grail for photonics scientists and engineers since all-optical signal processing promises extremely high signal processing speeds. Control over light with light may result in optical switching, logic gates, signal generation and more. Most of these optical functions are based on Kerr nonlinearity effects such as self- and cross-phase modulation and four-wave mixing (Kerr nonlinearity is discussed in Chapter 6 extensively).

Silicon has a numerous nonlinear characteristics that are based on interactions between incident light and the electrons and phonons in the material. Mainly, silicon is used because of its transparency (low loss) at infrared telecoms wavelengths, low cost and compatibility with CMOS technology rather than strong nonlinear performance.

Moreover, a common device for optical switching is a Mach-Zehnder interferometer, where in one arm of the interferometer a nonlinear element installed. Intense light induces refractive index changes and, consequently, changes the optical path [32]. The light beam experiences a power dependent phase shift resulting in different interference with the light from the other arm. Thereafter, as one increases the optical power it is possible to control the interference pattern of the two light beams (i.e. transition from constructive interference and maximum light transmission to destructive interference and minimum light transmission and vice versa). Common all-optical signal processing devices are silicon based waveguides that can achieve a π phase shift (common level of phase needed by electro-optic modulators) within short lengths and with reasonable losses [33]. The size of the waveguide plays crucial role in the magnitude of nonlinearity. As the effective mode area decreases (thus the light confinement increases) the nonlinear coefficient of the waveguide increases (see Chapter 6). Recent developments in nanofabrication allow the fabrication of such highly nonlinear waveguide devices.

In "photonic circuits" the information stored in light signals needs to be transmitted, processed and read. For all-optical signal processing architectures, logic gates may be an ideal platform for information processing. Here, input light beams interact within a medium that has power-dependent properties (nonlinear medium). In interferometric setups, one can

adjust phase and intensity of light in the interferometer arms resulting in interferometer outputs corresponding to several logic functions after interaction with a functional element. For example, one can perform such operations with a silicon micro-ring resonator coupled to straight waveguide [34], where two input "control" pulses coupled synchronously to the ring modify the refractive index at sufficiently high optical power. Thus, a CW "probe/signal" beam can be modulated since the modification of the refractive index shifts the resonant wavelength of the ring. After the pulses leave the ring, the refractive index relaxes back. If the pulses are not synchronized, the power is not sufficient to change the refractive index significantly and the CW beam experiences no modulation. Thereafter, by precise adjustment of the probe wavelength with respect to the ring resonator's resonance it is possible to perform logical functions to the output.

In this thesis, we propose to use plasmonic metasurface absorbers for all-optical signal processing. The main advantage of such metadevices lies in the truly linear nature of interactions of light with light within the absorber that delivers logic operations relying on the coherence of light, rather than nonlinearity. Conventional all-optical signal processing relies on high-intensity pulses in order to activate the material's nonlinearities, thus such existing approaches cannot offer satisfactory power consumption, something that is of vital importance for future telecoms applications. On the contrary, coherent control of light with light can operate with single photon signals [35]. For the realization of real telecom applications the integration with optical fibres that carry telecom signals seems compulsory. Micro-ring resonators and waveguides fabricated on chips require optical signals to be coupled in and out from the chip resulting in substantial coupling losses. On the contrary, metasurfaces are two-dimensional patterns that can be structured directly on the top of cleaved optical fibres and packaged resulting in fully-integrated in-fibre metadevices (see Chapter 2). The metasurfaces contain nanoresonators that exhibit strong light-matter interactions, such that thickness of few tens of nanometres is enough to deliver the desired function. Moreover, such resonators can be designed to operate at any chosen wavelength by adjusting their structural dimensions. Lastly, the operation speed of the device defines the bandwidth of the processing system. The bandwidth of micro-ring resonators is defined by the photon lifetime within the waveguide ($\tau = \frac{Q\lambda}{2\pi c}$, where Q and λ stand for the quality factor and wavelength, respectively) that is on the order of ~ 10 ps [34]. On the other hand, coherent interactions can result in switching of femtosecond pulses offering THz bandwidth [36].

1.2.4 Coherence within local fibre networks

The following chapters of this Thesis comprise experiments that study light-matter interactions within *coherent* fibre information networks. Thus, this section is devoted to the discussion of such coherency between optical signals, propagating within fibre networks, and its importance to the resulting output beams of fibre interferometers that can be modulated, encrypted as well as logic products of input light beams.

There are two classifications of coherence: temporal and spatial. In order to understand what is temporal coherence we need to introduce first the coherence length (L_c), which is the product of speed of light in vacuum and coherence time (τ_{coh}). Coherence time is the temporal interval over which we can reasonably predict the phase of a lightwave at a given point [37]. In laser physics and optical communications often L_c can be found as:

$$L_c = c\,\tau_{coh} = \frac{c}{\pi\,\Delta v},$$

where Δv is the linewidth (full width at half-maximum) or optical bandwidth of a light source. Coherence length is the length over which the light beam is nicely sinusoidal so that its phase can be predicted reliably. If τ_{coh} is large or Δv is low (around kHz) the optical wave (laser beam) has a high degree of temporal coherence.

In this thesis, the phrase “mutually coherent light beams” is used frequently. By this I mean that the optical signals used have the same frequency, the same polarization, most of the times same amplitude and the resulting interference pattern will depend on their relative/mutual phase (see Chapter 2). Thereafter, their combination will result in a high-contrast interference pattern. Let us consider two light beams/waves $E_1(t)$ and $E_2(t)$ with finite coherence length, see Figure 1-5 [37]. As shown explicitly in section 2.2.1, the interference of both waves is controlled by the product of both electric fields. The product of the two electric fields as a function of time will fluctuate randomly on timescales longer than the coherence time and average to zero over sufficiently long timescales and thus, will not produce the desired high contrast interference pattern as in the previous case.

Here, the temporal coherence of light beams interacting within the metamaterial absorber is essential. Thus, the light beams need to be derived from the same light source (laser) and the coherence length of such source should be long compared to the optical length difference of the interferometer arms. We are able to estimate the coherence length of our laser source, for example, the ID Photonics CoBrite-DX4 laser, which I used in my experiments, has a Δv of 25 kHz. Consequently, the coherence length of the laser is more than 3 km, long enough to sustain the phase information of the light beams throughout our fibre setup.

Moreover, spatial coherence depends on the correlation between the phases of a light wave at different points transverse to the direction of propagation, thus closely related to the beam's waveform. If two or more displaced points reside on the same waveform at given time the fields at those points are spatially coherent [37]. Let's us assume that a monochromatic source (of high bandwidth) illuminates two pinholes (similar to Young's double slit experiment). Strong correlation existing between the phases of the two emitted disturbances and thus, light from the two pinholes will generate an interference pattern (fringes) on a distant plane of observation. One the contrary, if the two pinholes illuminated by separated white light sources (of quite low L_c ~ 1 μm) then no interference fringes will be created and the fields to the two pinholes will be incoherent.

In our experiments, we used two counter-propagating light beams interacting in a fibre metamaterial absorber. The optical signals should be coherent with each other in order to create a high contrast interference pattern, i.e. a standing wave. The quality of the standing wave can be described quantitatively using visibility (V) that is given by:

$$V = \frac{I_{max} - I_{min}}{I_{max} + I_{min}},$$

where I_{max} and I_{min} are the maximum and minimum intensity of the standing wave pattern. For all-optical modulation of absorption (see Chapter 2) and other experiments we will need a standing wave of high V. By using such laser sources the resulting standing waves will be of very good quality and the light-matter interactions will be controlled by constructive and destructive interference, resulting in the desired output functions.

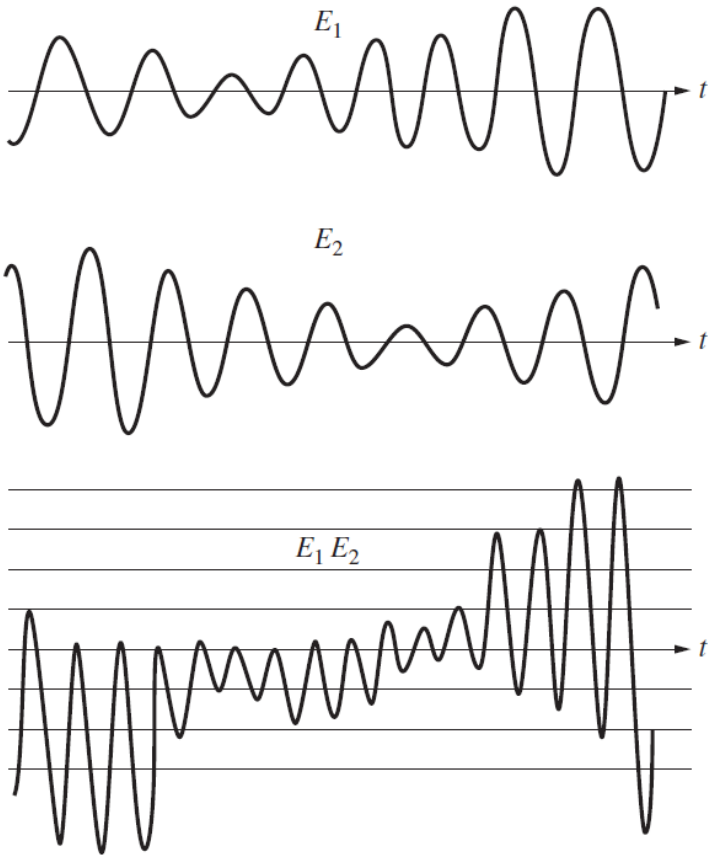

Figure 1-5 **Light waves $E_1(t)$ and $E_2(t)$ with finite coherence length.** The upper and middle panels show time traces of two overlapping electric fields, E_1 and E_2. The lower panel shows the product of the two fields that will be close to zero when averaged over a timescale that is long compared to the coherence time [37]. Figure adapted from Ref. [37].

1.3 Summary

Here, I introduced the background and basic principles that are of major importance for the following chapters of this Thesis. Briefly, I introduced metamaterials and discussed the need for “active metamaterials” (metadevices), for real life applications. I highlighted a few categories of such metadevices and explained their operation principles. Moreover, conventional techniques for all-optical signal processing (which mainly involve nonlinearities) were presented. Lastly, the importance of mutually coherent light beams within our fibre networks was highlighted where I estimated the coherence length of our laser source. In the next chapter, the coherent interactions of light with light in metasurfaces of deeply subwavelength thickness are investigated. This includes proof-of-principle simulations for all-optical switching. Lastly, I report on the steps of fabrication and integration of metamaterials with optical fibres.

Chapter 2 Metamaterials for coherent control of light with light

2.1 Introduction

In this chapter the theoretical background and basic full-wave simulations of fibre metasurfaces for coherent control of light with light are reported. Optimal structure parameters were found and optical properties across the near-infrared telecoms range were simulated. Thereafter, I report on how such metasurfaces can be fabricated on the top of cleaved optical fibres and introduce a methodology for practical realisation of fully-packaged fibre-optic metadevices targeting different wavelengths of operation.

2.2 Coherent control of light with light

According to C. Huygens' superposition principle, two counter-propagating beams of light pass through one another without mutual disturbance [38]. Therefore, control of light signals with light is not a trivial process. Typically, high intensity sources (lasers) are used to engage nonlinear phenomena that allow the Huygens's superposition principle to be broken.

However, Huygens' superposition principle does not prevent the exploitation of the linear superposition of coherent waves to control the interaction of light and matter. Here, this linear all-optical process will be used to achieve all-optical signal processing at low

intensities within a fibre environment. Recent research breakthroughs present coherent control as a highly promising research field with many potential applications such as ultrafast (femtosecond) all-optical modulation [39], modulation of light at arbitrarily low intensity [35], novel spectroscopic techniques [40] as well as manipulation of polarization [41] and propagation direction [42] of light. In this chapter, we discuss the interaction of two coherent counter-propagating waves on a plasmonic fibre metamaterial. Interestingly, the output intensity and absorption can be modulated from 0-100% by varying the phase of one incident wave resulting in constructive or destructive interference on an ideal metamaterial absorber.

2.2.1 Mathematical description of modulation of absorption of light with light via two-wave interference

Here, a mathematical description of coherent control of light with light is presented. We assume two waves that have the same polarization (y), real amplitudes ($\mathrm{E_A}$ and $\mathrm{E_B}$) as well as the same frequency and both propagate through free space in opposite directions along z. The complex electric field of the two waves ($\vec{E}_{\mathrm{A}}$ and $\vec{E}_{\mathrm{B}}$) and their superposition ($\vec{E}_{\mathrm{total}}$) can be written as:

$$\vec{E}_{\mathrm{A}} = \mathrm{E_B} * \mathrm{e}^{-\mathrm{i}(\omega \mathrm{t}+\mathrm{kz}+\varphi)} * \hat{\mathrm{y}}$$
$$\vec{E}_{\mathrm{B}} = \mathrm{E_A} * \mathrm{e}^{-\mathrm{i}(\omega \mathrm{t}-\mathrm{kz})} * \hat{y}$$

$$\vec{E}_{\mathrm{total}} = \vec{E}_{\mathrm{A}} + \vec{E}_{\mathrm{B}} = \left[\mathrm{E_A} e^{-\mathrm{i}(+\mathrm{kz}+\varphi)} + \mathrm{E_B}\mathrm{e}^{-\mathrm{i}(-\mathrm{kz})}\right]\mathrm{e}^{-\mathrm{i}(\omega \mathrm{t})},$$

where φ is the phase retardation of $\vec{E}_{\mathrm{A}}$ (phase retardation can be applied to $\vec{E}_{\mathrm{B}}$ as well). We study the variation of phase from 0-2π.

Now consider the total electric field delivered by the superposition of the two waves in the plane at $z = 0$ (where the metasurface will be placed). The intensity due to electric field is the square of the electric field amplitude of the wave, which is proportional to the local electric energy density. Thus one can define the electric intensity as:

$$I_{\text{total}} = \left|\vec{E}_{\text{total}}\right|^2 = \vec{E}_{\text{total}} \cdot \vec{E}^*_{\text{total}}$$

$$I_{\text{total}} = \left(\vec{E}_{\text{A}} + \vec{E}_{\text{B}}\right) \cdot \left(\vec{E}^*_{\text{A}} + \vec{E}^*_{\text{B}}\right) = \left|\vec{E}_{\text{A}}\right|^2 + \left|\vec{E}_{\text{B}}\right|^2 + \vec{E}_{\text{A}} \cdot \vec{E}^*_{\text{B}} + \vec{E}_{\text{B}} \cdot \vec{E}^*_{\text{A}} .$$

For our waves with real amplitudes (E_{A} and E_{B}) and phase difference φ this simplifies to:

$$I_{\text{total}} = \text{E}_{\text{A}}{}^2 + \text{E}_{\text{B}}{}^2 + 2\text{E}_{\text{A}}\text{E}_{\text{B}} \cos\varphi = I_{\text{A}} + I_{\text{B}} + 2\sqrt{I_{\text{A}} I_{\text{B}}}\cos\varphi ,$$

where

$$\left|\vec{E}_{\text{A}}\right|^2 = I_{\text{A}} \text{ and } \left|\vec{E}_{\text{B}}\right|^2 = I_{\text{B}}.$$

For the case of equal intensities of both waves, $I_{\text{A}} = I_{\text{B}} = \text{I}$ which is most relevant to this Thesis the electric intensity is given by:

$$I_{\text{total}} = 2\text{I} + 2\text{I}\cos\varphi .$$

In the case of constructive interference ($\varphi = 0, \pm 2\pi, \pm 4\pi, \dots$) the total intensity due to electric field at $\text{z} = 0$ reaches:

$$I_{\text{total}} = 4\text{I} .$$

In the case of destructive interference ($\varphi = \pm\pi, \pm 3\pi, ...$) the total intensity due to electric field at $\text{z} = 0$ reaches:

$$I_{\text{total}} = 0 .$$

Our mathematical description shows that constructive interference and destructive interference take place for $\varphi = 0, \pm 2\pi, \pm 4\pi, ...$ and $\varphi = \pm\pi, \pm 3\pi, ...$ phase difference, respectively. If we now place a metasurface at $\text{z} = 0$, then it will interact with the corresponding electric energy density. In our experiments we obtained coherent perfect transmission (destructive interference) for $\varphi = \pi$, when there is no electric field at the metasurface position and therefore no absorption. In contrast, constructive interference led to a large electric energy density interacting with the metasurface causing large absorption.

2.2.2 Thin film in an interference pattern

The basic principle behind coherent control of absorption of light with light may be understood as follows: Consider a film of sub-wavelength thickness that interacts with two counter-propagating and otherwise identical coherent beams of light of the same wavelength, see Figure 2-1 [43]. A standing wave will be formed. The film can be placed at an electric field antinode, field maximum, of the standing wave. In this way, the interactions are strong, resulting high absorption - in principle up to 100 %. In contrast, the film can also be placed in a zero-electric-field node of the standing wave. In this case, the interactions between the film and the electromagnetic wave are negligible. As a result the film becomes highly

transparent for both beams. By shifting the phase (of one beam), from 0 to π, the overall level of absorption can be modulated from 0 to 100 %.

Moreover, for efficient control of light no complicated setups are needed. Lately, many examples for coherent control of light with light have been proposed on nanostructured metamaterials of substantially sub-wavelength thickness. Infinitesimal thickness is needed in order to allow the thin film to be positioned at a node or anti-node of the standing wave, which is essential for control over the light-matter interaction. In order to achieve high-contrast modulation of light, the thin film also needs to interact strongly with light. Thus, a thin film that absorbs half of the intensity of a single beam of light is needed for ideal performance and metasurface nanostructures can be engineered to achieve this [44, 45]. Suitable optical properties can be achieved at resonances [46] of lossy metasurfaces. The spectral position of such resonances scales with the unit cell size of the metamaterial, while the resonant properties are controlled by the unit cell geometry and the constituent materials. In metamaterials, we can engineer the response and improve the resulting optical properties by changing the dimensional parameters [47].

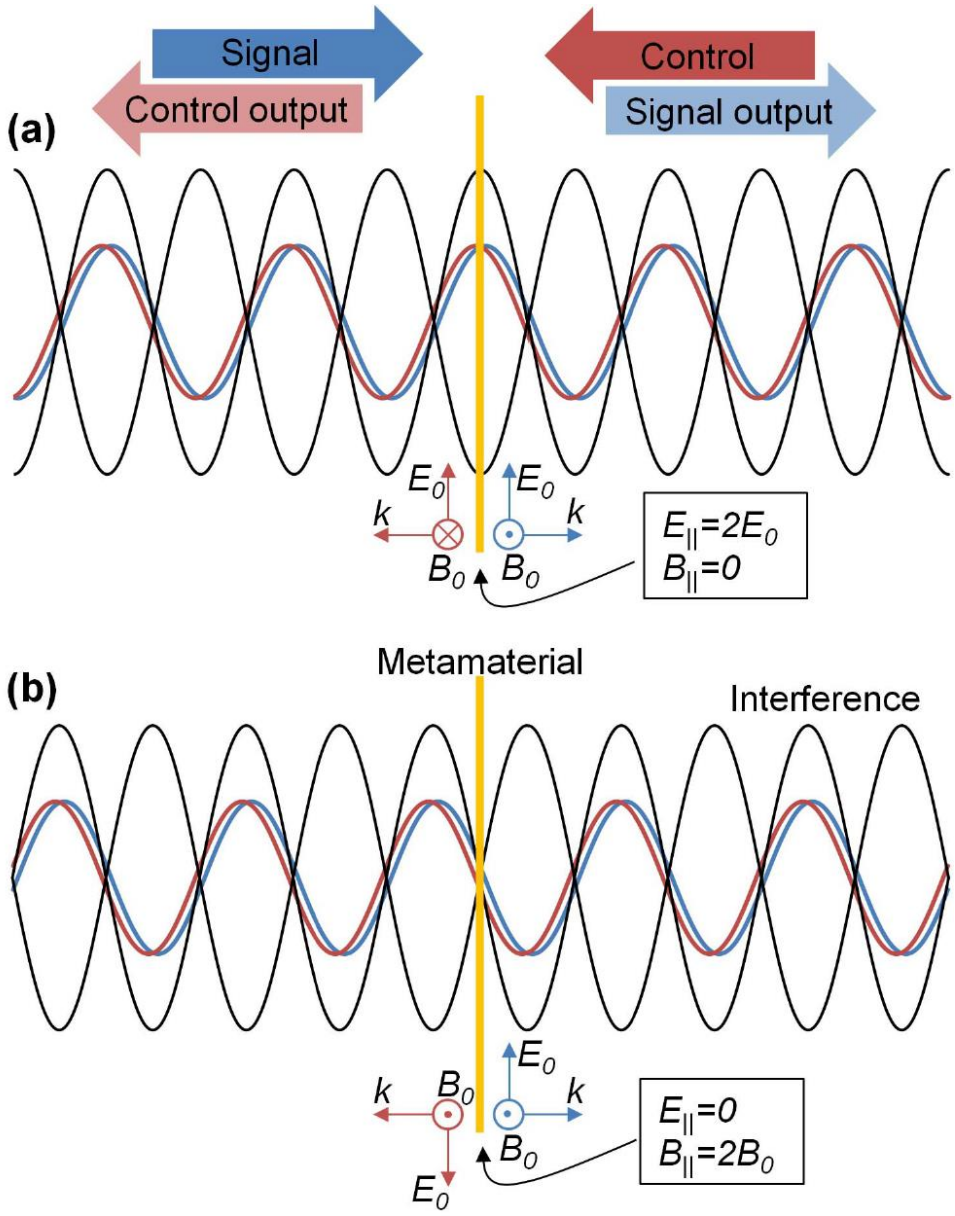

Figure 2-1 **Coherent control of light with light.** Two counter-propagating identical electromagnetic waves interact on plasmonic metamaterial of sub-wavelength thickness. There are two limiting cases: **(a)** constructive or **(b)** destructive interference of the electric field will control electric light-matter interactions. We can control this optical phenomenon by introducing a phase difference in one of the two incident beams (thus, moving the position of the standing wave with respect to the film). In this way, one can lead the system from maximum interactions (negligible transmission) at the antinode to full transparency and zero absorption at the node of the standing wave. Similarly, magnetic light-matter interactions will be controlled by (a) destructive and (b) constructive interference of the incident magnetic field on the nanoscale absorber [43]. Figure adapted from Ref. [43].

2.2.3 Ideal lossy film

Before we proceed to further details regarding simulations, a point of interest should be discussed and clarified. It is mentioned several times throughout this thesis that the ideal absorber for all-optical control of light has 50 % of absorption (A) for illumination from only one side. As explained below, this is the largest possible single-beam absorption for a single film of vanishing thickness [44, 45]. Also it is worth to note that for our experiments we need an absorber of substantially subwavelength thickness in order to shift its position with respect to the standing wave and thus, alter light-matter interactions. Let's us assume that an incident light wave illuminates a plasmonic film at normal incident and that our task is to minimize the reflected and transmitted intensity $|E_R|^2$ and $|E_T|^2$, i.e., maximum A = minimum [Reflection (R) + Transmission (T)].

The incident electric field induces oscillations of the electrons on the interface (metasurface in our case) which will be the same for both sides of the film due to the vanishing thickness. The oscillation of the electrons produces the same scattered electric fields forward and backward (sub-wavelength periodicity of the metasurface implies that all the components of the scattered fields to other directions except forward and backward will be zero due to destructive interference). In the backward direction, the scattered field corresponds to the reflected wave ($|E_{sc}|^2 = |E_R|^2$), while the interference between incident and scattered fields in the forward direction produces the transmitted wave ($|E_T|^2 = |E_{sc} + E_{in}|^2$), see Figure 2-2. Maximum A occurs for the scattered field that minimizes the combined intensity of transmission T and reflection R. Maximum losses require destructive interference between the incident electric field and the scattered field in order to minimize transmission. Destructive interference will occur for any scattered field with the same polarization and a phase difference of π relative to the incident field. It can be shown that maximum absorption occurs when the amplitude of the scattered field is half of the amplitude of the incident field.

$$E_{sc} = 0.5E_{in}e^{i\pi} = -0.5E_{in} .$$

While reflected and transmitted waves correspond to:

$$R\colon\ |E_{sc}|^2 = |E_R|^2 = |-0.5E_{in}|^2 = 0.25|E_{in}|^2 = 25\ \%$$

$$T\colon\ |E_T|^2 = |E_{in} + E_{sc}|^2 = |E_{in} - 0.5E_{in}|^2 = 0.25|E_{in}|^2 = 25\ \%\,.$$

Thus, if R = T = 25 % of the total incident light then the remaining 50% is absorbed, see equation below:

$$A = 1 - T - R = 1 - \frac{|E_{in} + E_{sc}|^2}{|E_{in}|^2} - \frac{|E_{sc}|^2}{|E_{in}|^2} = 50\ \%\,.$$

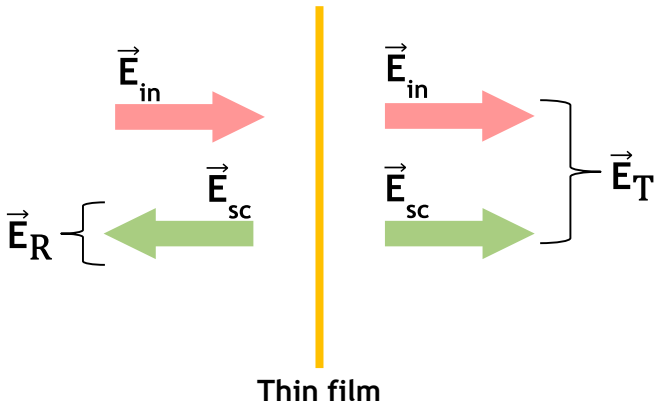

Figure 2-2 **Interactions of a light beam with a film of vanishing thickness.** The schematic shows the interactions between an incident light beam, at normal incidence, and a thin film resulting in scattered electric fields. Magnetic fields are not shown for simplicity.

Larger scattered fields increase reflection more than they can decrease transmission, while smaller scattered fields increase transmission more than they can decrease reflection, resulting in lower overall absorption. This can be shown by considering a real deviation ξ from the above scattered field $E_{sc} = -(0.5 + \xi)E_{in}$ which will lead to absorption of $50\% - 2\xi^2$ according to the above equation which will be less than 50% for any nonzero ξ.

It should be noted here that the film of vanishing thickness is not affected by the magnetic field at reasonable intensities. The magnetic field of the normally incident waves results in a magnetic Lorentz force on charges moving in the film, however, as this force is directed normal to the film, it cannot move electrons that are confined to the film (unless it

is strong enough to extract electrons from the metasurface film). When two counterpropagating and otherwise identical waves constructively interfere on an ideal thin absorber as described above, then the transmission of one incident wave and the reflection of the other will have equal amplitude and opposite phase, resulting in complete cancellation of the outgoing fields and thus coherent perfect absorption of all incident light within the metasurface absorber.

2.2.4 Free standing metasurface for all-optical modulation of light absorption

This subsection comprises the numerical study of a free-standing plasmonic metamaterial absorber. I choose to start with a design that was proposed previously [48] by our research group in order to check my simulation method. The film of 50 nm thickness is an array of asymmetric split-ring gold resonators, see Figure 2-3. The free-standing structure allows light-by-light modulation for two counter-propagating laser beams. A key property is

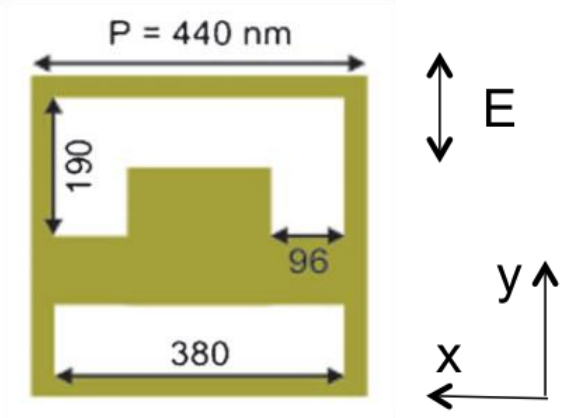

Figure 2-3 **Unit cell of the free-standing plasmonic metamaterial array.** The two-dimensional free-standing structure consists of a gold film of 50 nm thickness perforated with an array of asymmetrically slits (air gaps). Yellow and white colours represent the gold material and the slits, respectively. The structure exhibits interesting behaviour for y-polarized incident light, which is marked by a double arrow [48].

the thickness of the two-dimensional array, which is of $\lambda/31$, where λ is the wavelength of operation. Thus, the film is thin enough to be placed at a standing wave node/antinode where electric field is minimum/maximum and, thus the light-matter interactions will be depressed/enhanced.

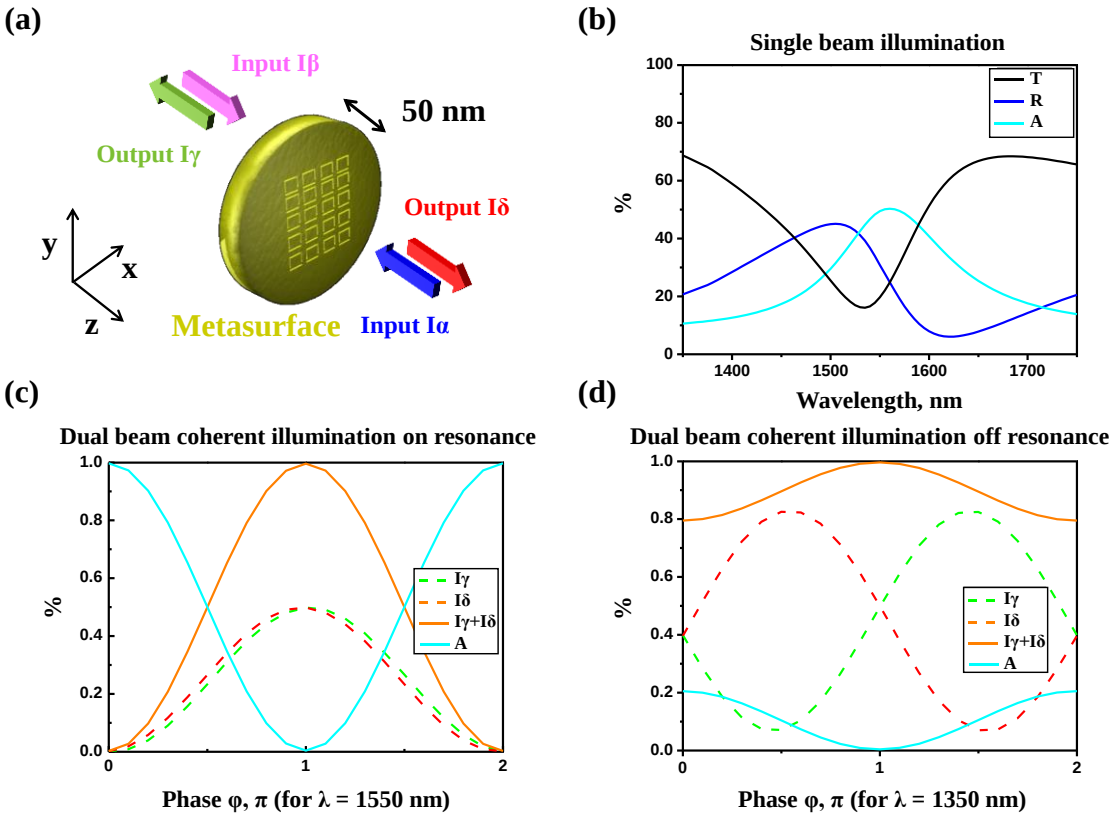

Figure 2-4 **Free-standing metamaterial for coherent interactions of light with light. (a)** Interaction of counter-propagating coherent light beams on a sub-wavelength thickness plasmonic metamaterial. Two limiting cases of interaction exist; the beams can interact constructively or destructively. **(b)** Numerically simulated reflection R, transmission T and absorption A spectra for y-polarized single beam irradiation. Absorption peaks at 49.71 % at a wavelength of 1550 nm. **(c,d)** Total output intensity Iγ + Iδ and absorption A on resonance at 1550 nm and off resonance at 1350 nm, respectively.

The simulation model considers a single unit cell with periodic boundary conditions along the x and y-axes (see Figure 2-4(a)), while incident electromagnetic waves propagate along the positive and/or negative z-axis. Our device is an optical four-port device consisting of two inputs (α and β) and two outputs (γ and δ). We defined as total output intensity Iγ + Iδ and as total absorption A = 1 - (Iγ + Iδ), where the total input intensity corresponds to 1.

As it is shown, a thin film ideally can absorb only 50 % of a single incident beam [44, 45] (Figure 2-4(b)). Thus, the remaining intensity of the beam is either reflected or transmitted. But this changes if the thin film is illuminated by a second coherent beam of light [48].

Figure 2-4(c) shows computational results that indicate that the structure exhibits perfect plasmonic transparency and controlled absorption up to 100 % depending on the phase difference (φ) of the incident waves at the metamaterial position. For our calculations, we used a commercial three-dimensional full-wave solver (Comsol 3.5) based on the finite element method. Gold is described by its permittivity taken from the Palik's handbook [49] ($\varepsilon_{gold} = -132.714 + 12.650i$ at λ = 1550 nm), see Appendix A for the spectral dependence).

2.2.5 Metasurface on fibre for all-optical modulation of light absorption

In principle, there are several possible ways of integrating such a metamaterial into a fibre environment. (i) The free-standing metasurface discussed in the previous subsection could be placed in between the end faces of two optical fibres, (ii) such a metamaterial could be fabricated on the end face of an optical fibre (see next section) or (iii) two fibres could be bonded with the metamaterial on the bonding interface. These cases differ with regard to the materials on either side of the metamaterial, which can be air/air, air/glass or glass/glass, respectively.

While the cases with the same materials on either side of the metamaterial have the advantage of symmetry, fabrication of a metamaterial on the end face of one optical fibre is less fragile, making it more suitable for an initial study, therefore, case (ii) is considered here. (I note that - in principle - a metamaterial could also be fabricated on the side of a D-shaped fibre, however, this geometry is not suitable for coherent control of light with light as discussed above and therefore this case will not be considered here).

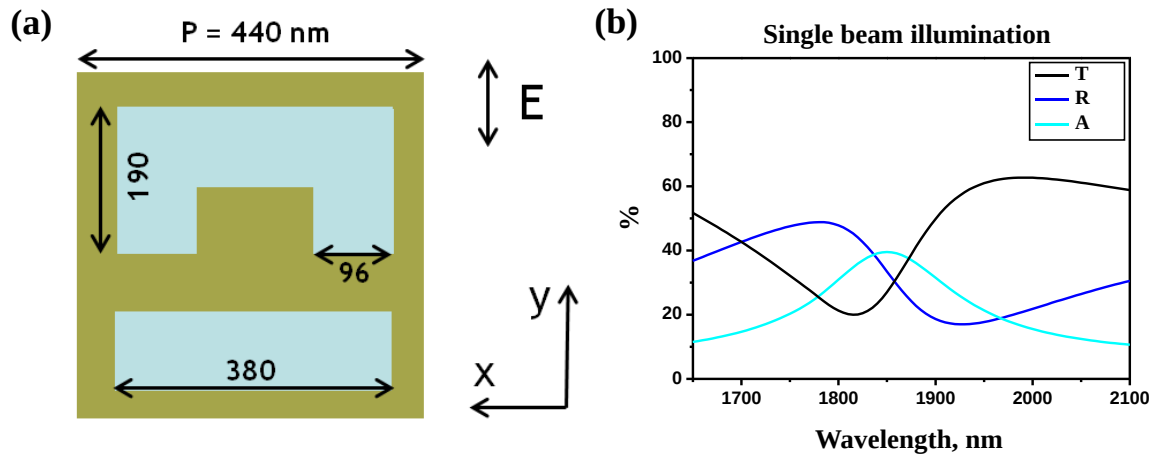

Figure 2-5 **Red-shifted optical properties of the metasurface in the fibre environment.** **(a)** Unit cell of the plasmonic metamaterial on the end face of an optical fibre. Yellow and light blue colours represent the gold material and the fibre substrate underneath, respectively. **(b)** Numerically simulated reflection R, transmission T and absorption A spectra for y-polarized single beam irradiation of the air side. The computational model predicts ~ 39.43 % of absorption at a wavelength of 1855 nm. The structure exhibits interesting behaviour for y-polarized incident light, which is marked by a double arrow.

Figure 2-5 presents the numerical model for the metamaterial on the end face of a fibre and the structure's optical properties for single-beam illumination from the air side. Obviously, the fiber core's permittivity is different from air permittivity, thus, the absorption peak red-shifted (compare Figure 2-4(b) and Figure 2-5(b)). For the silica substrate, I assumed a constant permittivity $\varepsilon_{silica} = 2.1007$ (this permittivity corresponds to the core of the fibre, the cladding permittivity is 2.0852 and assuming that most of the light propagates within the core it is a good approximation to take into account only the permittivity of core in our design).

Figure 2-6(a) shows the plasmonic metamaterial optimization with periodic boundary conditions along the x and y-axes within a fibre environment. Here, the gold thickness t (Figure 2-6(b)) and the length of the slit arm, d = (190 – x) nm, of the plasmonic metamaterial (see Figure 2-6(c) were studied under single beam illumination. The optimized metamaterial geometry has been adjusted in order to shift the absorption peak from 1855 nm back to 1550 nm (see Figure 2-6(d) and Figure 2-7(a)).

The asymmetry introduced by presence of fibre on one side of the metamaterial leads to different reflectivity and absorption depending on the direction of the incident beam (see

Figure 2-7(b)). If the incident beam travels in fibre to the metamaterial, the magnitude of the absorption peak is higher and the reflectivity value is lower. Transmission is the same for both impinging directions due to reciprocity.

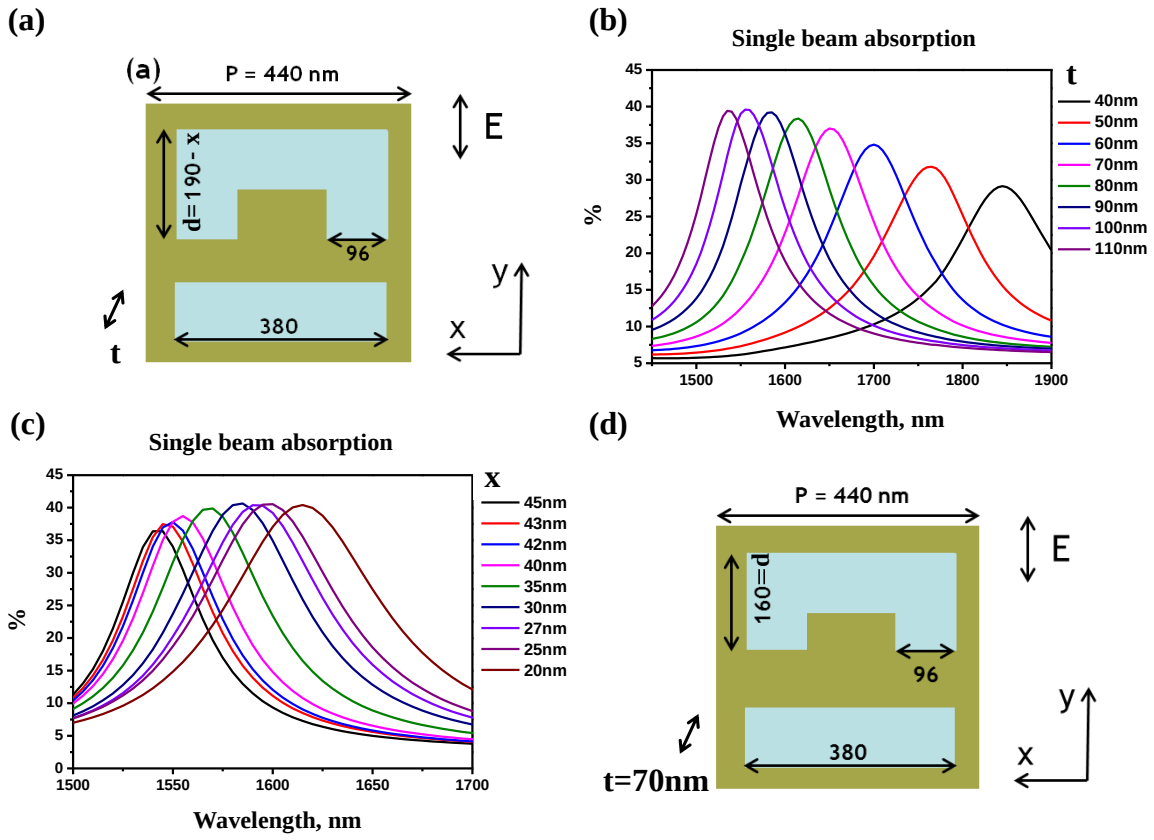

Figure 2-6 **Metamaterial optimization.** **(a)** The unit cell of the plasmonic metamaterial within a fibre environment. Here, t is the thickness of the gold layer and d is the length of the metamaterial slit shown in the figure. **(b)** Numerical calculation of absorption for single-beam illumination, different gold thicknesses t and constant x = 10 nm **(c)** Numerical calculation of absorption for single beam illumination, different metamaterial slit lengths described by parameter x and constant t = 60 nm. **(d)** The metamaterial unit cell with the optimal structure parameters (x = 30 nm and t = 70 nm).

Figure 2-7(c) shows the computational results for the metamaterial on fibre under coherent illumination on resonance at 1550 nm and off resonance at 1650 nm (see Figure 2-7(d)). The asymmetry along the propagation z-axis (air/fibre) caused by the presence of fibre has led to different resonant phase-dependent modulation of the output channels Iγ and Iδ (compare Figure 2-4(c) and Figure 2-7(c)), however, the phase-dependence of the total output power remains similar.

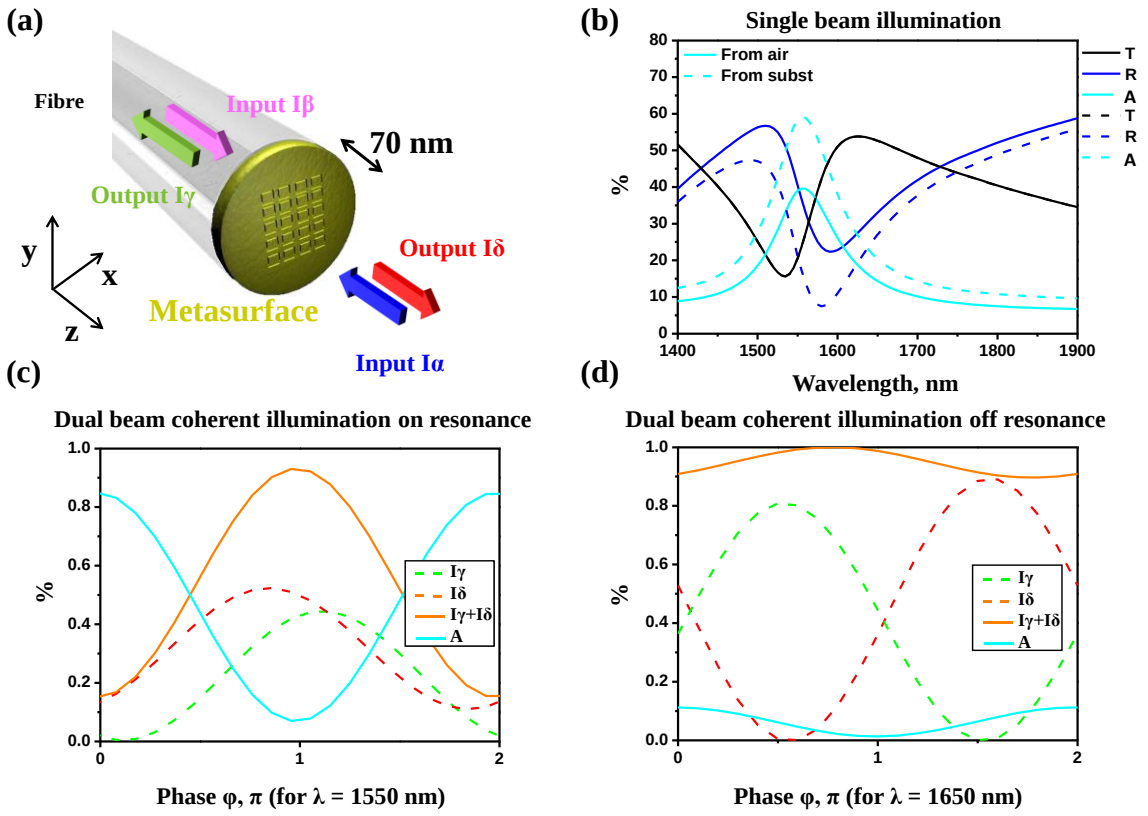

Figure 2-7 **Metamaterial on a fibre for coherent interactions of light with light. (a)** Interaction of counter-propagating coherent light beams on an optimized plasmonic metamaterial (see Figure 2-6(d)). **(b)** Numerical calculation of reflection R, transmission T and absorption A for a single beam impinging on the metamaterial from the silica (dashed) and air (solid) side. **(c,d)** Output power Iγ + Iδ and absorption A for coherent illumination of the metamaterial simultaneously from the air and silica sides with equal intensity and a phase difference φ at the resonance wavelength of 1550 nm and off-resonance at 1650 nm.

To conclude, I studied the optical properties of a free-standing metamaterial absorber and its potential for fibre integration. As shown, the metamaterial's resonance wavelength can be tailored by design [47], i.e. structural parameters and thickness. Thus, the desired optical response for single beam illumination was shifted to the range of the telecommunication C-band. When this was achieved I explored the concept of coherent modulation of optical absorption with the plasmonic metamaterial by dual coherent illumination (illumination by two counter-propagating light beams). For ideal coherent interactions, the optimised metamaterial should be at the resonance frequency. Then the plasmonic absorber can act as an all-optical switch integrated on the end face of an optical

fibre. Of course I expect some deviation from the ideal design due to fabrication imperfections and encapsulation losses but as shown in the next chapters, the optical behaviour of the fibre-packaged metasurface allows a wide range of all-optical functions. In the next section the metamaterial fabrication and packaging are discussed.

2.3 Metamaterial fabrication and packaging

The fabrication of metasurfaces on optical fibre tips was done entirely by myself, however, I acknowledge help of Dr. Y. Jung with encapsulation and packaging of fibre metamaterials.

Recent developments in nanofabrication and metal deposition techniques allow fabrication of plasmonic nanopatterns such as gold metamaterials with unit cell size squeezed down to the optical subwavelength scale of hundreds of nanometres. Within this section the different schemes used for the preparation of fibre metadevices are described. Briefly, the preparation of the fibre, metal thermal evaporation on the cleaved end face of the fibre and the metasurface fabrication are explained. It is important for the fibre metasurface to be compatible with standard fibre telecommunication systems. Thus, the fibre metamaterial is fully packaged using a combination of micro-lenses and fibre ferrules resulting in a robust fibre-optic device for telecommunications networks.

In all experiments, I used single-mode polarization-maintaining Panda style optical fibres (Thorlabs P3-1550PM-FC-2-FC/APC). Mechanical cleaving (controlled breaking that creates a flat end face) of the fibre has been used. In this step, the polymer jacket has been removed, and then the fibre has been cut (perpendicular to the core axis) in order to have a smooth surface at the end. The mechanical cleave creates several micro/nano pieces of silica glass all around the fibre's end face. Thus, solutions of ethanol and isopropanol for cleaning purposes have been used. The stripped fibre was checked using a SEM to identify the position of the slow axis with respect to scratches introduced while stripping the polymer jacket, see Figure 2-8(a,b). Consequently, one can identify the right orientation for

fabrication of the fibre metamaterial with respect to the fibre's slow axis after metal deposition. Moreover, the cleaved fibre was fixed on a fibre holder. Then the fibre holder was attached to the holder of the evaporator (Bob Edwards FL-400 Auto 306). The holder of the evaporator rotates in order to ensure uniform metal deposition. The metal deposition took place in high vacuum conditions ($\sim 5 \times 10^{-6}$ mbar) in order to avoid atom-particle collisions since the gold atoms/particles travel towards the holder during evaporation. The metal deposition rate was adjusted to $0.08\ \mathrm{nm/s}$. One can control the deposition rate, which controls the quality of the film, with the applied voltage across the metallic boat/crucible where the gold pellets are placed, see Figure 2-8(c-d). Thereafter, deposition of 70 nm of gold on the end face of the optical fibre is obtained. In our case, there were no issues with adhesion while in larger deposition areas the addition of Cr or Ti ensures good bonding between the metal layer and glass substrates.

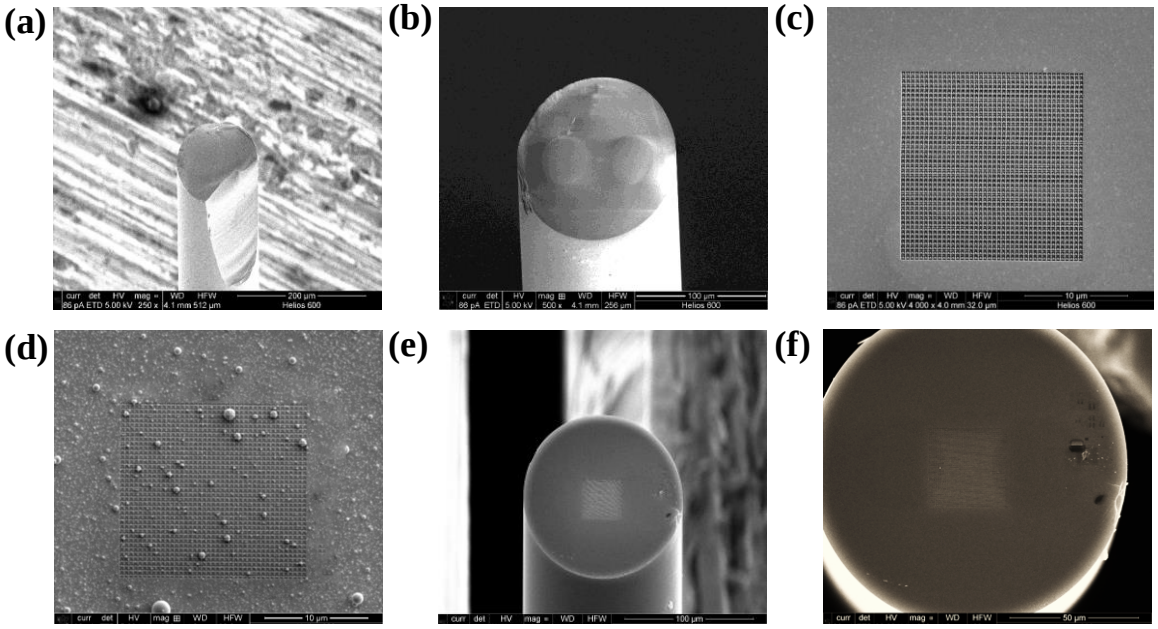

Figure 2-8 **Fabrication of metamaterial on polarization-maintaining fibre. (a)** Mechanical cleave can lead to break part of the fibre's end. **(b)** Cleaved polarization-maintaining fibre under SEM illumination. The two stress rods can be seen on opposite sides of the much smaller fibre core. **(c)** Successful and **(d)** unsuccessful deposition affects film smoothness and metamaterial structure quality, respectively. **(e)** The alignment of the polarization-dependent metamaterial has been done with respect to the grooves of the sample holder and scratches on the fibre end that occurred during stripping of the polymer jacket. **(f)** Metamaterial pattern on the polarization-maintaining fiber. The plasmonic metamaterial has been fabricated by nanostructuring the centre of a gold layer covering the fibre core.

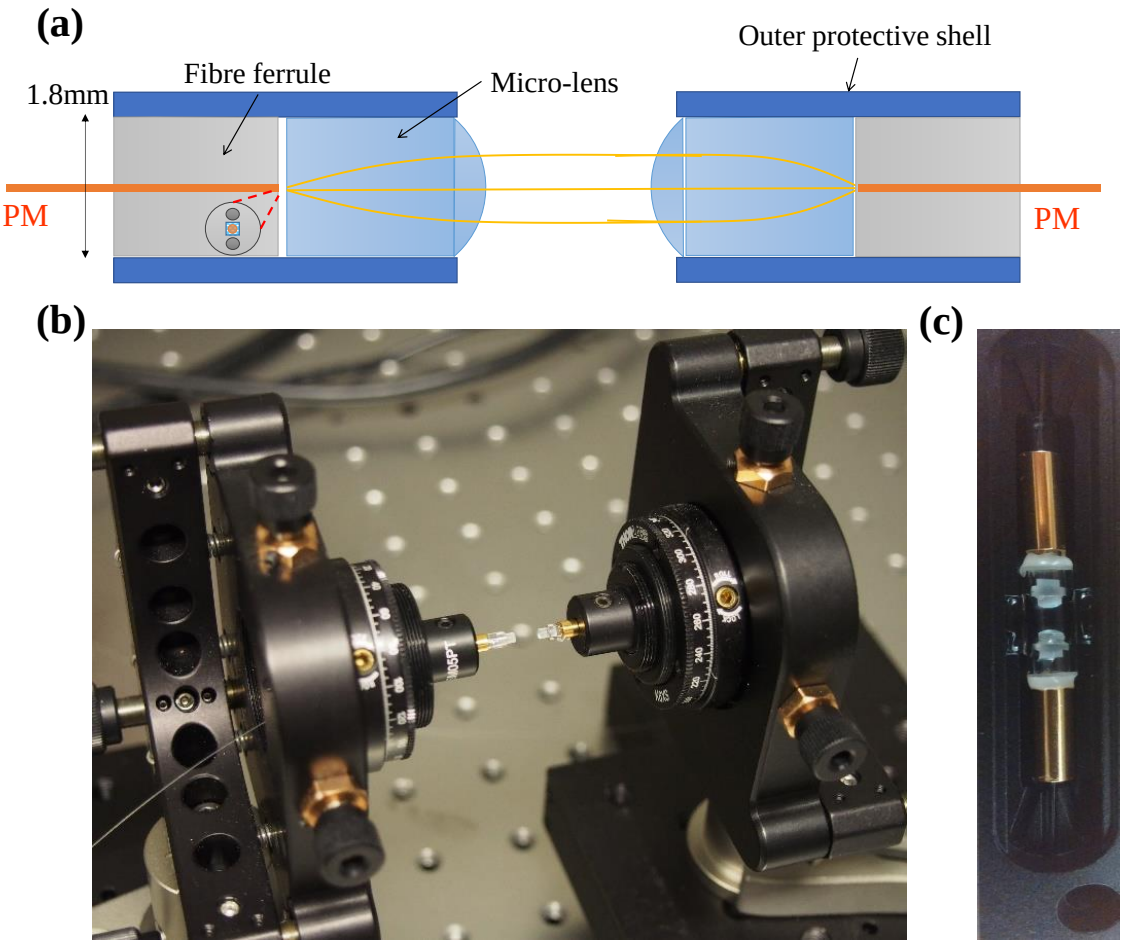

Figure 2-9 **Metamaterial packaging with micro-fibre-optic components.** **(a)** The metamaterial fibre was placed within a fibre ferrule and combined with a lens in order to collimate the optical beam. Then a second lens was used to focus/couple the light to the core of a bare fibre. PM - polarization-maintaining fibre. **(b)** Kinematic stages allow alignment within three dimensions and rotational control. **(c)** A photograph of the packaged metadevice (without lid) consisting of the metasurface-covered fibre coupled to a bare fibre end using a pair of microcollimator lenses.

The plasmonic fibre metamaterial structure with 25 × 25μm^2 overall area was fabricated in a 70nm gold film by gallium focused ion beam milling (Figure 2 8(e-f)). Satisfactory structure quality was achieved with an area dose of 20 mC/cm^2 and a beam current of 28 pA. Commercial software (DesingCAD, NPGS) was used to control both stages (in three axes) and scanning of the ion beam.

In order to allow metamaterial illumination from both sides, the metamaterial-covered fibre was interfaced with a second polarization-maintaining fibre using a microcollimator arrangement consisting of a pair of microlenses. Specifically, the metamaterial-covered fibre

end was inserted into a fibre ferrule and positioned at the focal point of an anti-reflection-coated microlens to assemble a compact microcollimator that was stabilized by a glass capillary shell. The second cleaved fibre tip was mounted in the same way. Using kinematic mounts, the light beams from the two microcollimators were aligned with each other by maximizing the optical coupling efficiency and polarization contrast. The aligned microcollimator arrangement was then fixed with UV-cured adhesive, stabilized with an outer glass capillary shell and placed in an anodized aluminum enclosure for additional protection, see Figure 2-9(a)-(c).

As we discussed in Chapter 7 the fibre metamaterials can also find applications down to the quantum regime. For such applications it is important that the generated photons will be mainly correlated pairs. Briefly, illumination of a type-1 beta-barium borate (BBO) crystal by a continuous wave laser, λ = 405 nm, produces correlated single photon pairs by spontaneous parametric down conversion (SPDC) [35] and thus, the resulting entangled photon pairs will be at a wavelength of 810 nm. While the metadevice's microcollimator lenses work fine around the telecommunications C-band, they have remarkable losses around 810 nm. The antireflection coating of the lenses is designed for operation at near infrared telecoms bands. As one can see in Figure 2-10(a), light transmitted from the lenses experiences losses as high as 17 dB (for two different types of coated lenses) compared to one standard single-mode fibre (SMF) at the wavelength of interest. Thus, a new approach for the preparation of metadevices for quantum experiments required.

As above-mentioned, the problem is the lenses (antireflection coating) operation wavelength range. Lenses were used in order to eliminate coupling losses since the numerical aperture (N.A. = $\sqrt{n_{core}^2 - n_{clad}^2} = 0.13$) of the fibres is significant and the light will spread rapidly when exiting the fibre. But what will happen if the two fibres come together? Exactly this is what I investigated in following experiment. I proposed an alternative solution of packaging without collimation lenses. Briefly, the two fibres, the fibre metamaterial (with appropriately scaled dimensions, see Chapter 7) and the coupling bare fibre, were inserted within the same fibre micro-ferrule with a diameter of (127 $\pm$ 2) μm and attached gently, see Figure 2-10(b)-(c). Then the slow axes where aligned by monitoring the output-coupled optical power. Additional layers of protective glass tubes (two layers) were installed and epoxy applied in every step (Figure 2-10(b)). Lastly, a metal housing that ensures mechanical robustness was added. The metadevice package, Figure 2-10(d), is finally connected to standard FC/APC connectors in both sides.

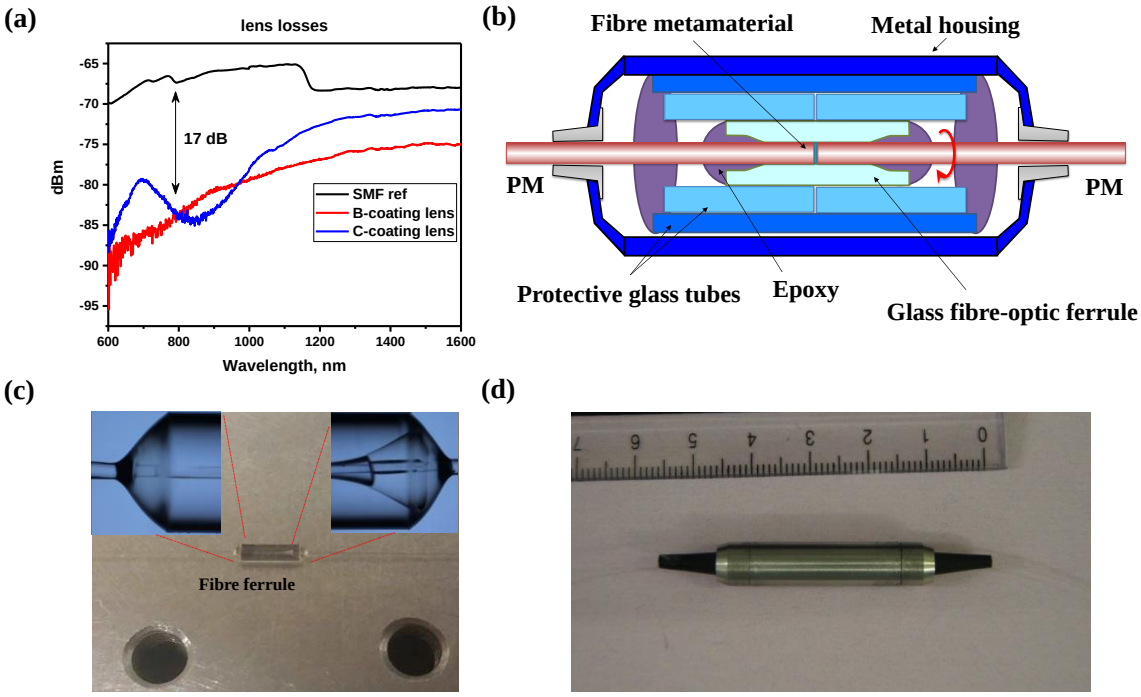

Figure 2-10 **Fibre packaging for applications at a wavelength of 810 nm. (a)** The measured optical power transmission for a standard single-mode fibre used as a reference (SMF ref) with black line, and for two types of antireflection coated lenses B and C with red and blue line, respectively. **(b)** The schematic shows the fibre-optic components used for the plasmonic metamaterial encapsulation for operation at a wavelength of 810 nm. The fibre metamaterial is enclosed between the two optical fibres. **(c)** Photograph of the micro-ferrule. Insets: photographs recorded under an optical microscope revealing that the fibres are fully inserted within the fibre ferrule. **(d)** The resulting fully encapsulated metadevice within a metal housing. The ruler shows that the device's length is about 6 cm.

2.4 Conclusions

In this chapter, I investigated the optimal structure parameters for effective all-optical signal modulation of metamaterials integrated with optical fibres. Proof-of-principle simulations were presented. Thereafter, I have shown the plasmonic fibre metadevice fabrication and packaging. Details regarding the preparation of the fibre, metal deposition and metasurface fabrication through focused ion beam milling were explained. I offered solutions of fibre packaging at wavelengths of 1550 nm and 810 nm. The latter packaging concerns quantum experiments where the fibre lenses used in previous attempts experience great losses at that spectrum range (see Figure 2-10(a)). All packaging modules are mechanically and chemically stable and compatible with standard fibre-optic components. Consequently, such fibre metadevices allow first practical telecommunications applications of photonic metamaterials. The aforementioned results became possible thanks to the recent development of novel nanofabrication techniques at the optical fibre tip. Further development of this concept may lead to novel solutions in quantum optical fibre-based devices.

Chapter 3 Fibre-optic metamaterial gate for all-optical signal processing

Part of the work in this chapter has been published as: **Fibre-optic metadevice for all-optical signal modulation based on coherent absorption.** A. Xomalis, I. Demirtzioglou, E. Plum, Y. Jung, V. Nalla, C. Lacava, K. F. MacDonald, P. Petropoulos, D. J. Richardson, and N. I. Zheludev. *Nature Communications* **9**, 182 (2018) [50]. The fabrication of metasurfaces on optical fibre tips and measurements at kHz frequencies were done entirely by myself, however, I acknowledge help of Dr. Y. Jung with encapsulation of fibre metamaterials and assistance of I. Demirtzioglou and Dr. C. Lacava with experiments at GHz frequencies. Other co-authors contributed with advice and/or to supervision and writing of the article.

3.1 Introduction

The majority of today's communications relies on transmission of data through optical fibres. Optical data transmission is superior to electronic data transmission in terms of bandwidth and energy consumption. Essential for the use of information is signal processing, where recovery, modification and further transmission of the input signals takes place. Thus, for implementation of optical data networks efficient all-optical signal processing devices/techniques are required. All-optical signal processing functions can be logic relations between input-output channels, optical switching (modulation of the level of absorption in the system), all-optical amplification of small signals and other. A point of vital importance is that such systems/devices need to operate within the telecommunications wavelength bands. Most widely used bands are C (1530 - 1565 nm) and L (1565 – 1625 nm), where the loss of silica fibres is low, chromatic dispersion is weak and erbium doped

amplifiers are available (for C-band). Thereafter, high bandwidth operation and potential for fibre integration/packaging are essential for devices' practicality and integrability.

In this chapter, I investigate, experimentally, how optical control over metasurface absorption can be used for all-optical signal processing. Then, I demonstrate that fibre metadevices can be successfully integrated within fibre coherent networks. Moreover, I perform all-optical signal processing at data rates that are compatible with conversional communications systems. Lastly, I show that the power required for such signal processing implementations can be in the order of few fJ/bit (~ 20.000 photons).

In more details, coherent control of the optical response of thin films in standing waves has attracted considerable attention, ranging from applications in excitation-selective spectroscopy and nonlinear optics to all-optical image processing. Here, I show that integration of metamaterial and optical fibre technologies allows the use of coherently controlled absorption in a fully fiberized and packaged switching metadevice. With this metadevice, which controls light with light in a nanoscale plasmonic metamaterial film on an optical fibre tip, I provide proof-of-principle demonstrations of logical functions XOR, NOT and AND that are performed within a coherent fibre network at wavelengths between 1530 and 1565 nm. The metadevice has been tested at up to 40 Gbit/s and sub-milliwatt power levels. Since coherent absorption can operate at the single-photon level and with 100 THz bandwidth, I argue that the demonstrated all-optical switch concept has potential applications in coherent classical and quantum communication fibre networks.

All-optical signal processing fundamentally relies on modulation of one optical signal with another. Therefore all-optical logical functions have long been perceived as the exclusive domain of nonlinear optics [51], which requires a minimum level of intensity to activate the nonlinear material response and faces trade-offs between magnitude and speed of the nonlinearity involved [34, 52-55]. However, recently it was shown that an effective nonlinear response may be derived from coherent interaction of light with light on linear materials of substantially sub-wavelength thickness [56]. In contrast to conventional optical nonlinearities, the effect has been shown to allow intensity-independent control over absorption of light, from almost 0% to almost 100% [48], with 100 THz bandwidth [36, 39] and even for single-photon signals [35]. The concept has enabled all-optical control of luminescence [57, 58], redirection of light [42, 59] as well as control of nonlinear [60], polarization [43] and quantum [61, 62] effects in films of nanoscale thickness and excitation-selective spectroscopy [40]. In particular, it has been predicted that coherent interaction of

light waves on lossy ultrathin films could perform signal processing functions [56] and proof-of-concept experiments in the static regime have been reported [63, 64].

3.2 Coherent metamaterial absorption in a fibre network

As illustrated in Figure 3-1(a), the functionality of the network is based on controlling absorption of light with light on an ultrathin metamaterial absorber. It has two bidirectional ports, i.e. two inputs, α and β, and two outputs, γ and δ. The input waves propagate in opposite directions and, provided that they are mutually coherent, co-polarized and of equal intensity, they will form a standing wave with electric field nodes and anti-nodes (Figure 3-1b). A sufficiently thin film may thus be placed at a node, where the electric field is zero due to destructive interference, or at an anti-node where the electric field amplitude is enhanced by constructive interference. Since truly planar structures interact with normally incident waves only via the electric field [65], this implies that a planar thin film placed at a node will be perfectly transparent, while the same thin film will be strongly excited if placed at an anti-node. With respect to absorption, which is limited to 50% in planar materials illuminated by a travelling plane wave [44] (see subsection 2.2.3), standing wave illumination allows absorption to be controlled from 0 to 100% in the ideal case [56]. Such performance in the optical part of the spectrum, as is relevant to optical fibre technology, may be approximated with materials that are thin compared to the optical wavelength and exhibit equal levels of transmission and reflection in addition to around 50% travelling wave absorption (see subsection 2.2.3). This combination of parameters may be achieved for example in nanostructured plasmonic metamaterials [48] and 30-layer graphene [35, 66] (see section 7.1).

The planar absorber used here is a plasmonic metamaterial consisting of a 70-nm-thick gold film perforated with an array of asymmetrically split ring apertures, as previously deployed in free-space demonstrations of coherent light absorption and transparency [48]. The dependence of this structure's transmission, reflection and absorption characteristics on aperture size and geometry [47] is well understood, allowing for easy optimization

throughout the optical telecommunications bands (see subsection 2.2.5). Our switch operates at wavelengths around $\lambda = 1550$ nm, where its 70 nm thickness corresponds to $\lambda/22$. The metamaterial structure was fabricated by thermal evaporation of gold and subsequent focused ion beam milling on a $25 \times 25\ \mu m^2$ area covering the core of a cleaved polarization-maintaining single-mode silica fibre (see inset to Figure 3-1), with the symmetry axis of the metamaterial aligned to the slow axis of the fibre (see Methods section 3.7 and section 2.3 for details). The fibre output was coupled to a second cleaved polarization-maintaining optical fibre using two microcollimator lenses to realize an in-line fibre metadevice (Figure 3-2).

The metadevice is terminated with standard FC/APC fibre connectors and it was characterized in a fibre interferometer assembled from standard polarization-maintaining fibre components (Figure 3-2). The output of a fibre-coupled CW laser was split along two paths of similar length, with one path containing an electro-optic phase or intensity modulator and the other containing a variable attenuator to allow balancing of the power propagating along the two paths. The paths were then recombined within the metadevice and the output signals were detected via circulators using an oscilloscope (see Methods section 3.7 for a more detailed description). I note that practical applications would require active stabilization of the optical path lengths, however the system shown here is sufficient to characterize the principle of operation of the fiberized switch. This is illustrated by the eye diagrams in Figure 3-2, which show that the eye closes on a timescale of seconds due to phase drift in the interferometer.

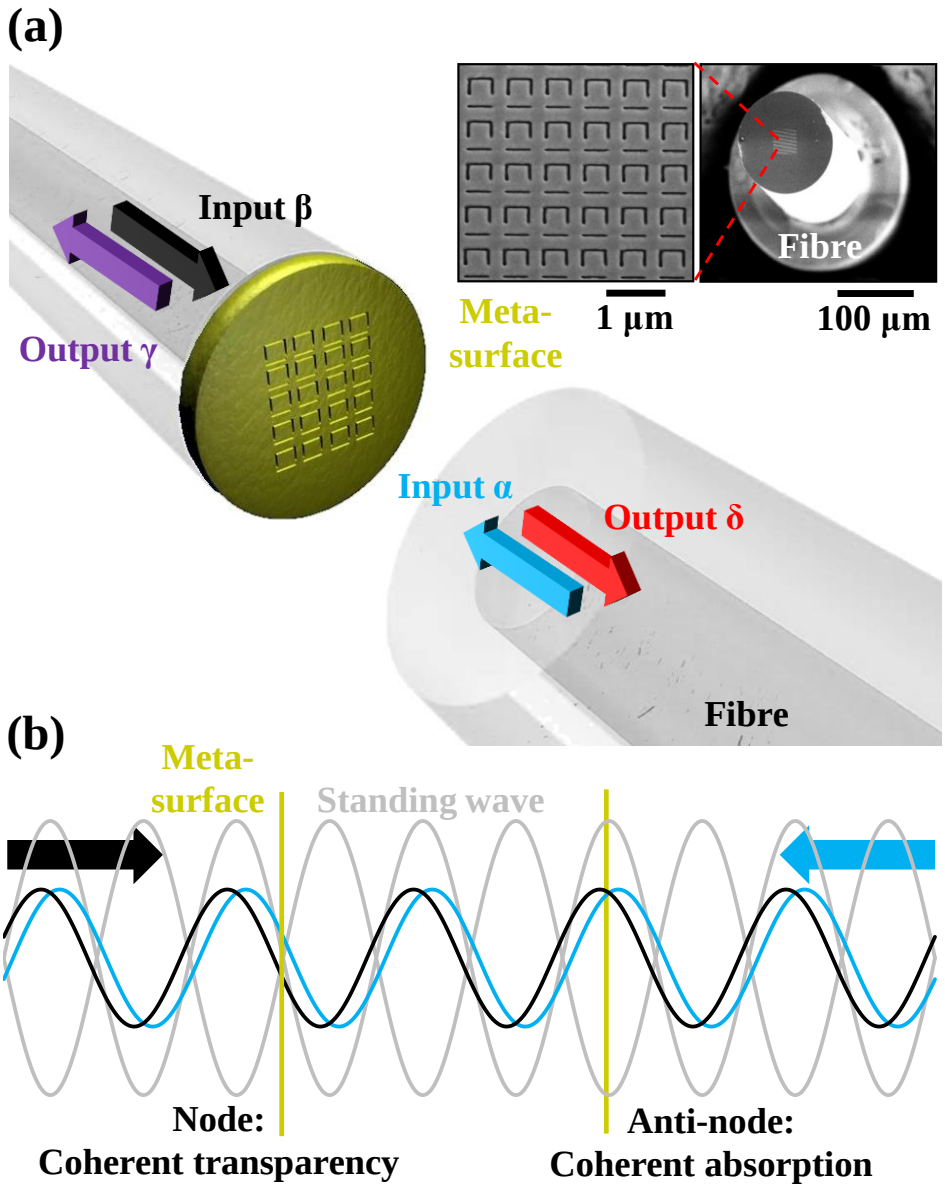

Figure 3-1 **Coherent interaction of light with light on a fibre metamaterial absorber.** **(a)** The plasmonic metasurface can act as four-port device with two optical input signals (α and β) interacting on the metasurface absorber, generating two output signals (γ and δ). The metasurface has been fabricated by nanostructuring the central 25 × 25 µm^2 of a 70-nm-thick gold layer covering the cleaved end-face of a polarization-maintaining single-mode silica fibre [inset scanning electron microscope (SEM) images]. **(b)** The counterpropagating coherent input signals form a standing wave wherein the metasurface can be located at a position of destructive interference of electric fields (node) where absorption is suppressed or at a position of constructive interference (anti-node) where absorption is increased.

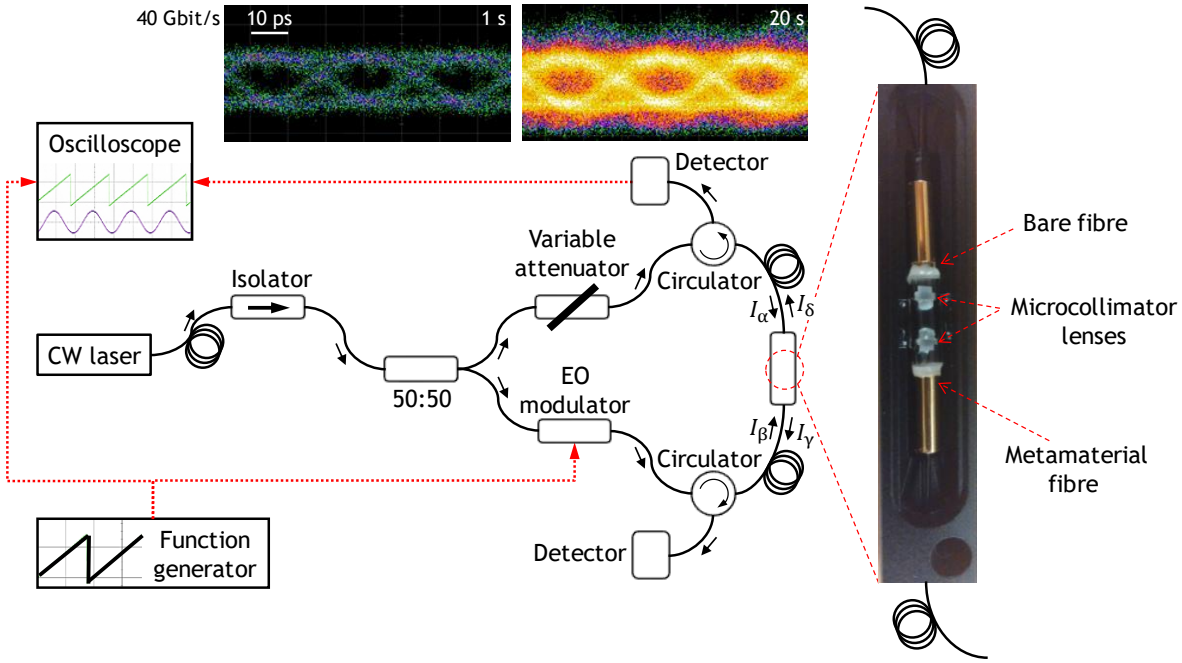

Figure 3-2 **Fibre-optic interferometric setup.** Schematic representation of the fully fiberized experimental setup with a photograph of the packaged metadevice (without lid) consisting of the metasurface-covered fibre coupled to a bare fibre end using a pair of microcollimator lenses. The inset shows eye diagrams of the intensity of output channel δ recorded for intensity modulation of input channel β at 40 Gbit/s, where colour indicates counts and the white scale bar indicates 10 ps.

3.3 All-optical signal modulation and amplification

Figure 3-3(a) shows the phase-dependent output intensities I_γ and I_δ relative to the input intensity $I_\alpha = I_\beta$ as a function of the phase difference between the inputs at a wavelength of 1550 nm. The overall output power can be controlled from about 9% to about 57% of the total input power, where a low output level corresponds to constructive interference of the incident waves on the metasurface and thus coherent absorption, while a high output level

corresponds to coherent transparency. Both output signals display a similar phase-dependence; however, the phase dependent output intensity I_δ offers somewhat higher contrast and therefore we focus on this output. It should be noted that, for an ideal metadevice containing a perfectly symmetric ultrathin absorber showing 50% single-beam absorption (with no other loss mechanisms) and equal reflection and transmission for both directions of propagation, both output intensities would be identical and modulated from complete absorption to perfect transmission (see subsections 2.2.3 and 2.2.4). Differences between the measured output channels arise in the present case from the asymmetric construction of our metadevice that contains a metasurface fabricated on the glass/air interface of one of the optical fibres. The whole metadevice exhibits about 24% single-beam transmission, 18% (8%) reflection and 58% (68%) losses for a single input signal α (β). However, only part of these losses correspond to metasurface absorption that can be coherently controlled, while other sources of loss include the fibre connections of the metadevice, scattering and unwanted reflections within the microcollimator and fabrication imperfections such as imperfect alignment of the metasurface orientation with the slow axis of the fibres.

The nonlinear functionality, of input-output relations, of the switch is illustrated by Figure 3-3(b), which shows how the output intensity I_δ depends on the input intensity I_β while I_α remains constant for various phase differences between the input beams. The measured output intensity I_δ as a function of input I_β is nonlinear and generally follows the behavior predicted by Fang et al. [56]. For input phase differences of less than $\pi/2$ it is also nonmonotonic—counterintuitively the output intensity decreases with increasing input intensity and reaches a minimum before increasing when I_β becomes large. For an input phase difference of $\pi/2$, changes in the measured output intensity I_δ are approximately proportional to changes in the input intensity I_β. For larger input phase differences, I_δ flattens with increasing I_β, but is steep for small I_β suggesting possible applications in small-signal amplification (see Figure 3-4). Thus, the results presented in Figure 3-3 show that large changes of the metadevice output result from modulation of phase or intensity of one of the metadevice inputs.

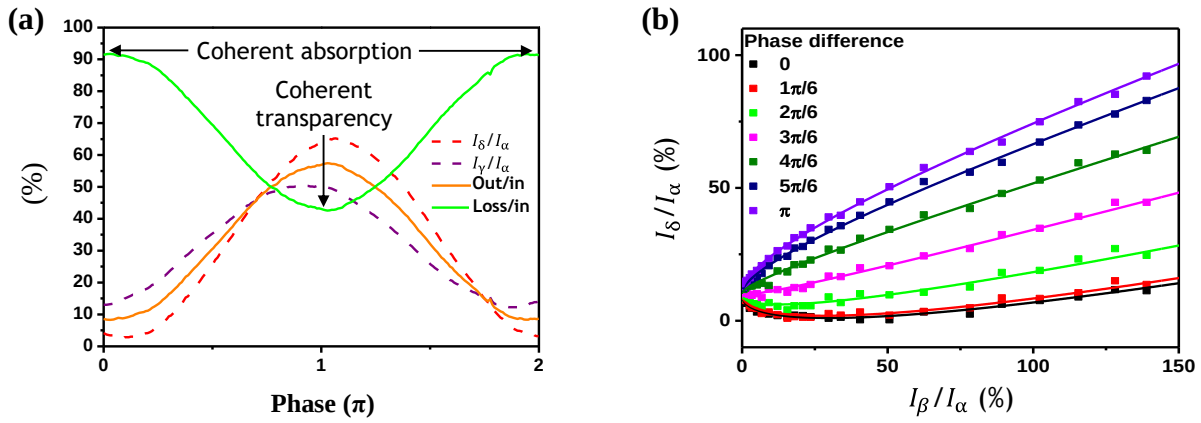

Figure 3-3 **Phase-dependent output intensities.** **(a)** Measured output intensities I_γ and I_δ (relative to I_α) as well as the total output power and metadevice losses (relative to the total input power) as a function of the phase difference between the input signals at the metasurface at a wavelength of 1550 nm. **(b)** Measured output intensity I_δ (data points) relative to the fixed input intensity I_α as a function of input intensity I_β for various phase differences between the input beams, with fits (lines), at wavelength of 1550 nm.

Figure 3-3(b) demonstrates an effective nonlinearity of input-output relationships that can be used for small-signal amplification (Figure 3-4), especially for an input intensity ratio of $I_\alpha / I_\beta \sim 100$ and mutual phase close to π. Interestingly, when a light beam of high intensity propagates through a nonlinear medium, harmonic distortion occurs, which can cause optical instabilities. Here, the effective nonlinear input-output behaviour of the four-port device considered in this experiment is quite different. This behaviour is characteristic of our four-port device and can be explained by redistribution of energy among different channels [56] and does not cause harmonic distortion of signals. Such four-port optical devices can mimick a variety of functionalities of electronic components, e.g. the small-signal amplification of the transistor. Where small modulation at the input is translated to large modulation at the output port. Here, constant input intensity I_α can act as bias voltage. In Figure 3-4 is presented the small-signal differential gain (G) of the metadevice:

$$G = \frac{d(I_\delta)}{d(I_\beta)}$$

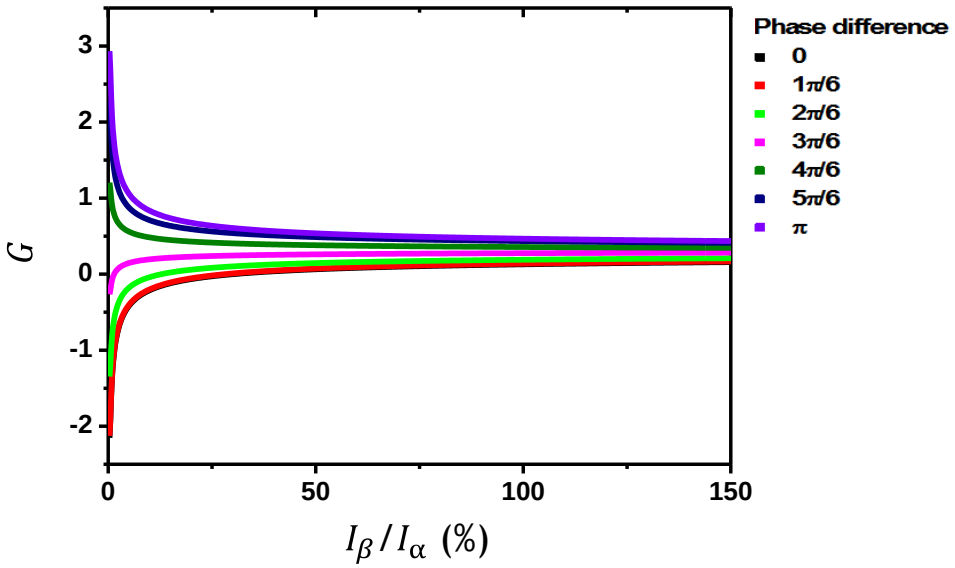

Figure 3-4 **Small-signal differential gain (G) in a four-port coherent optical device.** The gain of the metadevice as a function of the input intensity I_β for various phase differences between the input beams at a wavelength of 1550 nm. The curves shown were calculated as the first derivative of the fits shown in Figure 3-3.

In principle, G can take large values as I_β reaches zero. In our case, experimental findings shown that G can reach 3 for small I_β, see Figure 3-4. For an ideal free-space device G can take values, in principle, as high as 10 [67]. We therefore anticipate that such fiberized metadevices may be used in in-fibre applications where the bandwidth of electronic amplifiers limits the investigation and detection of ultrafast phenomena. We note that practical applications would require a more sophisticate fabrication, which may lead to better device performance and thus, larger small-signal gain.

3.4 All-optical signal processing

All-optical signal processing operations with input/output relations analogous to logical functions may now be realized in the network by exploiting coherent transparency and/or coherent absorption in the metadevice. In what follows, binary logic states encoded in beams of equal intensity but opposite phase in the metasurface plane are denoted '+' and '−', while opposing states encoded as low/high intensity are denoted '0'/'1'. Consider, in the first instance, the case of mutually coherent, binary, phase-modulated input signals + and −: constructive interference of identical bits α and β will lead to coherent absorption on the metasurface, while destructive interference of opposite bits will lead to coherent transparency, producing an intensity-modulated (0/1) output α XOR β. The behavior of an ideal switch is summarized in Table 3-1 and the measured behavior of the experimental metadevice is shown in Figure 3-5(a), for a modulation frequency of 10 kHz. The switch clearly presents XOR functionality with high contrast (>10×) between the output states. The intensity of the output logical 1 is about 30 % lower than in the ideal case due to losses within the metadevice. Note that the XOR function can be inverted to α XNOR β by providing an additional external phase-shift $\theta_{ext} = \pi$ to one of the input signals. Furthermore, a fixed input signal β of + or − could be used to map the phase-modulated signal α to an intensity-modulated signal with (NOT α) or without (IDENTITY α) inversion.

Table 3-1 **Logical functions between mutually coherent, equal intensity, phase-modulated input bits α and β ($I_\alpha = I_\beta = 1$).**

Input phase states		Ideal output intensities $I_\gamma = I_\delta$	
		$\theta_{ext} = 0$	**$\theta_{ext} = \pi$**
α	**β**	**α XOR β**	**α XOR β**
+	+	**0**	**1**
+	−	**1**	**0**
-	+	**1**	**0**
-	−	**0**	**1**

The network can also perform signal processing operations analogous to logical functions on intensity-modulated input data. The simplest example is a NOT function. Such inversion of an intensity-modulated signal α is achieved by leaving input beam β always on with its phase adjusted such that coherent absorption will occur for simultaneous illumination of the metasurface from both sides ($\theta_{ext} = 0$). Input pulses α (logical 1) will be coherently absorbed resulting in low output (logical 0). On the other hand, low input signals α (logical 0) will allow light from input β to reach the outputs (logical 1). For an ideal metadevice, the expected output intensities are 0 and 25 % of the input intensity, respectively; our experimental device achieves about 5 and 23 % at a modulation frequency of 10 kHz, which is more than sufficient to distinguish the logical states (Figure 3-5(b)).

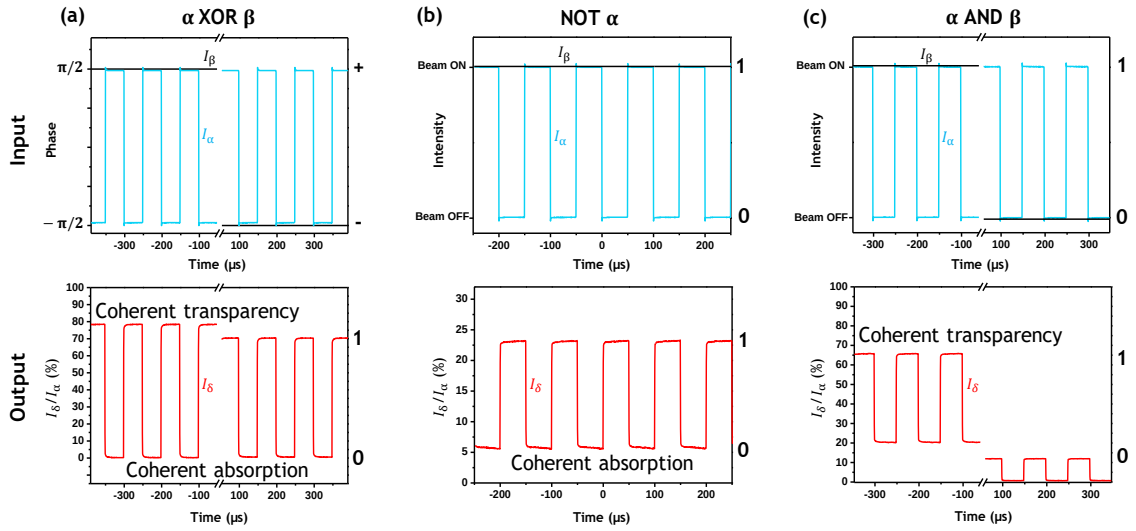

Figure 3-5 **All-optical logic functions measured at 10 kHz at a wavelength of 1550 nm.** **(a)** XOR function between phase-modulated input signals α and β producing an intensity-modulated output based on coherent absorption of identical bits and coherent transparency for opposite bits. **(b)** NOT function on a single intensity-modulated signal α. The inversion of signal α in the presence of beam β (which is always on) results from coherent absorption of incoming signal pulses when the metasurface is located at a standing wave anti-node. **(c)** AND function between intensity-modulated signals α and β resulting from coherent transparency of the metasurface for simultaneous illumination from both sides when the metasurface is located at a standing wave node. The logical states are indicated on the right-hand side of each graph. Minor signal distortions are due to the limited bandwidth of the waveform generator.

While the NOT function was based on coherent absorption, an AND function between binary intensity-modulated signals can be realized by exploiting coherent transparency. In

this case, a phase shift is applied to one input signal, such that simultaneous illumination of the metasurface from both sides leads to coherent transparency ($\theta_{ext} = \pi$). For an ideal device, this would lead to 100 % output intensity for interaction of two pulses on the metasurface and at least 4× lower output intensity for any other combination of input bits (Table 3-2). Experimentally we observe the AND function with more than 3× contrast between the logical output states at a modulation frequency of 10 kHz. In principle, other logic functions including XOR and OR for intensity modulated signals can be realized for suitable choices of θ_{ext} [64].

Table 3-2 **Logical function α AND β between mutually coherent, intensity-modulated input bits α and β.**

Input phase states		Ideal output intensities $I_\gamma = I_\delta$
		$\boldsymbol{\theta_{ext} = \pi}$
$\boldsymbol{\alpha = I_\alpha}$	$\boldsymbol{\beta = I_\beta}$	**α AND β**
1	**1**	**1**
1	**0**	**0.25**
0	**1**	**0.25**
0	**0**	**0**

3.5 Gigabits per second and beyond

In practical systems, optical signals transmitted by optical fibres are modulated at GHz frequencies rather than kHz, and also make use of a range of optical wavelengths. I therefore tested the metadevice at modulation frequencies 5–6 orders of magnitude higher than presented in Figure 3-5 and at wavelengths ranging from 1530 to 1565 nm (telecommunications C-band), as illustrated in Figure 3-6, Figure 3-7 and Figure 3-8. To this end, the output of the fibre interferometer was amplified with an erbium-doped fibre amplifier (EDFA) which provided an average output power of 1 mW. This conveniently ensures that the threshold power between logical 0 and logical 1 will always be close to 1 mW. Figure 3-6(a) shows the XOR function on phase modulated signals (as described

above) now at a modulation frequency of 1.2 GHz, while Figure 3-6(b) shows the NOT function on an intensity-modulated signal also at 1.2 GHz. An AND function was realized by intensity modulation of the laser light entering the interferometer (i.e. modulation before the 50:50 splitter shown in Figure 3-2) and the introduction of a path difference in the interferometer arms to delay the modulated signals α and β relative to one another as illustrated by Figure 3-6(c). This is equivalent to an intensity-modulated bit sequence 0011 in channel α and 1001 in channel β, resulting in an output 0001, i.e. α AND β, in the detected output channel.

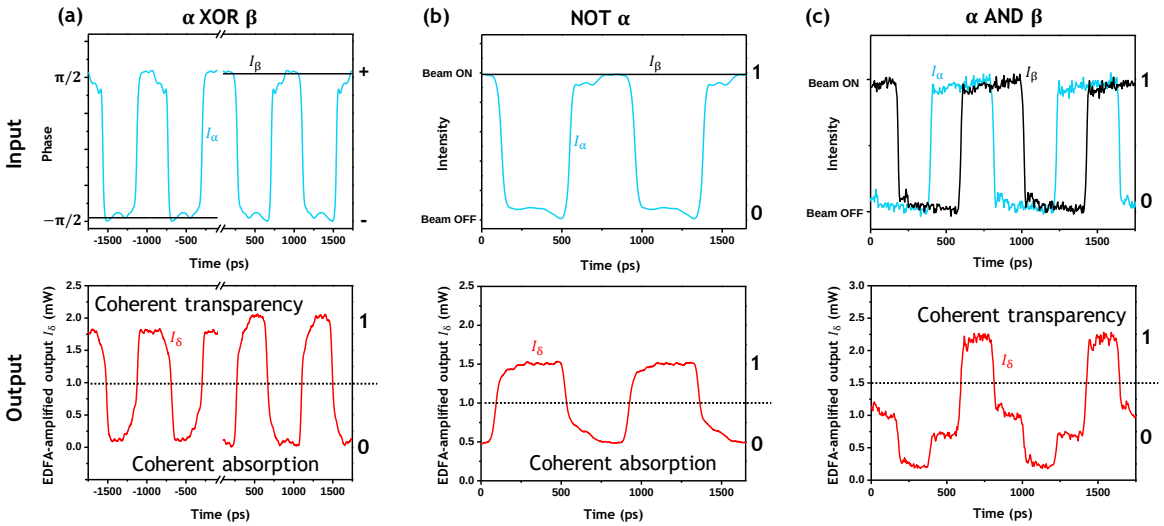

Figure 3-6 **All-optical logic functions measured at 1.2 GHz at a wavelength of 1550 nm.** **(a)** XOR function between phase-modulated input signals α and β producing an intensity-modulated output based on coherent absorption of identical bits and coherent transparency for opposite bits. **(b)** NOT function on a single intensity-modulated signal α in the presence of a constant beam β, resulting from coherent absorption of incoming signal pulses when the metasurface is located at a standing wave anti-node. **(c)** AND function on two intensity-modulated signals α and β resulting from coherent transparency of the metasurface for simultaneous illumination from both sides when the metasurface is located at a standing wave node. The elevated noise level in (c), as compared to (a), (b), is due to a change in the experimental configuration (described in section 3.7). The logical states are indicated on the right-hand side of each graph.

Figure 3-7 shows the NOT function of the switching network at a frequency of 10 GHz. The periodic electrical input signal α was generated with an arbitrary waveform generator (the electrical signal is used to drive an electro-optic modulator) and is equivalent to a bit sequence of 1011, which is inverted to become 0100 at a rate of 40 Gbit/s.

Measurements at wavelengths from 1530 to 1565 nm show successful signal inversion, thereby illustrating the broadband nature of the underlying coherent absorption effect across the full wavelength range of the tuneable laser used in the experiment. With 50 μW peak power in each input channel and a 25 ps pulse duration per bit, the modulator's energy consumption is 2.5 fJ per bit, which corresponds to about 20,000 photons per bit. Given that

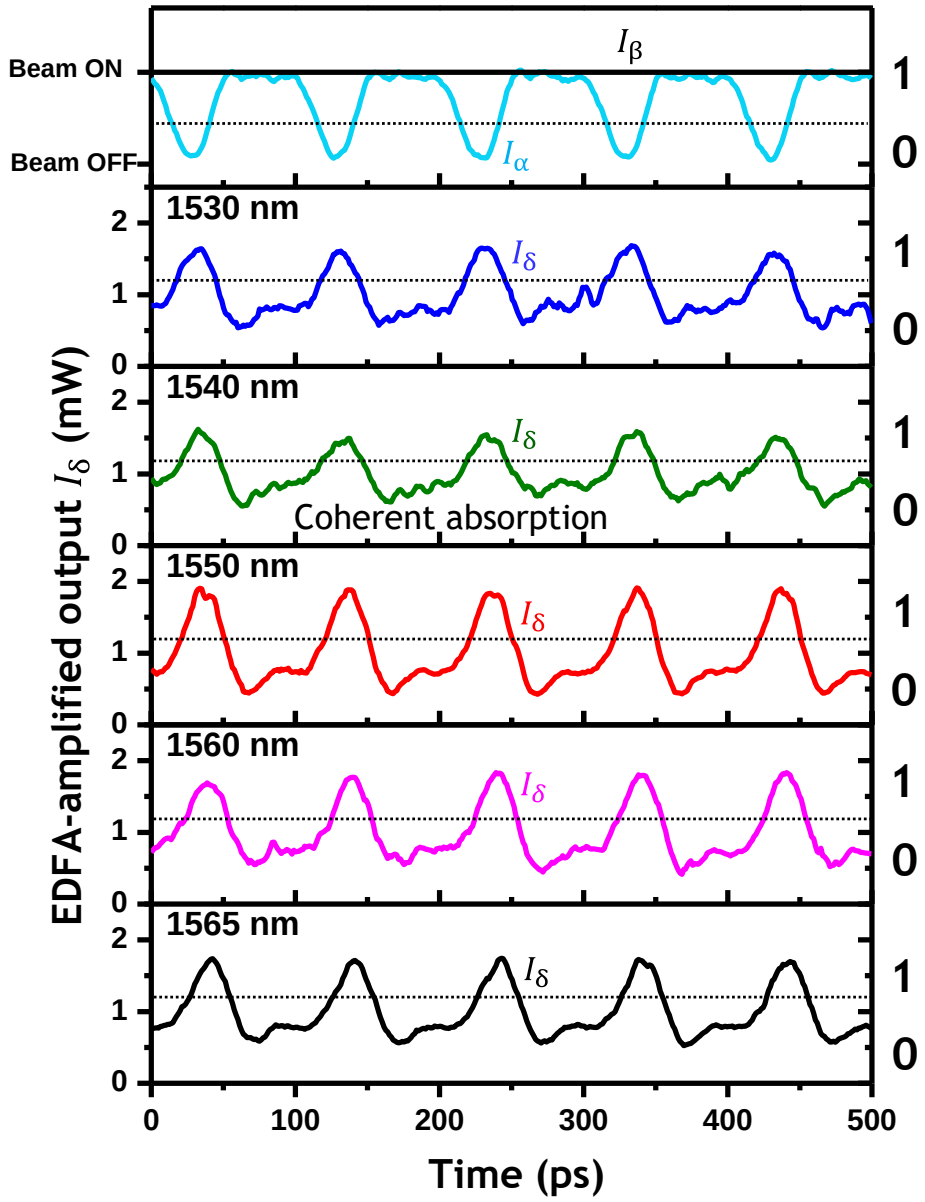

Figure 3-7 **All-optical logic function NOT α at 40 Gbit/s at wavelengths from 1530 to 1565 nm.** The input signal corresponds to an intensity-modulated bit pattern 1011 repeating at 10 GHz (top); corresponding output traces for different wavelengths (below) show that the metadevice inverts the bit pattern in all cases. Beam β is continuously in the on state (logical 1). The logical states 1 and 0 are indicated on the right hand side and separated by a horizontal dotted line on each graph.

coherent absorption of single photons has been demonstrated [35], we expect that energy consumption in the attojoule per bit regime should be possible with a sufficiently sensitive detection system.

In devices where the bit sequence of data affects the transmission quality of the signal or the all-optical functions they perform, one can use pseudorandom binary sequences (PRBS) for testing the magnitude of signal distortion. In general, an arbitrary waveform generator creates an electrical signal, which is used to drive an electro-optic modulator or the device itself. As discussed above, the operation principle of coherent control relies on a truly linear process, thus the response is relative fast (tens of fs), and consequently, the performance of the metadevice is expected to be independent of the bit sequence. Therefore, one would expect that if a PRBS signal drives the light-matter interactions within the ultrathin absorber the output signal would be intact.

I performed an experiment where a PRBS signal drives the intensity modulator and controls the interference pattern within the absorber. A PRBS sequence of 127 bits (PRBS-7) was launched into the intensity modulator that is installed in one interferometer arm, see Figure 3-2. Here, as previously, I show an inversion of the input signal resulting in a NOT logic function but this time the signal pattern/sequence is a PRBS-7. The all-optical logic function is performed at a rate of 40 Gbit/s (25 ps per bit), see Figure 3-8. One can see that the signal inversion is independent of the bit sequence as well as of the wavelength of the input beam. I tested our device at wavelengths between 1530 and 1565 nm.

The modulation results obtained at GHz frequencies are similar to those obtained at kHz frequencies. At GHz frequencies, some distortion is apparent in both the signals used to drive the phase and intensity modulators as well as the measured output signal, where contrast is slightly reduced. These distortions arise from the frequency response and background noise of the modulators and amplifiers used in the experiments. In particular, the distortions that are visible in the output signals in Figure 3-8 are also present in the modulated input signal, implying that they arise from imperfections of the waveform generator and the electro-optic modulator. While our experimental equipment does not allow us to test the performance of the modulator in the fibre environment beyond 40 Gbit/s, we expect that the switching network with metamaterial absorber can in principle operate at much higher frequencies. Indeed, the underlying phenomena of coherent absorption and coherent transparency in plasmonic metamaterials occur on timescales as short as 10 fs,

implying a potential bandwidth in the order of 100 THz [36]. However, such bandwidth will be difficult to realize in a fiberized switch due to dispersion limitations of the optical fibres.

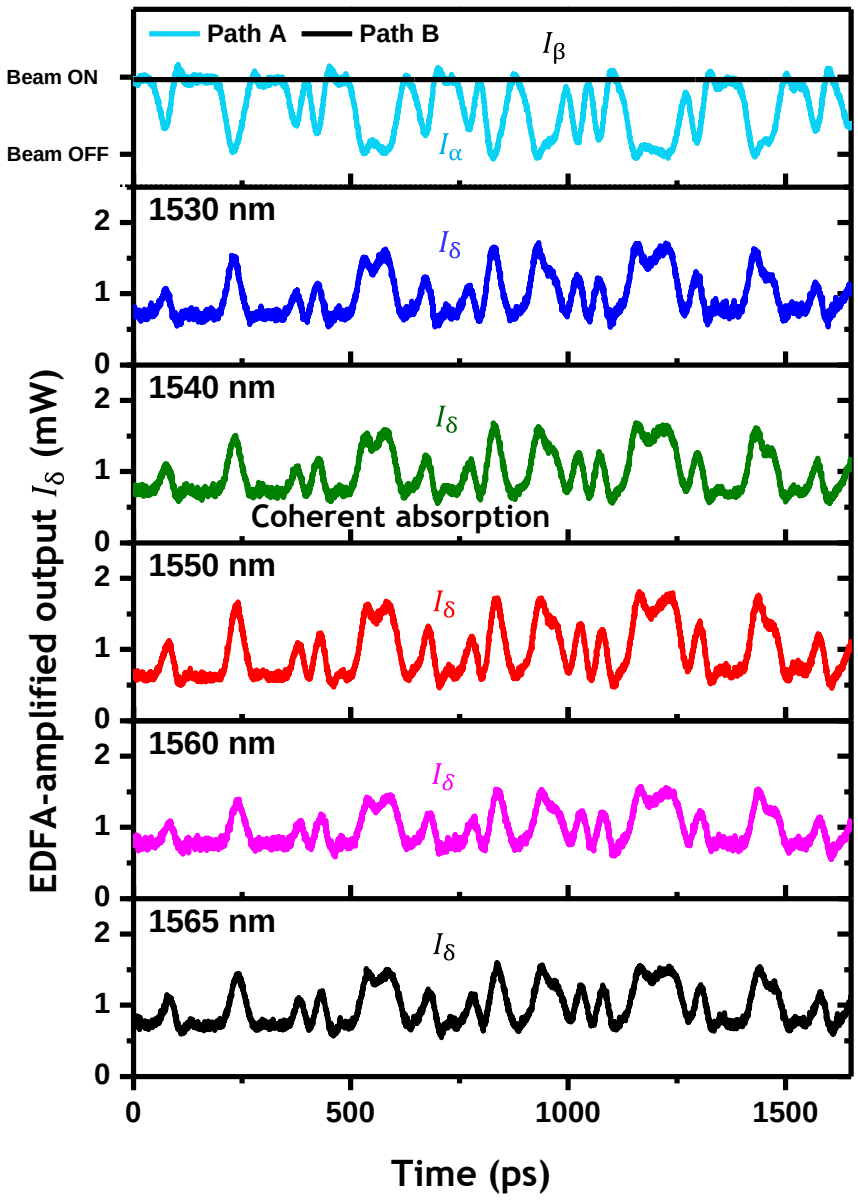

Figure 3-8 **All-optical logic function NOT α at 40 Gbit/s at wavelengths from 1530 to 1565 nm tested with PRBS-7 sequence.** The input signal corresponds to an intensity-modulated PRBS-7 bit sequence (top); corresponding output traces for different wavelengths (below) show that the metadevice inverts the bit pattern in all cases. Beam β is continuously in the on state. The metadevice was tested at wavelengths between 1530 and 1565 nm.

3.6 Conclusions

Even though I report a proof-of-principle demonstration, my results show that the coherent interaction of light with light on ultrathin films can be used to perform signal processing functions with high bandwidth and high contrast on signals carried by telecoms fibres. Improved device performance would result from a more symmetric design wherein the nanoscale thickness absorber is in contact with the same material on both sides, which may be achieved for instance by depositing a thin glass layer over the metasurface or via a bespoke splicing technique. The metamaterial design itself could also be improved to achieve 50% single-beam absorption and identical 25% transmission and reflection characteristics from both sides as well as polarization independence. Another option may be to replace the metamaterial with multi-layer graphene [35, 66].

All-optical signal processing applications based on coherently controlling the absorption of light with light promise extremely high bandwidth and extremely low energy requirements, but they will require mutually coherent signals and phase stability. Mutual coherence is most easily achieved in local systems, where multiple signals are derived from the same seed laser. Indeed, as locally coherent networks become part of the mainstream telecommunications agenda [68-70], coherent all-optical data processing may become a realistic proposition, particularly in miniaturized integrated optics and silicon photonic chips [71], where phase stability is more easily achieved than in large-scale fibre networks. In order to go beyond simple single-step logical functions, cascading of multiple coherent operations will also need to be explored. Such cascading is likely to require signal regeneration techniques as the XOR function converts phase-shift keying to amplitude shift keying (though in principle without insertion loss and with unlimited contrast), while the AND function suffers from limited contrast of 6 dB (though in principle without insertion loss) and the NOT function suffers from insertion loss of 6 dB (in principle with unlimited contrast). Recently, an example involving cascading of two coherent operations is published [72] (see Chapter 5).

It is notable that metasurfaces can be engineered to enable a broad range of switching and control functions, which may be used to implement various signal processing functionalities [31, 56, 64]. Devices based on coherent perfect absorption (as considered

here) and lossless devices are limiting cases among a much wider range of possibilities. Beyond all-optical data processing and small-signal amplification, potential applications of coherent metadevices include coherence filtering [48].

The switching network demonstrated here is one example among many opportunities arising from fibre-integration of metasurfaces, which could also be used to control, for example, focusing, polarization, spectral characteristics, propagation direction and angular momentum of light [73-75].

In summary, we report a metamaterial-based fiberized switching network for all-optical signal processing that is compatible with optical telecommunications fibre components. The multi-functional switch can perform effectively-nonlinear signal processing functions including input/output relations analogous to XOR, AND and NOT operations, and the underlying mechanism of coherent transparency and coherent absorption is compatible with single-photon signals [35] and 100 THz bandwidth (tested with 10fs pulses in free space experiments) [36]. I therefore anticipate that such fiberized metadevices may provide solutions for quantum information networks as well as orders-of-magnitude improvements in speed and energy consumption over existing nonlinear approaches to all-optical signal processing in coherent information networks.

3.7 Methods

Experimental metadevice characterization was performed using the interferometer arrangement presented in Figure 3-2. All fibre components were based on Panda-style polarization-maintaining single-mode fibres. In all cases the incident electric field was oriented parallel to the symmetry axis of the metamaterial nanostructure (slow axis of the fibre). Measurements at kHz frequencies used the 180 μW output of a fibre-coupled 1550 nm CW laser diode and were recorded using InGaAs photodetectors and an oscilloscope (Agilent Technologies DSO7104A). They were calibrated by taking into account the insertion losses of fibre components, such that I_α, I_β, I_γ and I_δ in Figure 3-3, Figure 3-4 and

Figure 3-5 correspond to the intensities entering and leaving the metadevice's fibre connectors. The peak input power at the metadevice input connector $I_\alpha = I_\beta$ was 10 μW. The input signal modulators used were low-loss electro-optical 10 Gbit/s phase and intensity modulators (EOspace) driven by a waveform generator (AM300 by Rohde & Schwarz). Measurements at GHz frequencies used a fibre-coupled tuneable CW laser (ID Photonics CoBrite-DX4). Here the EDFA-amplified output power was detected by an oscilloscope (Agilent Infiniium DCA-J 86100C) as described in the previous sections. The peak input power at the metadevice input connector $I_\alpha = I_\beta$ is ~100 μW in the case of Figure 3-6(a-b), 30 μW in Figure 3-6(c) and 50 μW in Figure 3-7 and Figure 3-8. The modulators used were low-loss electro-optical 10 Gbit/s phase and intensity modulators (EOspace) driven by an arbitrary waveform generator (Tektronix AWG7122C) and a radio frequency amplifier (LA Techniques) in the case of Figure 3-6(a-b), and an arbitrary waveform generator (SHF 12100 B) in the case of Figure 3-2 eye diagrams, Figure 3-6(c), Figure 3-7 and Figure 3-8.

Chapter 4 Picosecond all-optical switching and dark pulse generation in a fibre-optic network using a plasmonic metamaterial absorber

Part of the work in this chapter has been published as: **Picosecond all-optical switching and dark pulse generation in a fibre-optic network using a plasmonic metamaterial absorber.** A. Xomalis, I. Demirtzioglou, Y. Jung, E. Plum, C. Lacava, P. Petropoulos, D. J. Richardson, and N. I. Zheludev. *Appl. Phys. Lett.* **113**, 051103 (2018) [76]. The fabrication of metasurfaces on optical fibre tips and optical characterisation of the metadevice were done entirely by myself, however, I acknowledge help of Dr. Y. Jung with encapsulation of fibre metamaterials and assistance of I. Demirtzioglou during experiments with picosecond pulses. Other co-authors contributed with advice and/or to supervision and writing of the article.

4.1 Introduction

In the previous chapter, the integration of fibre metasurfaces and fibre technology was discussed. I reported proof-of-principle demonstrations of all-optical switching and data processing using such encapsulated devices. My findings shown that truly linear approaches may have advantages over nonlinear methods, mainly regarding power consumption. There are recent demonstrations which prove that the principle of coherent control of absorption is compatible with single photons signals [35] and with THz bandwidth [36] in free-space schemes. Although, for realization of applications within telecommunications networks a great limitation exists in terms of speed due to fibre dispersion.

In this chapter, I discuss the practicability of data processing with THz bandwidth within fibre information networks. My findings have shown that such bandwidth is feasible and fully compatible with my devices. Coherent interaction of two light waves on a film of subwavelength thickness provides remarkable opportunities for controlling intensity and polarization of light beams as well as all-optical image processing. Here I show that such interactions can be used for optical dark pulse generation and basic all-optical signal processing in fully fiberized coherent information networks with 1 THz bandwidth. With an encapsulated plasmonic metamaterial absorber operating in the telecommunications C-band, I demonstrate switching and dark pulse generation with 1 ps laser pulses. To my knowledge, this is the fastest all-optical switching in the fibre environment reported so far. Lastly, I study the interactions between pulses of different duration within the plasmonic metasurface, thus paving the way for pulse shaping applications. Importantly, I demonstrate that this allows conversion of an arbitrary pattern of bright pulses into dark pulses, e.g. for pulse shaping applications where the bandwidth, repetition rate and shape/envelope of the initial (input) pulses should not limit the performance. In general, dark pulses within a CW background (or in a longer pulse envelope in our case) is preferable compared to bright pulses for long signal transmission. Their fundamental difference lies on the peak power difference. Bright pulses have high peak power and low average power while rapid dips within a CW signal (dark pulses) have low peak power and high average power. As it is shown below, high peak power gives rise to nonlinear effects that can distort pulses and thus, the information transmitted.

Intentionally, 1ps pulses were selected for my experiments since shorter pulses will experience greater dispersion. Section 3.2 of the "Nonlinear Fiber Optics" book of Agrawal G. [77] can give us an estimation for the dependence of dispersive effects of pulse duration, as well as nonlinear effects, which can cause pulse broadening/distortions. Here, we introduce the following quantities, dispersion length L_{D} and nonlinear length L_{NL}:

$$L_{\mathrm{D}} = \frac{{T_o}^2}{|\beta_2|} \quad \text{and} \quad L_{\mathrm{NL}} = \frac{1}{\gamma_{\mathrm{NL}} P_o},$$

where T_o is the input pulse width, β_2 the group-velocity dispersion (GVD) parameter (its sign, positive/negative depends on whether the wavelength of operation is below/above the zero dispersion wavelength of the fibre), γ_{NL} the nonlinear parameter of the material and

P_o the peak power. L_{D} and L_{NL} provide length scales over which dispersive and nonlinear effects become important during pulse propagation. Consequently, when $L_{\mathrm{D}} \ll L$ *and* $L_{\mathrm{NL}} \ll L$, where L is propagation length, the pulses will experience neither dispersive nor nonlinear effects of significant magnitude. For example, a pulse with peak power of 1 mW at wavelength of 1550 nm with γ_{NL} = 2 $(\mathrm{Wkm})^{-1}$ and β_2= 20 ps^2/km (typical values for telecoms fibres) and pulse width of either 1 ps or 10 fs would have the same L_{NL}= 500 km length but L_D would be 50 m and 0.005 m, respectively. This shows that 10 fs pulses experience dispersion effects within a much shorter distance of propagation compared to 1 ps pulses. This can give us a rough idea for the conditions that one should carefully choose when working with short light pulses within fibre communication networks. It also indicates that local all-optical signal processing schemes based on fibre-optics could achieve THz bandwidth, especially when using the low peak powers that are permitted when exploiting coherent control of light with light.

4.2 Linear optical switching with 1 THz bandwidth

Nonlinear optics has given rise to all-optical signal processing by allowing optical signals to modulate one-another [51]. However, nonlinear methods require sufficient intensity to achieve a significant nonlinear response and face trade-offs between speed and magnitude of the nonlinearity involved [34, 52-55, 78, 79].

In contrast, all-optical processing of mutually coherent signals does not require optical nonlinearity [56]. Similarly, nonlinear dark pulse generation [80-89] and nonlinear dark soliton propagation [80, 90-93] in optical fibres at high intensities are well-known, but the shortest dark pulses have been generated by linear methods in free space [36, 91]. Recent developments in dark pulse generation and coherent all-optical signal processing exploit the fact that modulation of light with light may be derived from the interaction of mutually coherent optical signals in a linear material of substantially subwavelength thickness [31]. Such all-optical modulation allows control over the absorption of light from “coherent perfect absorption” to “coherent perfect transmission” and is intensity-independent down to

single photon signal levels [35]. It has enabled 11 fs dark pulse generation [36], polarization modulation, image processing and various logic functions in free space [31]. The concept was applied to demonstrate NOT, XOR and AND functions at up to 40 Gbit/s in a fibre-optic interferometer [50] (as discussed in Chapter 3).

Standard single-mode optical fibres transmit 1 ps optical pulses in the C-band over several meters without any significant temporal broadening due to dispersive effects (see section 4.1). This allows the realization of local fibre networks that exploit coherent techniques for controlling light with light at high bandwidths. Here I demonstrate that coherent absorption and coherent transparency enable controlled absorption and transmission of mutually coherent 1 ps pulses in a fibre-optic network containing a pigtailed metadevice at wavelengths ranging from 1530 to 1560 nm. My measurements imply a modulation bandwidth of at least 1 Tbit/s and indicate that the all-optical logic functions [50] may be performed at this rate (or even faster). Using 1 ps pulses to trigger coherent absorption of the central part of few ps pulses, we generated 1 ps dark pulses. Such linear in-fibre dark pulse generation is compatible with arbitrarily low intensities and may be used to convert arbitrary patterns of bright pulses into dark pulses.

The all-optical modulator is based on the linear interaction of light with light in a thin absorber. Two co-polarized, counter-propagating and mutually coherent input pulses in channels α and β interact in a lossy metasurface of deeply subwavelength thickness resulting in two output pulses in channels γ and δ. A standing wave forms as coherent input pulses of parallel linear polarization and equal intensity pass through each other. The metasurface is sufficiently thin to be placed at a node of the standing wave, where the electric field is zero due to destructive interference, or at an anti-node, where the electric field amplitude is enhanced by constructive interference. When it is located at a standing wave node, the light pulses cannot interact with the metasurface, rendering the structure perfectly transparent. In contrast, the pulses will interact strongly with the metasurface when it is placed at a standing wave anti-node, resulting in enhanced absorption. In the case of an ideal planar absorber this allows, in principle, the absorption of the optical pulses to be modulated from 0% to 100% [31] (see subsection 2.2.2).

The lossy metasurface is the functional element within a fibre-optic metadevice with standard pigtailed FC/APC connectors which ensure compatibility with telecommunication fibre components (Figure 4-1(a)). As described in more detail in section 2.3, the metasurface was fabricated on the end face of a flat-cleaved single-mode polarization-maintaining optical

fibre. A 70-nm-thick layer of gold was thermally evaporated onto the fibre's end face followed by focused ion beam milling of a 25 × 25 μm^2 array of asymmetrically split ring apertures through the gold layer covering the fibre core with the symmetry axis of the metasurface aligned to the slow axis of the Panda style fibre (Figure 4-1(b)). The metamaterial-covered fibre was then coupled with a second cleaved optical fibre. To

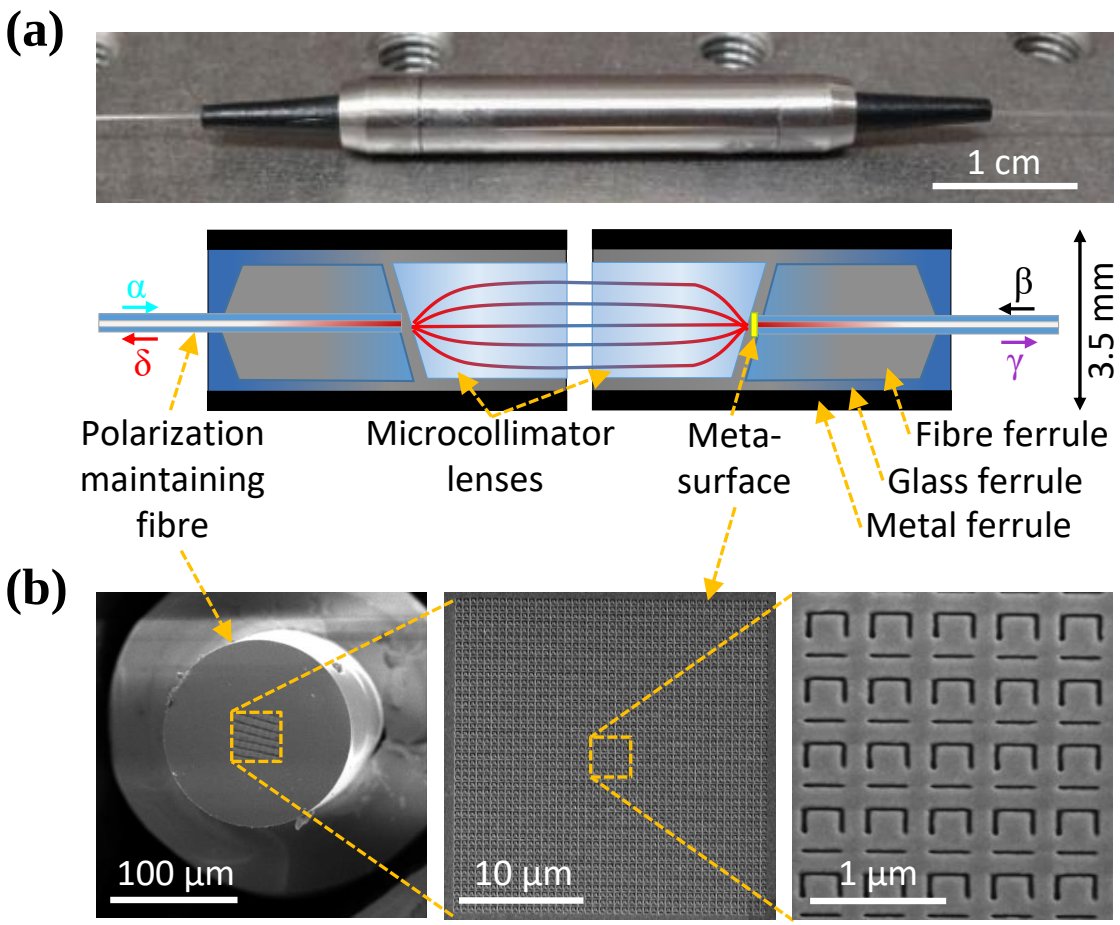

Figure 4-1 **Fibre-optic metadevice for signal processing and dark pulse generation based on coherent absorption. (a)** Photograph and schematic of the improved fibre-optic metadevice. Within the metadevice, coherent optical pulses in input channels α and β interact in a metasurface absorber, resulting in output pulses in channels γ and δ. **(b)** SEM images of the metamaterial absorber that consists of a nanostructured gold film of 70 nm thickness and covers the core area of a single-mode polarization-maintaining optical fibre.

maximize the coupling efficiency and for ease of alignment, the fibre output was collimated and then focused onto the core of the second fibre using two anti-reflection-coated microcollimator lenses (Figure 4-1(a)). The components were fixed in place with glass and metal ferrules and bonded with UV-cured adhesive. The resulting assembly was placed in a protective stainless steel package.

We characterized the functionalities of a polarization-maintaining fibre interferometer containing the metadevice (Figure 4-2). A fibre-coupled tunable continuous wave laser (Keysight 81940A) was launched into a frequency comb generator (OptoComb LP-5011), which produced 1 ps optical pulses at a repetition rate of 10 GHz. Then the pulsed signal was amplified and split into the two interferometer arms. One arm contained an optical delay line for adjusting the relative arrival times of pulses in channels α and β at the metasurface. The delay line was combined with a polarization controller and a polarization beam splitter that were used to monitor and minimize the unwanted orthogonal polarization component. The two arms were recombined within the metadevice and the output signals were detected via circulators using a fast sampling oscilloscope (EXFO PSO-102). Variable optical attenuators were used to prevent optical damage on the metasurface and to balance the peak power of the optical pulses in the two arms. In all experiments, the incident electric field was oriented parallel to the symmetry axis of the metasurface. While our fibre interferometer is stable on second timescales, which is sufficient for proof-of-principle demonstrations, we note that practical applications would require active stabilisation of the optical path lengths to prevent phase drift in the interferometer.

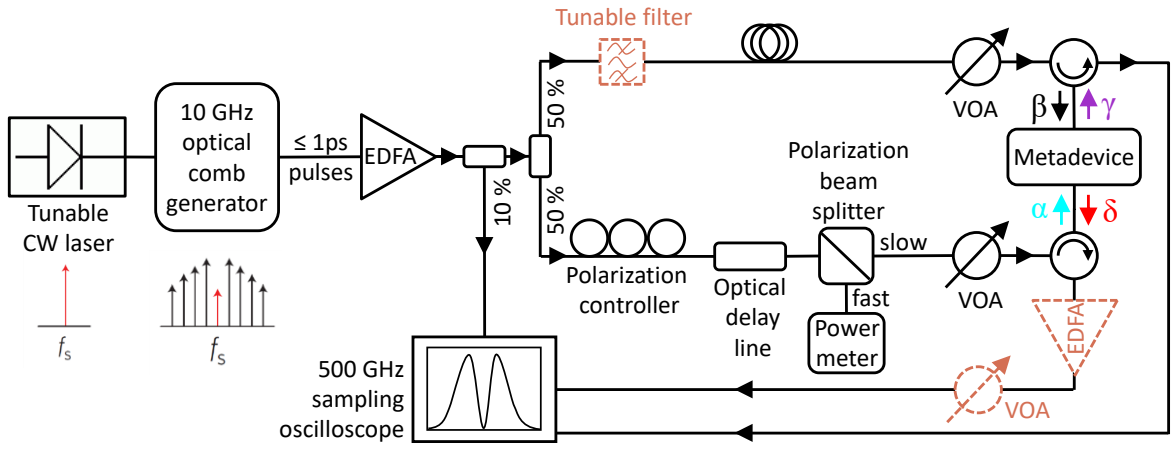

Figure 4-2 **Coherent signal processing and dark pulse generation.** Experimental setup for controlled absorption and transmission of 1 ps pulses (black lines) with additional components required for dark pulse generation and detection (brown dashed lines). VOA - Variable Optical Attenuator, EDFA - Erbium Doped Fibre Amplifier.

The absorption of coherent optical pulses entering the metadevice depends on the phase difference between the input pulses at the position of the metasurface. It is instructive to consider the limiting cases, which are illustrated by Figure 4-3 for equal-intensity input pulses of 1 ps duration, 1550 nm central wavelength, 10 GHz repetition rate and 0.4 mW

average power in channels α and β (Figure 4-3(a)). Destructive interference of these input pulses on the metasurface causes negligible light-metasurface interaction and thus little absorption, resulting in large output pulses in channels γ and δ (Figure 4-3(b), top). In contrast, constructive interference on the metasurface enhances the light-metasurface interaction, causing strong absorption of the input pulses that results in suppression of the output pulses (Figure 4-3(b), bottom). Thus, the phenomena of coherent transmission and coherent absorption allow both 1 ps optical pulses to be either simultaneously transmitted or simultaneously absorbed in the metadevice.

Linear modulation of light with light is well-known in interferometers, where mutually coherent signals are usually combined by an essentially lossless beam splitter or fibre coupler. For comparison, I repeated the same experiment using a 50:50 fibre coupler (Figure 4-3(c)) instead of the metadevice (Figure 4-3(b)). Both the metadevice, which may be seen as approximating an ideal lossy beam splitter [44], and the 50:50 fibre coupler, which may be seen as approximating an ideal lossless beam splitter, allow modulation of the output pulses in channels γ and δ. However, the modulation mechanisms and the resulting relationships between the output signals are different. The coupler modulates light by redistributing power without losses in the ideal case, thus maximizing one coupler output will minimize the other (cases I and II in Figure 4-3(c)). In contrast, the metadevice modulates light by controlling absorption, resulting in output signals that are simultaneously maximized or simultaneously minimized (Figure 4-3(b)). Therefore, four-port data processing devices based on coherent interactions on lossless and lossy beam splitters are fundamentally different and may be used in single or dual output signal processing architectures, respectively. Conventionally, four-port devices are used in cascading schemes, where the information experiences multiple processing steps. Although, if one reduces the "useful" outputs from two to one this reduces the capacity of the processing network by a factor of two. Thus, our metadevices may find applications in schemes where the capacity of the network plays crucial role.

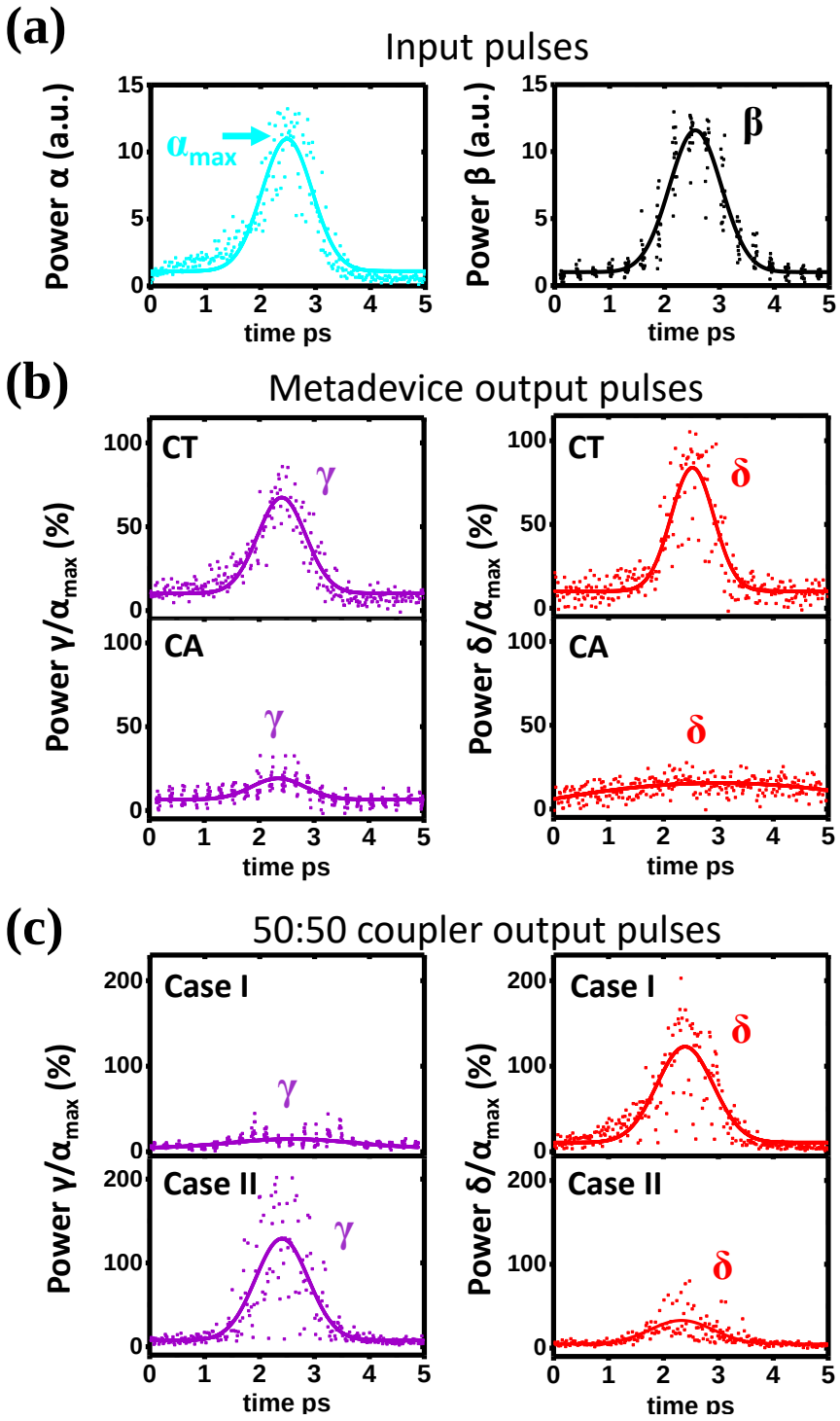

Figure 4-3 **Controlled absorption and transmission of 1 ps pulses.** **(a)** Power profiles of the coherent input pulses in channels α and β. **(b)** Power profiles of the output pulses in channels γ and δ in the cases of destructive (top) and constructive (bottom) interference on the metasurface absorber. These cases correspond to Coherent Transmission (CT) and Coherent Absorption (CA), respectively. **(c)** Power profiles of the output pulses in channels γ and δ measured after replacing the metadevice with a low-loss 50:50 fibre coupler in case of constructive interference of the input pulses in output channel δ (Case I) or γ (Case II). For clarity, all pulses are presented with Gaussian fits (lines).

4.3 Broadband signal processing and optical characterization of the metadevice

To characterize the performance of the switching network I introduced the notion of modulation contrast, which is the ratio between peak powers in an output channel for the coherent transmission and absorption regimes. An ideal metadevice without coupling losses, that could provide infinite contrast for both outputs, would contain a metasurface that transmits and reflects 25% and absorbs 50% of any single input signal [31]. The asymmetric construction of our metadevice, that is based on a metasurface fabricated on the glass/air interface of a cleaved optical fibre, results in different optical properties for input signals in channels α and β (Figure 4-4(a)). However, the asymmetry is small around the telecommunications C-band that covers the 1530 nm – 1565 nm wavelength range. For example, a single input signal of 1550 nm wavelength in channel α (β) will experience about 15% (15%) transmission, 22% (20%) reflection and 63% (65%) losses including coupling losses. These optical properties vary slowly with wavelength indicating that the metadevice can operate over a broad spectral range. Indeed, measurements of the peak power ratio of coherently transmitted pulses to coherently absorbed pulses yield a modulation contrast of 2 to 5 (3-7 dB) for both output channels, γ and δ, for the entire 1530 to 1560 nm wavelength range that is accessible by our experimental setup (Figure 4-4(b)). Here, peak powers were determined by Gaussian fits (lines in Figure 4-3) in order to exclude statistical noise affecting the data points.

For characterization of the optical behaviour (reflection and transmission) of the metadevice, presented in Figure 4-4(a), my methodology is the following. Transmission measurements were obtained by launching light, from a tungsten-halogen light source with broadband radiation spectrum from 360 to 2600 nm wavelength, into the one port of the metadevice and plugging the other output into an optical spectrum analyser (OSA) where I can detect the light's spectrum directly, see Figure 4-5(a). For normalisation, I conducted the same measurement with an uncut fibre of the same specifications instead of the metadevice. Then assuming that losses associated with the connectors are similar in both cases (of the uncut fibre and the metadevice), I calculated the transmission of the metadevice only. In order to measure reflectivity, a 50:50 coupler and the OSA were used to detect light reflected from either the metadevice (see Figure 4-5(b)) or from a reference mirror consisting

of a cleaved fibre with a ~ 200-nm-thick gold film deposited on the cleaved end. The metadevice reflectivity was calculated as the ratio of the measurements on metadevice and reference mirror.

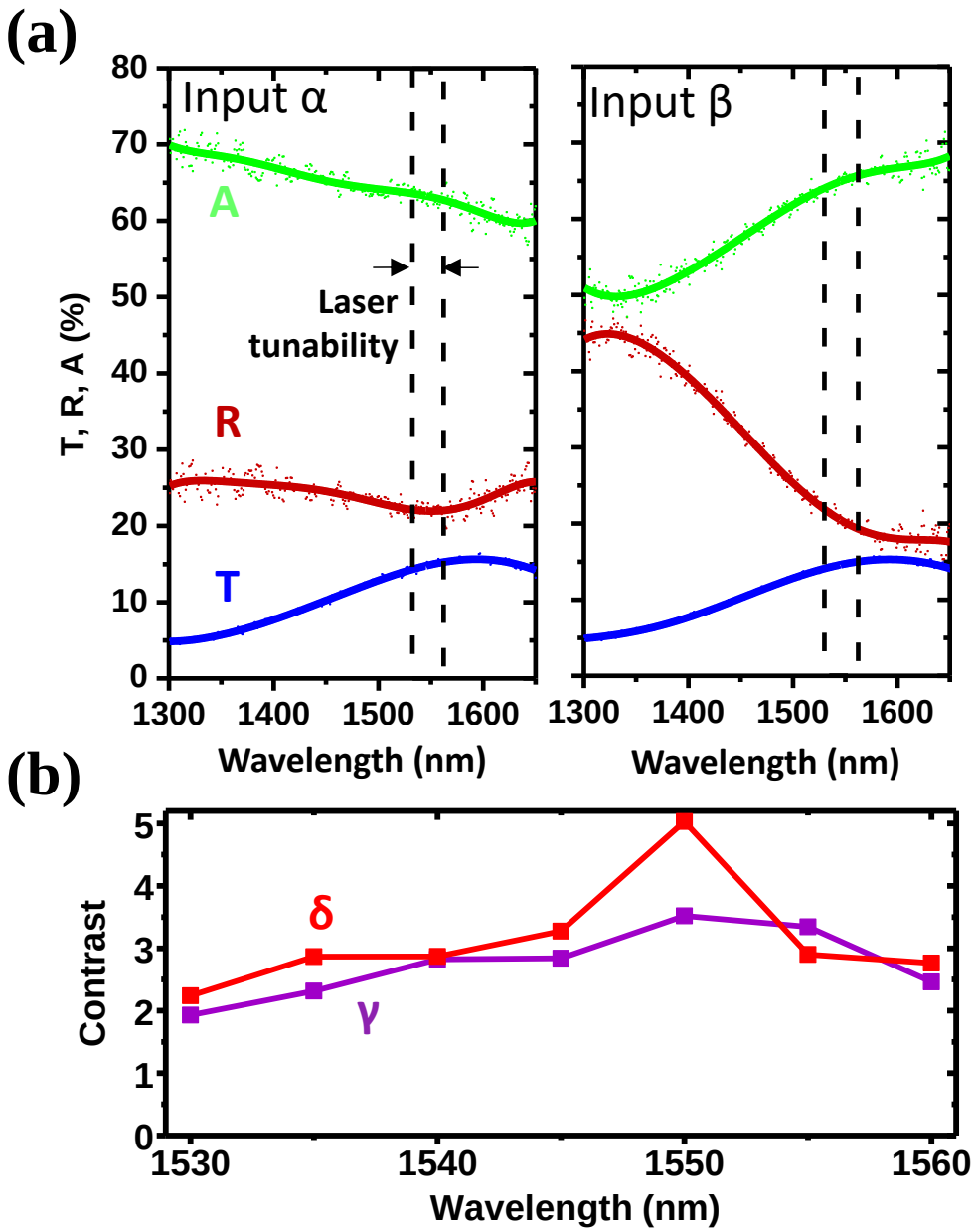

Figure 4-4 **Broadband signal processing.** **(a)** Metadevice transmission (T), reflection (R) and absorption (A) as measured with light entering the metadevice from either input α (left) or β (right). The data points are shown with polynomial fits (lines). **(b)** Modulation contrast observed for output channels γ and δ as functions of laser wavelength.

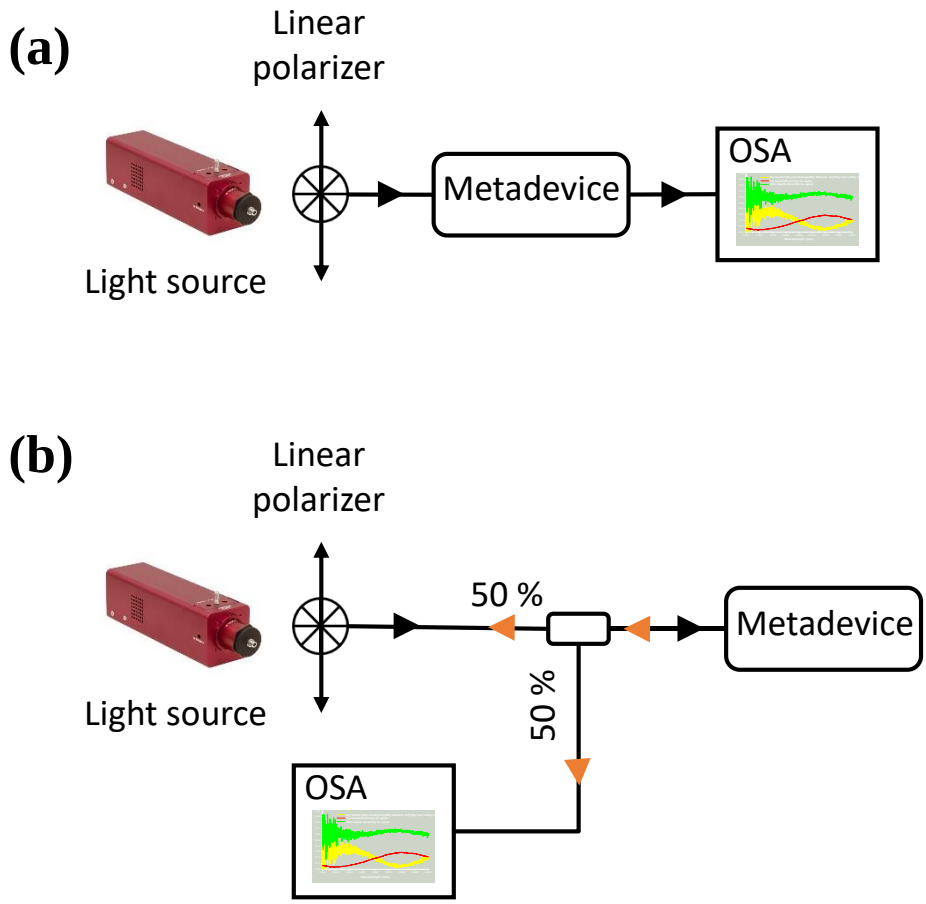

Figure 4-5 **Apparatus for measuring optical properties of metadevices.** The schematics show the experimental setup used for determination of **(a)** transmission and **(b)** reflection of the plasmonic metadevice. Brown arrows show the path of the reflected light. OSA - Optical Spectrum Analyser

I note that it is important to consider polarization. In single-mode fibres (for the time being I assume not polarization-maintaining fibres) the field distribution of the fundamental mode (HE_{11} or LP_{01} in linearly polarized mode notation) has three nonzero components E_x, E_y and E_z. Two of these (E_x or E_y) dominate. Thus, single-mode fibres are not truly single mode because can support two degenerate modes, which are polarized in two orthogonal directions [77]. In the ideal case, where a "perfect" symmetric core exists (along its entire length) and a stress-free situation (deformation acting on a material's body/lattice may cause optical anisotropy to an otherwise isotropic material leading to birefringence), light with polarization along the x-axis is not expected to be coupled to the y-polarization. However, small variations in the core shape are always present resulting in mixing of the two polarizations by breaking the mode degeneracy [77]. Fortunately, stress-induced anisotropy can be exploited to break degeneracy and this is the operation principle of polarization-

maintaining fibres. The larger the anisotropy of the fibre's cross section, the greater the difference in the propagation constants β_x and β_y for the two normal modes [94]. Here, we can define the magnitude of this effect as:

$$B_m = \frac{|\beta_x - \beta_y|}{\frac{2\pi}{\lambda}} = |n_x - n_y|,$$

where, B_m is the modal birefringence and n_x and n_y are modal refractive indices for the two orthogonal states. A typical value of modal birefringence for a Panda-style fibre is around ~ 10^{-4} [77]. B_m is strongly depended on the size of the stress-inducing elements. Moreover, the x- and y-directions comprise different refractive indices resulting in different light propagation velocities. The difference in velocities, between the two propagating light modes, makes it very difficult for optical energy to be cross-coupled, and, thus the polarization state of transmitted light is preserved. In the slow axis the effective refractive index is higher [in Panda-style fibres, the slow axis comprises stress rods of a different material (borosilicate glass, n=1.5007 at a wavelength of 1550 nm)] while the fast axis has a lower refractive index.

The use of polarization preserving fibres requires identification of the propagation axis (slow or fast) before light is launched into the fibre. For this reason, a linear polarizer mounted to a rotary mount installed after the light source was used, see Figure 4-5. During fabrication, the symmetry axis of the metasurface unit cell is aligned with the slow axis of the fibre (see section 2.3). By rotating the polarizer one can control the polarization of light impinged to the metasurface. In all measurements light launched into a fibre was polarized along the slow axis of the fibre.

Thereafter, one can calculate absorption (A) from the measured transmission and reflections coefficients as:

$$A = 1 - R - T,$$

where R and T stand for reflection and transmission, respectively. Since the metasurface unit cell period is of sub-wavelength size, light transmitted or reflected by the plasmonic

metasurface will experience no diffraction. Additional losses associated with coupling losses attributed to the collimating lenses as well as slight misalignment between the metasurface and bare fibres are included in the measured absorption coefficient.

4.4 Dark pulse generation

Here, I need to point out that our approach to create dark pulses differs from dark soliton generation. For the existence of temporal dark solitons a delicate balance between nonlinear (Kerr effect) and linear (group delay dispersion) effects must exist in order to cancel each other. In my case, dark pulse generation is based on temporal absorption in a plasmonic metasurface by well-adjusted interference of mutually coherent input light beams. The resulting dark pulses may be look similar although the physics is different. Moreover, I expect that the dark pulses resulting from my approach may be affected by linear effects (pulse broadening) mostly, since the power used is too low to generate the nonlinear effects that are required for solitons.

Opportunities for pulse shaping and dark pulse generation arise from combining mutually coherent signals of different envelope shape within the metadevice. I introduced a tuneable bandwidth spectral filter for pulse broadening in one interferometer arms (Figure 4-2) in order to study the interaction of 1 ps pulses with few ps pulses. The pulses in the input channels α and β had 1550 nm central wavelength, 10 GHz repetition rate and sub-mW average power.

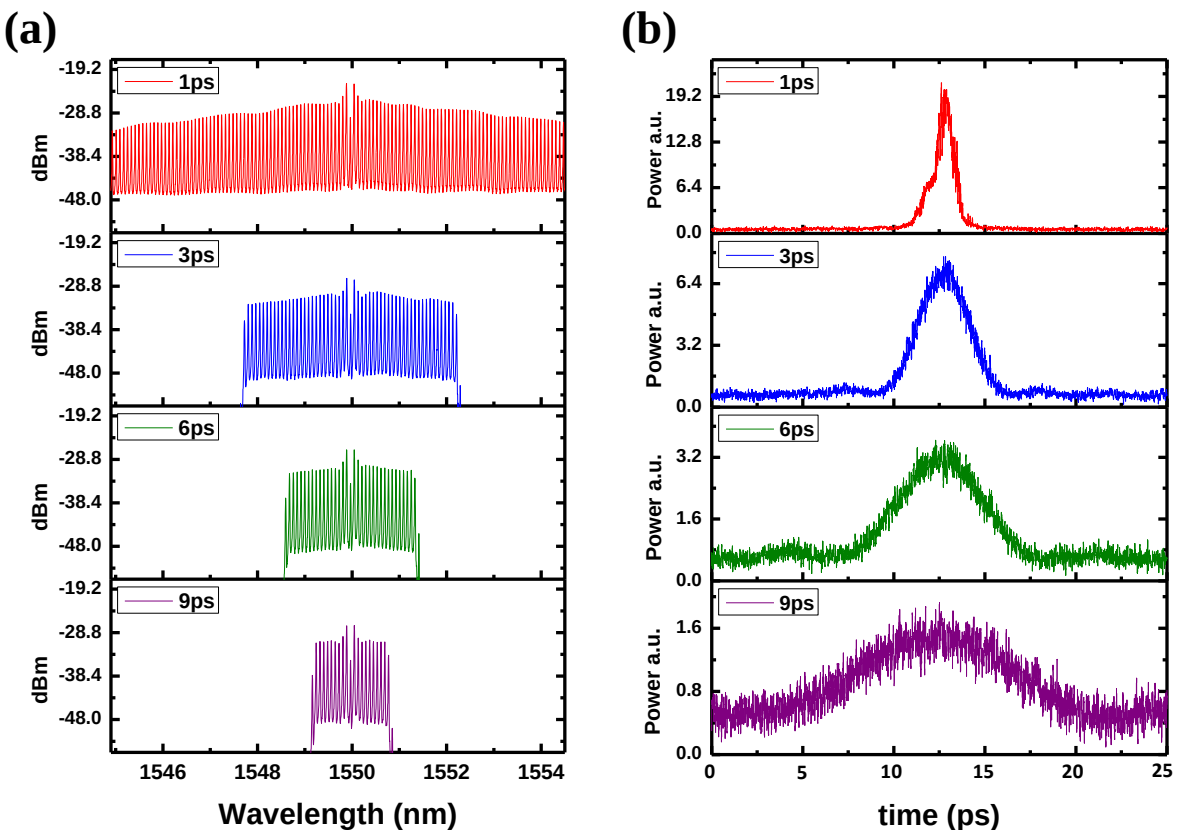

Figure 4-6 **The effect of spectral cropping on pulse duration. (a)** Optical spectrum of input channel β for four characteristic cases. The upper panel shows the spectrum of input light without spectral cropping. Panels below show optical spectra for different levels of pulse broadening. **(b)** Time traces of the pulses in input channel β with durations of 1, 3, 6 and 9 ps.

The effect of "spectral cropping" was studied thoroughly (Figure 4-6) for the identification of the ideal conditions for the experiment. As one decreases the spectral bandwidth of a pulse by spectral filtering the average optical power drops dramatically and thus, the traces in the time domain become noisier, see Figure 4-6(b). In order to compensate for this drop, the power amplification (using EDFAs) should be stronger. Here, my investigation focus on four different cases resulting in pulses with duration of 1, 3, 6, and 9 ps. Figure 4-6(a) shows the spectral range and Figure 4-6b) the corresponding time traces of pulses launched at the input channel β with and without (top panel in Figure 4-6(a-b)) spectral filtering. Pulses in the input channel α experience no broadening.

For clarity, I recorded the metadevice's higher-contrast output channel δ, that had to be amplified for detection due to the reduced peak power imposed by pulse broadening (Figure 4-7). The reflected 1 ps pulses from input channel α and the transmitted broadened pulses from input channel β were first separated in time, with the delay line (Figure 4-2),

and detected at output channel δ (top row of Figure 4-7). In order to compensate for the metadevice's asymmetry, the detected pulse peak power of both pulses was matched by adjusting the variable optical attenuators in the interferometer arms. Then the pulses were overlapped in time. Depending on the mutual phase of the two input pulses, the 1 ps pulse may either suppress or increase the metasurface absorption in the region of temporal pulse overlap. Thus, in the case of coherent transparency I measured a bright 1 ps power burst at the centre of the broadened pulse (middle row), while I measured a 1 ps trough in the signal in the case of coherent absorption (bottom row). Such rapid dips in power on a bright background are known as "dark pulses". I note that EDFA amplification provides more gain to lower average power signals [i.e. the measurements in the middle (bottom) row of Figure 4-7 are less (more) amplified than the reference measurements in the top row]. A comparison of the bright burst power (dark pulse power) with the power of the broader pulse, that is visible just before and after the bright burst (dark pulse), reveals a typical power change of 3× to 4× due to the presence of the second pulse. This indicates that the modulation contrast between bright bursts and dark pulses is about 10 dB in this experiment that compensates for the metadevice asymmetry. Although, I note that this proof-of-principle demonstration can be further improved since it is low compared to other dark pulse demonstrations (~30 dB) [86].

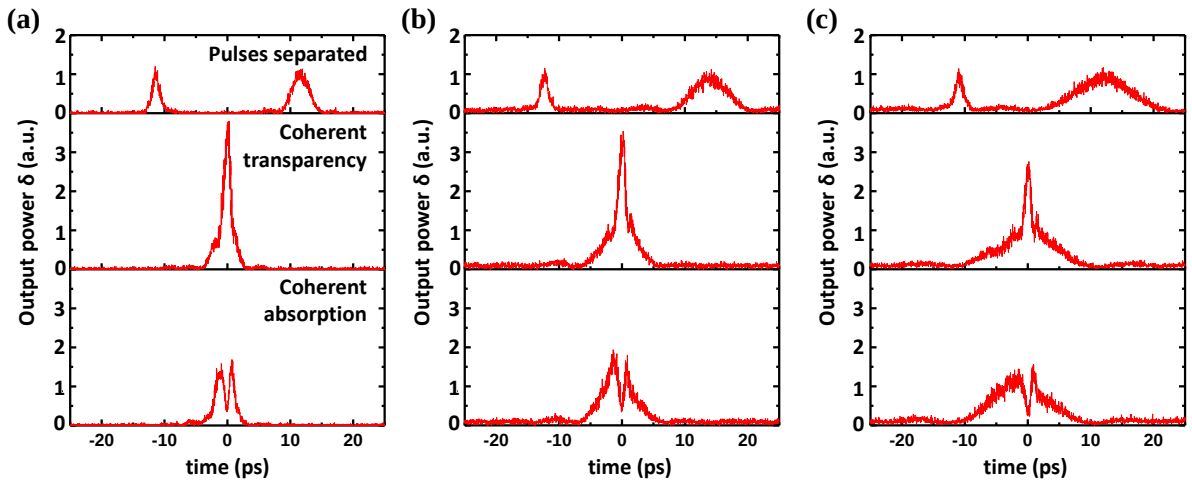

Figure 4-7 **Generation of 1 ps dark pulses.** Output power in channel δ in the cases when the input pulses in channels α and β are separated in time (top); the pulses overlap in the coherent transparency regime (middle); the pulses overlap in the coherent absorption regime (bottom). The columns correspond to different durations of the input pulses in channel β of **(a)** 3 ps, **(b)** 6 ps and **(c)** 9 ps. In all cases, the duration of the pulses in channel α was 1 ps.

My results show that a fibre-optic network containing a plasmonic metasurface absorber of nanoscale thickness allows controlled absorption and transmission of coherent optical signals with 1 ps time resolution, corresponding to a modulation bandwidth of 1 Tbit/s (in the telecommunications C-band). I have previously shown that coherent absorption and coherent transparency enable logic NOT, XOR and AND functions at up to 40 Gbit/s [50] (see Chapter 3). While we are not able to generate faster data signals, our results indicate that our fibre-optic interferometer with its metamaterial absorber could perform these functions at data rates as high as 1 Tbit/s. We expect that the fiberized system may have a modulation bandwidth of a few Tbit/s, which is limited by pulse broadening due to dispersion in the optical fibres rather than coherent absorption that occurs on a timescale of tens of femtoseconds [36]. Dispersion in the interferometer may be described by the average dispersion and differences of dispersion between the interferometer arms. The average dispersion changes the overall pulse width, could be exploited for compression of pre-chirped pulses and does not affect the achievable modulation contrast. Significant dispersion differences across the spectral pulse width would degrade the modulation contrast as different spectral components would interfere with different phase differences on the metasurface. However, such dispersion differences may be avoided by carefully managing the dispersion introduced by the components included in the two arms of the interferometer.

By allowing bright pulses to trigger coherent absorption of a carrier signal, our fibre-optic network with metamaterial absorber can be used to convert an arbitrary sequence of bright pulses into dark pulses. Such an arbitrary dark pulse pattern generator without minimum intensity requirements could find uses in signal processing, dark soliton generation, nonlinear optics [95] and spectroscopy [96].

4.5 Conclusions

To conclude, in this chapter I presented all-optical control of ps pulses with 1 THz bandwidth in a fibre-optic information network containing a fibre encapsulated metasurface absorber. Interaction of mutually coherent optical pulses on a lossy metasurface enables

controlled transmission and absorption of 1 ps optical signals, pulse shaping and 1 ps dark pulse generation. Interestingly, such pulse shaping is not dependent on pulses repetition rate and duration and thus may be used for conversion of an arbitrary sequence of bright pulses intro dark pulses.

The underlying mechanism of coherent perfect absorption and coherent perfect transmission is a truly-linear physical phenomenon, thus pulse shaping as well as more sophisticated data processing demonstrations such as logic functions [50] may be possible at any level of intensity down to the quantum regime [35]. Potential applications beyond dark pulse generation range from fast and energy-efficient all-optical information processing (Chapter 3) to coherent quantum information networks and dark pulse generation (Chapter 4).

Chapter 5 Cryptography in coherent optical information networks using dissipative metamaterial gates

Part of the work in this chapter has been published as: **Cryptography in coherent optical information networks using dissipative metamaterial gates.** A. Xomalis, I. Demirtzioglou, Y. Jung, E. Plum, C. Lacava, P. Petropoulos, D. J. Richardson, and N. I. Zheludev. *APL Photonics* **4**, 046102 (2019) [72] selected as APL Photonics editor's pick. The fabrication of metasurfaces on optical fibre tips and optical characterisation of the metadevices were done by myself, however, I acknowledge help of Dr. Y. Jung with encapsulation of fibre metamaterials and assistance of I. Demirtzioglou with experimental equipment. Moreover, I thank Dr. E. Plum for advice and help with optical encryption measurements. Other co-authors contributed with advice and/or to supervision and writing of the article.

5.1 Introduction

All-optical encryption of information in fibre telecommunication networks offers lower complexity and far higher data rates than electronic encryption can deliver. However, existing optical layer encryption methods, that are compatible with keys of unlimited length, are based on nonlinear processes that require intense optical fields. Here, I introduce an optical layer secure communication protocol that does not rely on nonlinear optical processes but instead uses energy redistribution of coherent optical waves interacting on a plasmonic metamaterial absorber. I implemented the protocol in a telecommunication optical fibre information network, where signal and key distribution lines use a common coherent

information carrier. I investigated and demonstrated different encryption modes, including a scheme providing perfect secrecy. All-optical cryptography as demonstrated in this chapter exploits signal processing mechanisms that can satisfy optical telecom data rate requirements in any current or next-generation frequency band with bandwidth exceeding 100 THz [36] and switching energy of a few photons per bit [35]. Arguably, the findings presented in this chapter are the first demonstration of the use of plasmonic/metamaterial devices in a data security application.

5.2 Encryption protocols: one-time pad cipher

Secure exchange of confidential information is essential in banking, health care, social media, the Internet of Things, government, the security forces and many other aspects of modern life. Fully secure cryptography has been known since 1882, when F. Miller introduced the one-time pad technique [97], which uses a perfectly random key that is at least as long as the message. During World War I, G. S. Vernam re-invented and patented [98, 99] the technique, which was proven to be unbreakable by C. E. Shannon in 1949 [100, 101]. One-time pad ciphers have been used for top-secret diplomatic and military communications ever since.

Table 5-1 **Random key.** The random sequence of numbers generated by throwing a 26-sided dice 26 times. We chose 26 times in order to fit the letters of the alphabet. In principle, the key should be as long as possible to survive brute force attacks.

Random generated Key.										
5(E)	**13(M)**	**2(B)**	**6(F)**	**19(S)**	**4(D)**	**22(V)**	**3(C)**	**3(C)**	**18(R)**	**10(J)**
11(K)	**25(Y)**	**16(P)**	**9(I)**	**26(Z)**	**3(C)**	**7(G)**	**7(G)**	**21(U)**	**5(E)**	**17(Q)**

Let us assume that we have a random number generator, in our case 26-sided dice and roll it 26 times. The resulting random numbers can be considered as the key for the message, see Table 5-1. The key should be at least as long as the message to avoid any repetition. For better secrecy, the key can be pre-shared between sender (Alice) and receiver (Bob).

In this example, Alice wishes to send "GOODMORNING" to Bob, where the letters correspond to specific numbers, for example G=7, O=15 etc. Then, Alice can use random numbers of the key for encryption. The sender needs to inform the receiver for the exact point that they should look at when decrypting the message. For example, common passwords between sender and receiver where of this nature: "May the 5th" meaning that the receiver should start reading the key from the 5th line of the 5th page in order to decode the secret message correctly. Here, I will start using the key from the beginning for clarity. Table 5-2 shows the methodology that Alice will follow for encoding her message. First, she adds the numbers of the message and key and then if the number is greater than 26 (modulo 26) she subtracts 26 and otherwise she leaves it as it is. Alice uses two encryption stages here, later will discuss more sophisticated ways for data encryption. The resulting cipher text alone does not contain any information about the initial message. An eavesdropper will not be able to decode the secret text without knowledge of the secret key as well as the point that Alice chose to start using the key (in this case she started from the first letter).

Table 5-2 **Encoding process.** Alice adds letters of key and message and then applies modulo 26 in order to encrypt her message with respect to the given key.

Message encoding											
Message	G	O	O	D	M	O	R	N	I	N	G
Message	7	15	15	4	13	15	18	14	9	14	7
Key	5(E)	13(M)	2(B)	6(F)	19(S)	4(D)	22(V)	3(C)	3(C)	18(R)	10(J)
Message + Key	12	28	17	10	32	19	40	17	12	32	17
Modulo 26	12	2	17	10	6	19	14	17	12	6	17
Cipher text	L	B	Q	J	G	S	N	Q	L	F	Q

When Bob receives the cipher text, he needs to follow the inverse process in order to decrypt the secret message, see Table 5-3. First, he has the key (pre-shared key) and

assuming that he knows the starting point (Alice let him know) he takes the difference between cipher text and key and adds 26 to any non-positive numbers.

Table 5-3 **Decoding process.** Bob applies the inverse function of encryption for the decryption of the cipher text. First, Bob aligns the key and message and takes the difference, then he applies modulo 26 to decrypt the secret text.

Cipher text decoding											
Cipher text	L	B	Q	J	G	S	N	Q	L	F	Q
Cipher text	12	2	17	10	6	19	14	17	12	6	17
Key	5(E)	13(M)	2(B)	6(F)	19(S)	4(D)	22(V)	3(C)	3(C)	18(R)	10(J)
Cipher text - Key	7	-11	15	4	-13	15	-8	14	9	-12	7
Modulo 26	7	15	15	4	13	15	18	14	9	14	7
Message	G	O	O	D	M	O	R	N	I	N	G

One-time pad ciphers are used by governments and secret agents for their practicality and simplicity. There are plenty of techniques and operations, except modular addition, for data encoding such as logic functions (but not limited to these) between data and key. XOR (exclusive or/exclusive disjunction) is the logical operation, which is most commonly used by computers for electronic encryption since it is a native machine instruction and for this reason extremely fast and of lower complexity.

More widely-used encryption techniques use keys of limited length, making them vulnerable to brute force attacks. Symmetric techniques, such as Data Encryption Standard (DES) [102] and Advanced Encryption Standard (AES) [103], use the same key for encryption and decryption and therefore require secure key distribution, e.g. quantum key distribution [104-106]. Asymmetric techniques, such as Rivest–Shamir–Adleman (RSA) [107], avoid the key distribution problem by using a public key for encryption and a private key for decryption, but suffer from a higher computational cost. Such encryption is normally implemented electronically, leaving the optical layer used for data transmission vulnerable to attacks. Optical layer security can be improved by all-optical encryption. However, all-optical encryption techniques that can use one-time pad ciphers in conventional networks rely on nonlinear optics [108, 109], implying high intensity and energy requirements. Moreover, the use of finite keys in all-optical encryption and related approaches to optical layer security, e.g. optical steganography [110] and code-division multiple access systems

[111-113], cannot be fully secure. Thus, efficient exchange of confidential information with perfect secrecy remains a challenge. Coherent communication, which uses the phase of optical signals, has gained attention in recent years for its potential for improving communication line capacity [114-116]. Phase stabilization techniques [117, 118] and emerging networks with mutually coherent information channels [118-120] provide an opportunity to develop secure solutions based on the relative phase of channels using the same wave information carrier. Within this chapter, I use the term "coherent information network" to refer to such networks with mutually coherent information channels.

5.3 Implementation of one-time pad cipher for coherent optical communications

Here I propose and experimentally demonstrate a secure encryption protocol for coherent information networks. The proposed encryption protocol is applicable to any wave information carrier in a network containing mutually coherent communication lines. It is a symmetric, one-time pad technique without significant computational cost and immediate signal recovery. I report on proof-of-principle demonstrations of the encryption and decryption protocol in a coherent telecommunication optical fibre network. The underlying encryption and decryption operations occur in THz bandwidth (see Chapter 4) coherent optical gates that can operate with single photons (see subsection 7.2.3). Therefore, such optical implementations have the potential to provide perfect secrecy with THz bandwidth and low power consumption.

The general concept of a coherent encrypted information network based on any wave information carrier is illustrated in Figure 5-1, considering transmission of secret data by a sender Alice to a receiver Bob in the presence of an eavesdropper Eve along the transmission line. A common coherent carrier is modulated to generate data and key signals. The data is encrypted by forming a coherent superposition of the data and the key in a first coherent gate. The encrypted data and the key are transmitted using separate, mutually coherent

channels. Superposition of the encrypted signal with the key in a second coherent gate results in recovery of the original data.

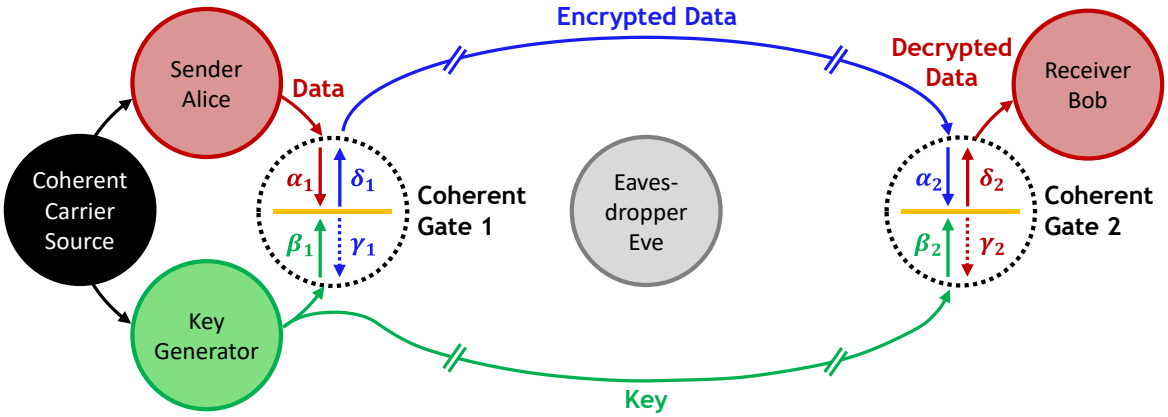

Figure 5-1 **Coherent encrypted information network.** Alice encrypts her data by forming a coherent superposition of data and key on Coherent Gate 1. Bob decrypts the data by combining the encrypted data and the key on Coherent Gate 2. To eavesdrop the communication line Eve would have the difficult task of detecting not only the intensity of the encrypted data and key signals, but also their mutual phase and shall also know the type of gate that has been used for encryption and decryption

My optical implementation of coherent cryptography is based on analogue optical gates exploiting linear interactions of mutually coherent waves on a lossy beam splitter [31]. In recent years it has been demonstrated that a thin, lossy beam splitter illuminated from both sides can act as a four-port device for incident and reflected waves and can operate in different functional modes [56]. XOR, AND (logical conjunction) and NOT (logical negation) all-optical gates have been demonstrated in coherent telecommunication fiber networks [50] (see Chapter 3) reaching a switching bandwidth of 1 THz [76] (see Chapter 4). Here I used such coherent optical gates for encryption and decryption of a binary optical data signal with amplitude modulation. I implemented the technique in a fully-fiberized network at a bitrate of 3 Gbit/s at the telecommunications wavelength of 1550 nm. I experimentally demonstrated partially secure modes of encryption that would require complex techniques for eavesdropping and proposed a more sophisticated implementation that offers perfect secrecy.

The coherent optical gates used for encryption and decryption exploit the fact that linear interactions between waves and matter may be controlled by mutually coherent waves. Counterpropagating, co-polarized and mutually coherent light waves form an optical standing wave with alternating positions of negligible electric field (nodes) and enhanced electric field (anti-nodes). A material that is thin compared to the wavelength of the coherent waves may be placed at such a node or an anti-node, where its interaction with the optical electric field will be negligible or enhanced, respectively. This allows the absorption of light in a thin absorber to be controlled, in principle from 0% (coherent perfect transparency) to 100% (coherent perfect absorption) [48] as discussed in subsection 2.2.3. This control over absorption of light with light without a nonlinear medium occurs on a femtosecond timescale corresponding to more than 100 THz bandwidth [36], for single quanta of light [35] and can be used to perform all-optical signal processing functions in telecommunication frequency bands [50] as demonstrated in the previous chapters. Thus, a thin absorber can act as an ultrafast, low power analogue optical gate. The gate has two inputs – the counterpropagating, mutually coherent incident waves – and two outputs formed by the superposition of transmitted and reflected waves. Here I used such gates for (i) encryption by superposition of mutually coherent data and key signals and (ii) decryption by coherent perfect absorption of the key resulting in recovery of the original data, regardless of what the coherent key was.

Consider two coherent optical gates ($i = 1, 2$), each with counterpropagating input signals, α_i and β_i, and output signals, γ_i and δ_i. The counterpropagating, co-polarized and mutually coherent optical input signals α_i and β_i have electric fields $E_{\alpha i}$ and $E_{\beta i}$ and interact with a linear material of negligible thickness within the gate. Linear transmission and reflection of light can be described by the generally complex Fresnel field transmission and reflection coefficients t and r, where $t = r + 1$ for planar, non-diffractive structures. Thus, the time-dependent output signals γ_i and δ_i with electric fields $E_{\gamma i}$ and $E_{\delta i}$ resulting from simultaneous reflection and transmission of the incident fields are given by:

$$E_{\gamma i} = tE_{\alpha i} + rE_{\beta i} \text{ and } E_{\delta i} = rE_{\alpha i} + tE_{\beta i} .$$

A coherent perfect absorber of negligible thickness is described by $t = 0.5$ and $r = -0.5$ (keeping only the negative sign term assuming a π phase shift in reflection [35]), where the minus sign indicates that reflection occurs with a π phase shift. It transmits and reflects

$|t|^2 = |r|^2 = 25\%$ of a single incident light beam's intensity and absorbs the remaining 50%. It follows that the output fields from a coherent perfect absorber will always have the same intensity and a π phase difference, $E_{\delta i} = -E_{\gamma i}$. In particular, for incident fields of the same intensity, constructive interference on the absorber ($E_{\alpha i} = E_{\beta i}$) results in coherent perfect absorption ($E_{\delta i} = E_{\gamma i} = 0$), while destructive interference ($E_{\alpha i} = -E_{\beta i}$) results in coherent perfect transparency ($E_{\gamma i} = E_{\alpha i}$ and $E_{\delta i} = E_{\beta i}$). There are three characteristic cases of encryption for mutually coherent, binary and intensity-modulated data and key signals, α_1 and β_1, interacting on a coherent absorber: (i) If data and key are in phase, coherent absorption of simultaneously-arriving pulses implies that a high output level (logical "1") only occurs if a single pulse is incident, corresponding to an encrypted output α_1 XOR β_1. (ii) If they have a π phase difference, a high output signal due to coherent transparency for simultaneously-arriving pulses corresponds to an encrypted output α_1 AND β_1. (iii) Other phase differences between data and key lead to partial absorption of simultaneously-arriving pulses. In particular, a $\pi/3$ phase difference yields the same output level for one or two incident pulses (e.g. $|E_{\gamma 1}| = |E_{\delta 1}| = 0.5|E_{\alpha 1}|$ for $|E_{\alpha 1}| \neq 0$, $E_{\beta 1} \in \{0, E_{\alpha 1} e^{\pm i\pi/3}\}$), corresponding to an encrypted output α_1 OR β_1. In all cases, the original data may be recovered (with some attenuation) by combining the encrypted signal

$$E_{\alpha 2} = E_{\delta 1} = E_{\beta 1}/2 - E_{\alpha 1}/2 \,.$$

with the key $E_{\beta 2} = E_{\beta 1}/2$ on a second coherent absorber, where the key is removed by coherent absorption, resulting in an output

$$E_{\delta 2} = E_{\alpha 1}/4.$$

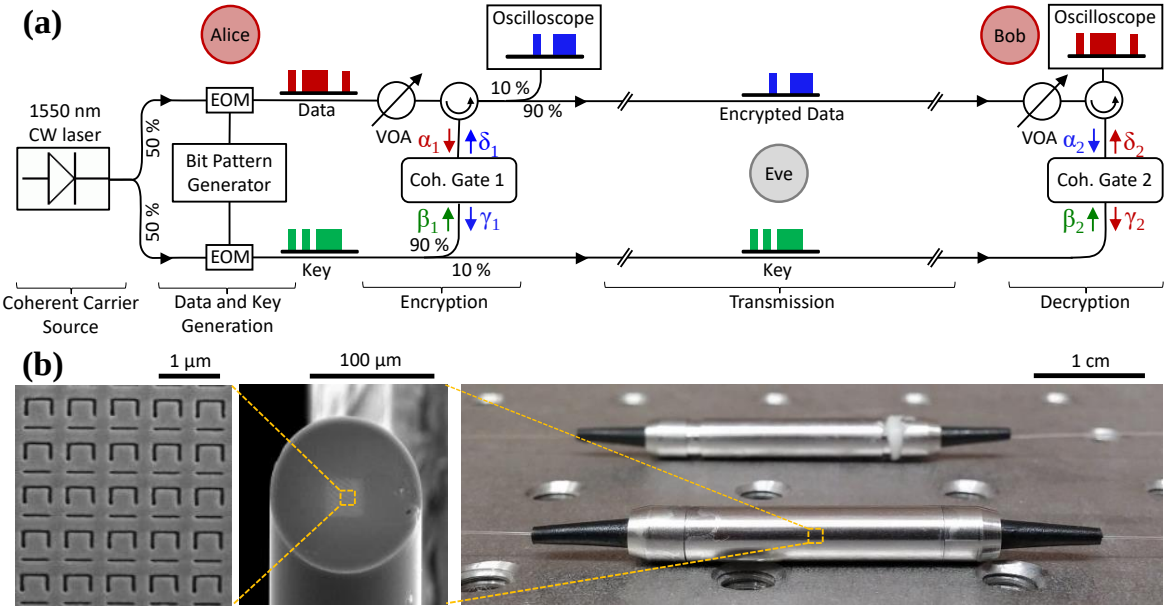

Figure 5-2 **Optical implementation of a coherent encrypted information network. (a)** A CW diode laser operating in the telecommunications C-band was used as coherent carrier source. Other elements in the schematic are abbreviated as follows: EOM – intensity electro-optic modulator, VOA – variable optical attenuator. **(b)** The coherent optical gates are based on interaction of four waves on a plasmonic metamaterial absorber. The metamaterial absorber is manufactured in a 70-nm-thick gold film on the core of a single-mode polarization-maintaining optical fibre (SEM images) and packaged in a standard fiber device housing (photograph).

In this chapter, I focus on the characteristic cases of XOR, AND and OR encryption and decryption using two coherent optical gates that approximate coherent perfect absorbers. Each gate contains a plasmonic metamaterial absorber fabricated on the core of an optical fibre (Figure 5-2(b)) within a stainless steel enclosure with standard pigtailed FC/APC connectors ensuring compatibility with standard fibre components. The metamaterial was fabricated as described in section 2.3. At the experimental wavelength of 1550 nm, a single input signal entering the first coherent optical gate in channel α_1 (β_1) experiences about 15% (15%) transmission, 22% (20%) reflection and 63% (65%) losses including coupling losses. Corresponding values for the second coherent optical gate are 14% (14%) transmission, 26% (20%) reflection and 60% (66%) absorption.

I characterized the encryption and decryption functionalities of the coherent optical gates in a fibre network consisting of two polarization-maintaining fibre interferometers (Figure 7-5 (a)). The output of a 1550 nm wavelength Continuous Wave (CW) laser (ID

Photonics CoBrite-DX4) was split along two interferometer arms with electro-optic intensity modulators (EOSPACE AX-0K5-10-PFA-PFA-UL and FUJITSU FTM7937-AA) that were controlled by an arbitrary waveform generator (Tektronix AWG7122C) to produce data and key bit patterns, α_1 and β_1. These were combined on the first gate to generate the encrypted data signal. Using a circulator and a splitter, the encrypted data δ_1 and the key were transmitted separately from the encryption setup (Alice) to the decryption setup (Bob), where they were combined on the second gate for decryption. A delay line was used to ensure temporal overlap of the encrypted data with the relevant part of the key on the second gate. The delay line was combined with a polarization controller and polarization beam splitter that were used to align the polarization state of the key to that of the encrypted data. A splitter, a circulator and two Erbium-doped fibre amplifiers (KEOPSYS) were used to monitor the encrypted and decrypted signals, δ_1 and δ_2, simultaneously with the aid of an oscilloscope (Agilent Infiniium DCA-J 86100C). Variable optical attenuators were used to prevent optical damage of the metamaterials within the coherent optical gates and to balance the peak power of the optical signals. In all experiments, the incident electric field was oriented parallel to the symmetry axis of the metamaterial. While my fibre interferometers are stable on sub-second timescales, which is sufficient for proof-of-principle demonstrations, I note that practical applications would require active stabilisation of the optical path lengths to prevent phase drift in the interferometer, as well as a fully polarization-maintaining fibre network.

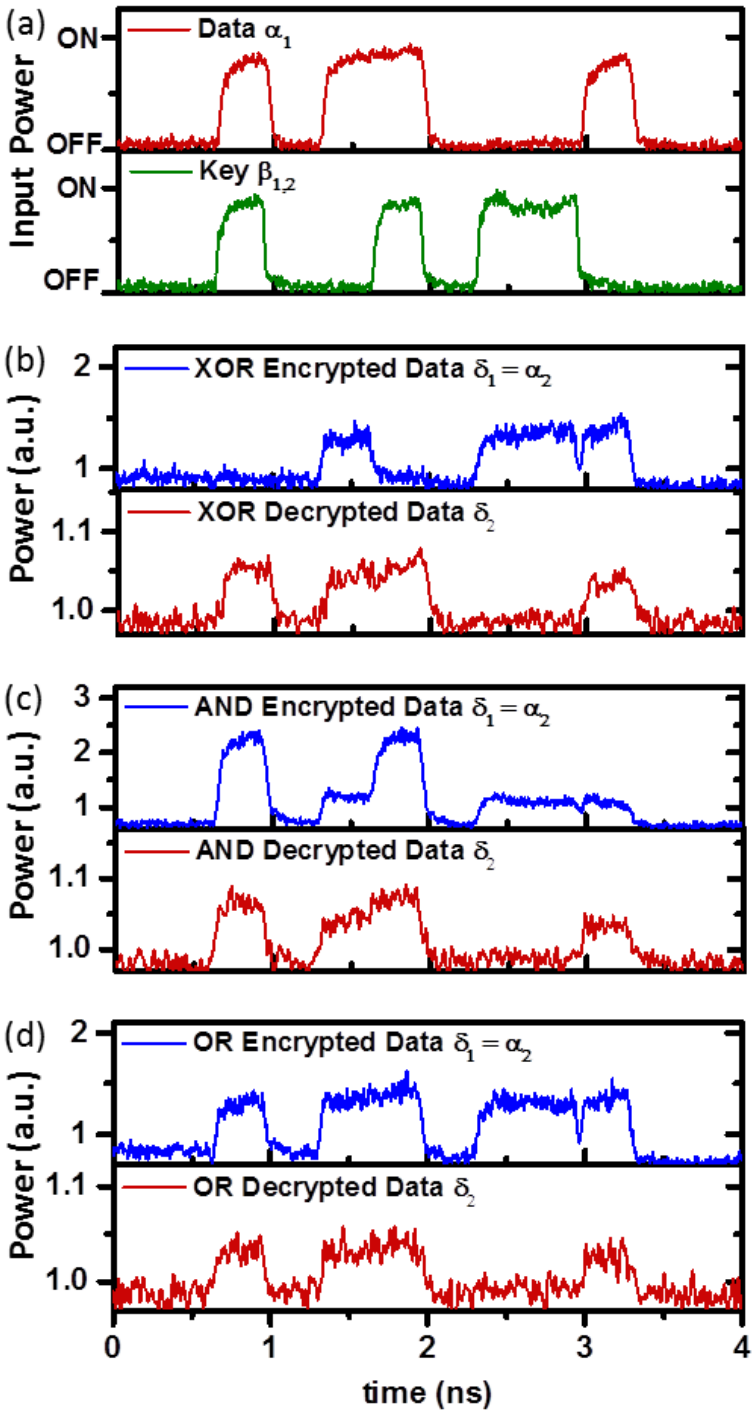

Figure 5-3 **Encryption and decryption in the coherent information network at 3 Gbit/s using different types of optical gates.** **(a)** The encryption-decryption performance is illustrated for optical signal and key sequences presented in (a). Encrypted and decrypted sequences for coherent optical gates operating in the following encryption modes: **(b)** XOR; **(c)** AND; **(d)** OR.

Encryption and decryption were studied with binary, intensity-modulated bit patterns, where high and low intensity correspond to logical "1" and "0", respectively. While the one-time pad approach is applicable to bit patterns of any length, I demonstrated the principle with patterns of 8 bits for experimental simplicity and clarity. The data pattern in channel α_1 is 10110001 and the key pattern in channel β_1 is 10010110 at a bitrate of 3 Gbit/s throughout all experiments (Figure 5-3(a)). Depending on the optical phase difference between data and key, the output δ_1 of the first coherent optical gate corresponds to (data) XOR (key), (data) AND (key) or (data) OR (key). In the case of XOR encryption (Figure 5-3(b)), where data and key input states of 1 and 1 are eliminated by coherent absorption, eavesdropper Eve cannot derive information about the secret message from the intensity of either the encrypted signal or the key alone: Both intensity levels in key and encrypted signal may correspond to either 1 or 0 in the data. In the case of AND encryption (Figure 5-3(c)), where data and key input states of 1 and 1 are transmitted by coherent transparency, Eve can determine 50% of the data bits from the intensity of the encrypted signal, which contains 3 levels. By identifying the highest and lowest intensity levels as 1 and 0, respectively, Eve can read 10x10xxx. In the case of OR encryption (Figure 5-3(d)), where any data and key input pulses are encrypted with the same intensity, Eve can read 25% of the data bits from the encrypted signal intensity. By identifying the low intensity level as 0, Eve can read x0xx0xxx and she can further assume that 2/3 of the remaining bits are likely to be 1 (assuming an equal loading between 0 and 1 bits). In all cases, Bob successfully decrypts the secret message.

Thus, if Eve can only detect intensity, then coherent XOR encryption is secure and AND and OR encryption are partially secure as summarized in Table 5-4. However, I examined next the case where Eve can also detect phase. Figure 5-4 illustrates the data, key, encrypted and decrypted states in terms of intensity and phase, where the security of the encryption scheme depends on whether information about the secret data can be derived from the encrypted signal without knowledge of the key (which is independent of the data and therefore cannot contain information about the data). It turns out that the high intensity states for XOR and OR encryption have different phases, allowing their decryption by phase-detection. This allows Eve to read 50%, 50% and 100% of the encrypted data in case of XOR, AND and OR encryption without knowledge of the key (Table 5-4).

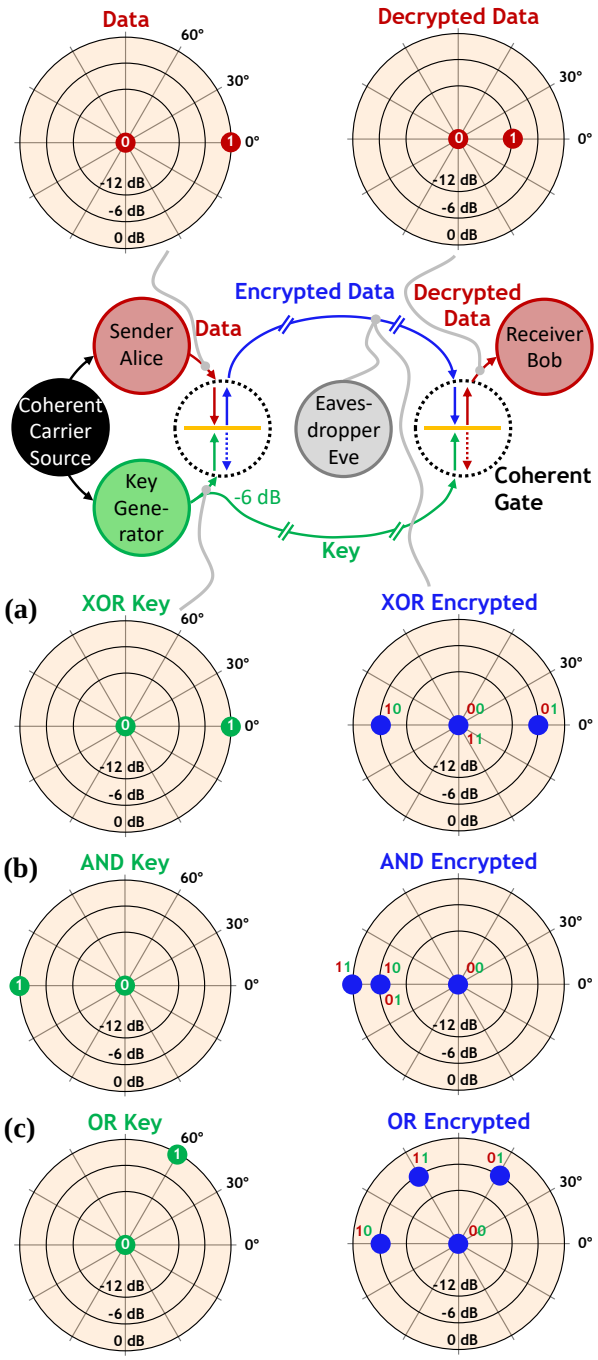

Figure 5-4 **Security of coherent encryption with different all-optical gates.** Polar diagrams showing power and phase (as radius and angle) of data, key, encrypted and decrypted states for the characteristic encryption modes of **(a)** XOR, **(b)** AND and **(c)** OR using four-port coherent optical gates based on a thin film absorber. The binary logical states are denoted by "0" and "1". Assume eavesdropper Eve attempts to recover the data (red) by detecting the encrypted signal (blue). XOR encrypted data cannot be decrypted by detecting power alone and only partial decryption is possible with simultaneous power and phase detection. AND encrypted data can only be partially decrypted by power detection and phase detection does not provide any additional information. Full decryption of OR encrypted data is possible only by simultaneous detection of power and phase.

Table 5-4 **Security of coherent encryption modes.** Amount of information that can be deciphered by an eavesdropper detecting the encrypted data signal. *Assuming a data signal with an equal number of logical "0" and "1" states.

Coherent encryption mode	Information that can be deciphered from encrypted data	
	Intensity detection	**Intensity and phase detection**
XOR	**0 %**	**50 %**
AND	**50 %**	**50 %**
OR	**25 %***	**100 %**
Secrecy layer	**0 %**	**0 %**

5.4 Perfect secrecy scheme

However, I argue that the coherent encryption scheme may be adapted to become completely secure. To achieve this, the original coherent information network (Figure 5-1) is modified by replacing the key generator with a "secrecy layer" (Figure 5-5) that modulates the data channel in addition to generating the optical key. Alice starts with the same intensity-modulated data as before (states 0 and 1) and a CW signal from the same laser that has a phase difference of $\pi/3$ relative to the data. For randomly chosen data bits, the secrecy layer simultaneously applies a π phase shift to the data and a $\pi/3$ phase shift to the CW laser signal, generating phase-shifted data and optical key, respectively. These are then used for encryption on Alice's coherent optical gate. Thus, the states 1 and 0 are encrypted using the key state K, while the phase-shifted data states 1' and 0' are encrypted with the phase-shifted key state K'. Now the encryption operation on the first coherent optical gate will map all possible combinations of phase-shifted data and key to only two encrypted states, each of which can correspond to either 1 or 0 with equal probability. Eve cannot derive any

information about the original data from knowledge of intensity and phase of either key or encrypted data alone (perfect secrecy, Table 5-4). In other words, encryption may translate the data into any bit sequence of the same length and all are equally likely. Nevertheless, Bob still recovers the original message by detecting only intensity after coherent absorption of the key in his coherent optical gate.

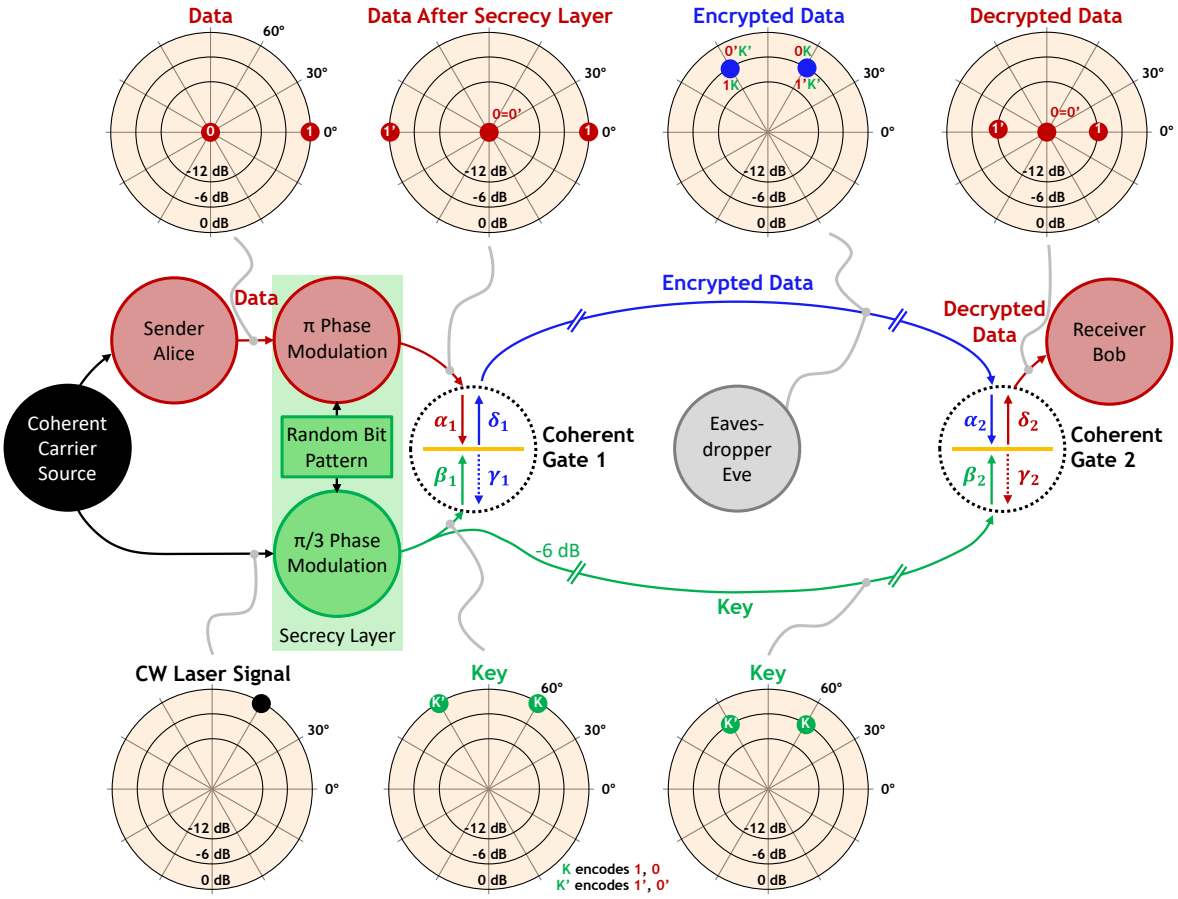

Figure 5-5 **Secure coherent encryption and decryption with secrecy layer.** A secure encryption scheme, where neither the transmitted key nor the transmitted encrypted data alone reveals any information about the secret data. The binary logical states are represented by 0 and 1 and the key is represented by K, where ' represents a phase shift that is applied simultaneously to data and key for randomly chosen bits.

I note that it does not matter that the decrypted data still contains the phase shift that was applied to random data bits as intensity detection does not distinguish between bits

without and with phase-shift (e.g. 1 and 1'). Perfect secrecy requires that the key is truly random, never reused and at least as large as the data bit sequence. If this is satisfied, then Eve could only decrypt the data by simultaneously reading encrypted data and key including their mutual phase. This would be a complex task as these are sent along different fibres in our implementation. (As in other one-time pad encryption systems, this vulnerability could be avoided by using pre-shared keys: Bob could apply a pre-shared key bit sequence to an unmodulated CW laser signal sent by Alice.) Suitable, truly random key bit sequences can be generated at up to 300 Gbit/s based on the output of chaotic semiconductor lasers [121]. Recent measurements of coherent absorption indicate that encryption and decryption on metamaterial-based coherent optical gates can support bitrates of at least 1 Tbit/s in fibre-optic systems [76] (limited by fibre dispersion, see Chapter 4) and 100 Tbit/s in free-space implementations [36].

5.5 Challenges of one-time pad cryptography

When Shannon proved that one-time pad ciphers are unconditionally secure [100, 101], he made several assumptions that are not always true in real-life applications. As the name of the approach states, the one-time pad values and sequences should be used only once. Thus, such cryptographic approaches often require updating of keys. Consequently, use of pre-shared keys is not ideal for transmission of big data due to the limitation of the key's length. As discussed above, the key should be at least as long as the message to avoid repetition and in the case of multiple or back-to-back transmission of secret messages the cipher can become impractical. In addition, concerns raise from the fact that Shannon's proof is dealing with a truly random key. However, commonly used algorithms are pseudorandom bit generators because the generated sequences are strongly depended on an initial imported value. The generation of truly random keys is of great interest for cryptographic schemes and secure telecommunications. For such applications, we cannot use macroscopic processes like coin flipping or dice rolling, we can use microscopic phenomena instead. Recently, great effort has been devoted to the exploration of such processes, which would be able to generate

truly random data/bits. Such microscopic phenomena that can generate unpredictable sequences of bits can be thermal noise, quantum effects, which are of limited bandwidth though, and chaotic semiconductor lasers [121]. The latter is an optical random bit generator which is able to generate truly random bits at rates up to 300Gbit/s for reliable cryptographic applications.

5.6 Conclusions

In this chapter, I have presented the basic principles of one-time pad ciphers and their implementation within a coherent information network. More specifically, I have shown how the phase of mutually coherent information carriers can be exploited for cryptography in coherent fibre-optic telecommunications networks. I have demonstrated encryption and decryption of intensity-modulated optical data on fibre-integrated coherent optical gates based on plasmonic metamaterial absorbers. Encryption is based on creating a superposition of mutually coherent data and key signals in a first coherent optical gate and decryption exploits coherent absorption of the key in a second coherent optical gate to recover the original data signal. I have demonstrated three characteristic modes of encryption at a bitrate of 3 Gbit/s, identified their vulnerabilities and proposed a more advanced implementation that provides perfect secrecy (i.e. no information about the data can be derived from either encrypted data or key alone). As the underlying principle of coherent absorption is compatible with single photon signals and few femtosecond pulses, my cryptographic scheme has potential applications in quantum cryptography as well as energy-efficient and high-bandwidth cryptography and all-optical signal processing within coherent networks.

Chapter 6 Nonlinear control of coherent absorption by metasurfaces in fibre-optic networks

The investigation of functions derived from nonlinearities is an active research field in the optical communication community. Nonlinear all-optical signal processing can have applications ranging from signal switching [32] and wavelength conversion [122] to parametric gain [123] and signal generation [124]. Power-dependent phase changes the optical path of light within a nonlinear element, that can be an optical fibre or a waveguide, and since Kerr nonlinearities are ultrafast, they allow ultrafast switching that is only limited by the intrinsic properties of the device such as response/activation time.

Additionally, the information society puts up ever-increasing demands on energy efficiency and speed of information transfer and processing, e.g. for the Internet of Things, artificial intelligence and video on demand. Noise is one of the fundamental physical phenomena together with chromatic dispersion and Kerr nonlinearities that limit the data capacity (C in bits/s) of a fibre telecommunication channel. Suppression of the average noise power within communication networks is essential for classical [125] and quantum [126] fibre-optic implementations according to Shannon-Hartley theorem (equation below) [127, 128]. Over the last decade, considerable effort has been devoted to the generation of bit streams of high bandwidth (B in Hz) for enabling ultrafast data transmission and optical processing [129, 130] although carrier-to-noise power ratio (S/N) is of great importance as well. Consequently, the need for noise suppression devices [131] that can be, preferably, all-optical, fibre-integrated and packaged remains crucial.

$$C = B\,log_2\left(1 + \frac{S}{N}\right)$$

In this chapter, I demonstrate that, in a nonlinear fibre optical network, coherent interaction of light with a plasmonic metamaterial can be used for optical noise suppression, power-limiting, pulse restoration, pulse splitting and signal transfer between carrier wavelengths. As in previous chapters, the functional element, where coherent absorption takes place, is a fibre-integrated metasurface that is fully-compatible with fibre-optic

networks since it is fibre-pigtailed. First, I need to explain basic principles of nonlinear optics (section 6.1) and the importance of fibres to the observation of nonlinear processes (section 6.2). Section 6.3 describes the experimental demonstration of various nonlinear all-optical signal processing functions.

6.1 Introduction to fibre-optic nonlinearities

In this section, I introduced basic quantities and equations that explain how a material behaves under high intensity illumination. Nonlinear optics is a research field that investigates the modification of material properties under the presence of intense light [52]. One can start the discussion of the optical response of materials by considering the simplest case of how the polarization $\tilde{P}(t)$ (or dipole moment/volume) depends on the strength of electric field, $\tilde{E}(t)$ of an intense light beam. Here, the tilde (˜) represents a quantity that changes rapidly in time. In the simplest case of conventional linear optics the $\tilde{P}(t)$ changes proportional to $\tilde{E}(t)$ strength:

$$\tilde{P}(t) = \varepsilon_o \chi^{(1)} \tilde{E}(t),$$

where ε_o is the permittivity of free space and $\chi^{(1)}$ the linear susceptibility. Now, in the case of high intensities the optical response can be described by generalizing the above-mentioned equations as:

$$\tilde{P}(t) = \varepsilon_o[\chi^{(1)}\tilde{E}(t) + \chi^{(2)}\tilde{E}^2(t) + \chi^{(3)}\tilde{E}^3(t) + \cdots] = \tilde{P}^{(1)}(t) + \tilde{P}^{(2)}(t) + \tilde{P}^{(3)}(t) + \cdots,$$

where $\chi^{(2)}$and $\chi^{(3)}$ are second and third nonlinear optical susceptibilities and $\tilde{P}^{(2)}(t)$ and $\tilde{P}^{(3)}(t)$ are the second and third order polarizations, respectively. Briefly, $\chi^{(1)}$ leads to the refractive index and the attenuation factor (associated with fibre losses), $\chi^{(2)}$ accounts for second-harmonic generation and sum-frequency generation (is zero for materials that have inversion symmetry) and $\chi^{(3)}$ is responsible for third-harmonic generation, four-wave mixing and nonlinear refraction effects.

This Thesis mainly investigates phenomena that are connected with the propagation of light through silica fibres. Silica is glass and isotropic and thus $\chi^{(2)}$ contribution must vanish. This statement can be proven as follows [52]. The second order nonlinear polarization is given by:

$$\tilde{P}^{(2)}(t) = \varepsilon_o \chi^{(2)} \tilde{E}^2(t)$$

where $\tilde{E}(t) = \epsilon\cos(\omega t)$ is the applied field. As the sign of $\tilde{E}(t)$ changes, the sign of the induced polarization ($\tilde{P}^{(2)}(t)$) should change as well (if we assume that the medium has inversion symmetry). Thus, the above equation must be replaced by:

$$-\tilde{P}^{(2)}(t) = \varepsilon_o \chi^{(2)} [-\tilde{E}(t)]^2 = \varepsilon_o \chi^{(2)} \tilde{E}^2(t)$$

Thus, $\tilde{P}^{(2)}(t)$ is equal with $-\tilde{P}^{(2)}(t)$ and this occurs only when $\tilde{P}^{(2)}(t)$ vanishes identically. Consequently, this means that $\chi^{(2)} = 0$ for silica fibres.

As discussed above, low order nonlinear effects derived from $\chi^{(3)}$ are responsible for third-harmonic generation, four-wave mixing and nonlinear refraction effects. Although, the effects that generate new frequencies require a lot of effort to achieve phase matching and usually are inefficient in optical fibres. Thus, nonlinearities in optical fibres are usually associated with nonlinear refraction. By the term of nonlinear refraction I refer to a phenomenon where the refractive index of the medium depends on the intensity of the applied field (and its frequency as well) such as:

$$n(\omega, I) = n(\omega) + \Delta n = n(\omega) + n_2 I = n(\omega) + n_2 |E|^2,$$

where $n(\omega)$ is the refractive index and n_2 is the nonlinear refractive index that is related to $\chi^{(3)}$. The physical origin is that the light induces a nonlinear polarization in the medium, which modifies the medium's properties for light propagation and, macroscopically, can be described as modification of the refractive index. A simple expression for n_2 of a waveguide is:

$$n_2 = \frac{\gamma_{NL} \lambda A_{eff}}{2\pi},$$

where γ_{NL} is the nonlinear coefficient of the material measured in (W km)$^{-1}$, λ is the wavelength of light and A_{eff} is the effective mode area that is related to the fibre's core diameter [77].

Thus, the overall refractive index is intensity dependent and thus, light that propagates through the medium experiences an intensity-dependent phase delay. Now, the nonlinear phase (φ_{NL}) is given by:

$$\varphi_{NL} = \gamma_{NL} P_o L_{eff},$$

$$L_{eff} = \frac{\left[1 - e^{(-\alpha L)}\right]}{\alpha},$$

where P_o is the peak power of an optical pulse, L_{eff} is the effective length (a quantity that plays the role of an effective length that is smaller than the physical length of the fibre, L, due to losses), and α the attenuation factor. As aforementioned, intense light induces φ_{NL} due to a nonlinear refractive index change. Nonlinear modulation of the refractive index is the operational principle of nonlinear Mach Zehnder interferometric devices. There are

reports on all-optical modulators based on such interferometric integrated nonlinear waveguides [32]. Briefly, in one path of the interferometer a nonlinear element is installed. As light, of high intensity, passes through the nonlinear material an additional phase retardation is added due to the Kerr effect (nonlinear phase can be also induced by voltage i.e. electro-optic modulators). Thereafter, when light beams from the two interferometer arms recombine they will interfere destructively or constructively resulting in low or high output power, respectively. By altering the intensity of light one can control the phase of the nonlinear arm, and thus, it is possible to control the interference of light with light. While this section was devoted to the basic physics of the nonlinear contribution of the medium to light propagation, the next section will highlight the importance of optical fibres to the observation of nonlinear effects.

6.2 Optical fibres with enhanced nonlinearities

As discussed in the previous section, an intense light field can give rise to nonlinear refraction effects that can be used for all-optical functions i.e. switching. Over the last decades optical fibres became a popular platform for the observation of nonlinear phenomena. Consequently, in this section the advantages of optical fibres over the bulk media are discussed. G. Agrawal in his book [77] describes very nicely why nonlinear effects can be observed in optical fibres at relatively low power levels.

One can define a figure of merit for the efficiency of nonlinear processes as $I_o L_{eff}$, where I_o is the intensity of a light beam and L_{eff} is the effective length of the medium (discussed in the previous section) and describes the length over which high intensity within the medium can be maintained [132]. Now for a bulk medium if light is focused to a spot, I_o is given by:

$$I_o = \frac{P_o}{\pi r^2},$$

where r is the spot radius. Moreover, L_{eff}, for a Gaussian beam, is equal to the Rayleigh length, which determines the length over which the light beam can propagate without diverging significantly. The Rayleigh length (z_r) is given by:

$$z_r = \frac{\pi {w_o}^2}{\lambda},$$

where, w_o is the radius of the focused beam and in our case I assume that is equal to the spot radius. Thus, for a bulk medium the resulting product describing the nonlinear efficiency is:

$$(I_o L_{eff})_{bulk} = \frac{P_o}{\lambda} \ .$$

In the case of an optical fibre the light experiences waveguiding thus the spot size remains the same throughout fibre's length and is strongly dependent on the fibre's core. Now, L_{eff} (as we mentioned in the previous section) depends on the attenuation factor α ($L_{eff} = \left[1 - e^{(-\alpha L)}\right]/\alpha$). Thus, the product for an optical fibre is given by:

$$(I_o L_{eff})_{fibre} = \frac{P_o\left[1 - e^{(-\alpha L)}\right]}{\pi r^2 \alpha} \ .$$

Now I can compare the product of the bulk medium with the fibre one. I assume that $r \sim 4$ μm for a single-mode fibre, the operation wavelength is λ = 1550 nm, the attenuation factor α is 0.79 dB/km and the fibre length is about 500 m (as the fibre that was used in our experiments). Thus, the comparison shows that:

$$\frac{(I_o L_{eff})_{fibre}}{(I_o L_{eff})_{bulk}} = 12.77 * 10^6 \sim 10^7.$$

This means that the enhancement factor of a nonlinear process in-fibre compared to the bulk medium can reach 10^7. The aforementioned makes clear why nonlinear processes can be observed at "relatively low power levels" in optical fibres. Thus, for my experiments I used highly nonlinear fibres of such measurements.

6.3 Perfect coherent nonlinear absorption

Conventional nonlinear absorption causes intensity-dependent dissipation of light, but cannot result in complete absorption or complete transmission. Here I show that nonlinear phase retardation in an optical fiber can be used to control dissipation of coherent waves interacting on a thin absorber from total absorption to perfect transmission. I report proof-of-principle demonstrations that this effect can be used for optical noise suppression, power limiting, pulse restoration, pulse splitting and signal transfer between carrier wavelengths in an optical fiber network. My results indicate that nonlinear control of coherent absorption can imitate and outperform saturable and multi-photon absorption in coherent light applications.

6.3.1 Introduction

Since 1926, when nonlinear optics began to develop with the observation of nonlinear absorption in uranium-doped glass [133], saturable absorption and multi-photon absorption have become the basis of applications from laser physics to signal processing,

microfabrication and imaging. Semiconductors [134], quantum dots [135], carbon nanotubes [136, 137] and doped fibres [138] serve as saturable absorber for mode-locking and Q-switching of lasers. Multi-photon absorption in photoresists, dyes and metamaterials is the basis of direct laser writing [15, 139], imaging through biological tissue [140], optical limiting and all-optical signal processing [141, 142]. However, conventional saturable and multi-photon absorption cannot escape fundamental limitations. Saturable absorption cannot eliminate absorption completely as it is a consequence of absorption-induced depletion of a material's ground state. Similarly, multi-photon absorption causes a gradual intensity reduction that reduces its own efficiency, making the effect self-limiting and preventing complete absorption.

Here I introduce coherent perfect nonlinear absorption, which exploits an intensity-dependent optical phase shift to control the absorption of light waves with strong phase correlation interacting with a thin absorber. This allows control of dissipation within an ideal absorber from perfect transmission to perfect absorption. I demonstrate this nonlinear absorption mechanism in a fibre-based Sagnac loop, where self-phase modulation and cross-phase modulation in a nonlinear optical fibre yield intensity-dependent phase shifts and a 70-nm-thick plasmonic metamaterial fabricated on the core of a cleaved optical fibre acts as the absorber. I observe signal-to-noise contrast enhancement, narrowing and splitting of few-picosecond optical pulses, optical limiting and signal transfer between different carrier wavelengths.

6.3.2 Coherent nonlinear absorption concept

The light-matter interaction of a material of substantially sub-wavelength thickness can be controlled by counterpropagating coherent light waves (α and β). This allows the manifestation of the thin film's linear [31] and nonlinear [60] optical properties to be controlled. Here I consider linear absorption of such a lossy thin film, which can be controlled, in principle, from 0% to 100% (Figure 6-1(a)) [31]. Ideal performance can be

achieved with a "coherent perfect absorber", which exhibits 25% transmission and reflection each and 50% absorption for illumination from only one side. Almost ideal coherent absorbers consisting of metamaterials [31], multi-layer graphene [35], heavily-doped silicon film [143] and other materials have been reported. The limiting cases of low and high absorption are known as coherent transparency (CT) and coherent absorption (CA). Destructive interference of both waves, α and β, on an absorber of negligible thickness results in perfect transparency, since light-matter interaction is prevented by electric field cancellation. Constructive interference of both waves causes enhanced absorption due to the interaction of the absorber with an enhanced electric field.

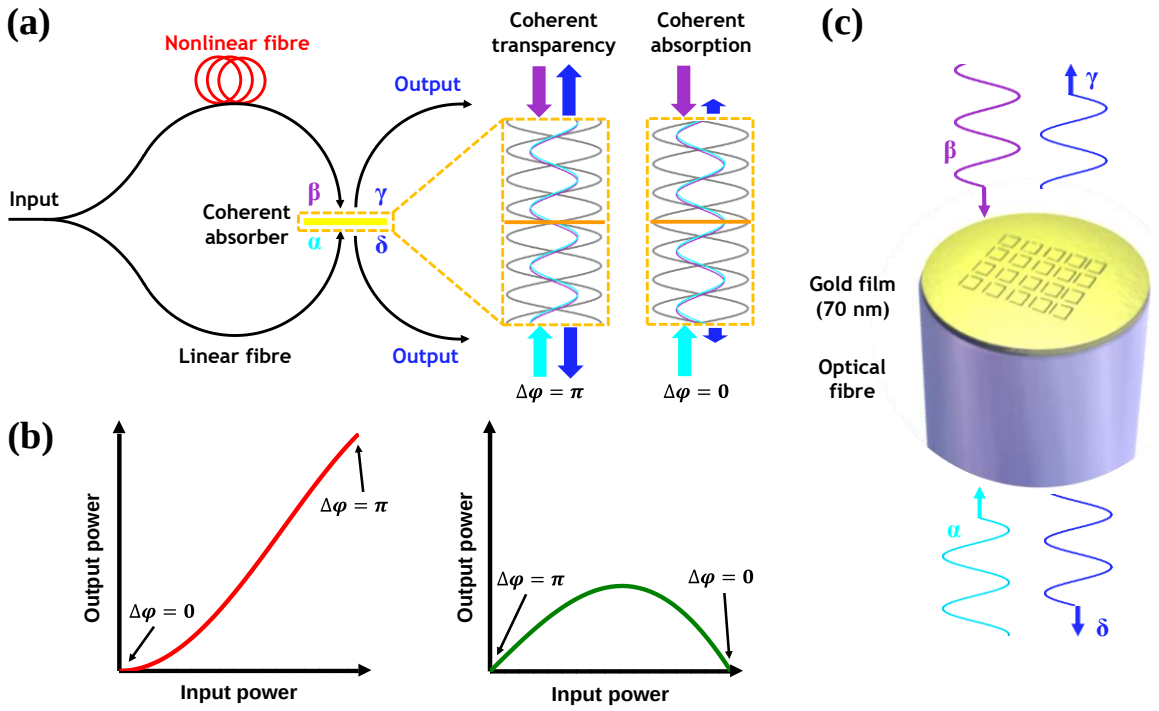

Figure 6-1 **Coherent nonlinear absorption.** **(a)** Counterpropagating and co-polarized light beams with strong phase correlation, α and β, form a standing wave. Propagation of light beam β through a Kerr medium (nonlinear fibre) yields a nonlinear phase shift that displaces the standing wave's nodes and anti-nodes. A thin absorber located at a standing wave node (anti-node) causes weak (strong) light absorption known as coherent transparency (coherent absorption). $\boldsymbol{\Delta\varphi}$ is the power-dependent phase difference of α and β on the absorber. **(b)** Dependence of output power on input power for an ideal absorber. Characteristic cases are shown, where $\boldsymbol{\Delta\varphi}$ changes linearly with input power, from 0 to π and π to 0, respectively. **(c)** The thin absorber used here is a plasmonic metamaterial fabricated on the core of a cleaved single-mode optical fibre. It acts as a four-port optical device with two inputs (α and β) and two outputs (γ and δ).

For illumination of an ideal coherent absorber with mutually coherent input signals of the same intensity, the total output power P_{out} is given by the total input power P_{in} and the phase difference $\Delta\varphi$ between the input signals:

$$P_{out} = P_{in}\, sin^2\left(\frac{\Delta\varphi}{2}\right).$$

Such optical devices with two inputs (α and β) and two outputs (γ and δ) can perform all-optical signal processing functions [50]. As coherent control of absorption of light with light is compatible with single photons [35] and offers THz bandwidth in fibre-optic [76] configurations, it could underpin quantum and energy-efficient, high-bandwidth all-optical signal processing applications.

In this Chapter I will show how coherent transparency and coherent absorption of a thin absorber can be exploited to achieve coherent nonlinear absorption. Nonlinear absorption will occur if the optical power P controls the interference of the input signals on the thin absorber. This will be the case if one of the input signals, e.g. β, experiences a nonlinear phase shift $\varphi(P)$ due to propagation through a medium with a non-linear refractive index, i.e. a Kerr-medium, see Figure 6-1(a). The resulting power-dependent phase difference between α and β on the thin absorber will be:

$$\Delta\varphi = \Delta\varphi_0 + \varphi(P),$$

where $\Delta\varphi_0$ is the phase difference at low power and is determined by the optical length difference of the interferometer arms. With increasing power, the nonlinear phase shift will give rise to a variation between coherent transparency (at $\Delta\varphi = \pm\pi, \pm 3\pi, ...$) and coherent absorption (at $\Delta\varphi = 0, \pm 2\pi, ...$), respectively, corresponding to 0% and 100% absorption for an ideal thin absorber. For a given intensity range, the effect may thus be exploited for preferential absorption of either low intensities (noise suppression) or high intensities (optical limiting) by choosing $\Delta\varphi_0$ and the nonlinearity of the Kerr-medium accordingly (see Figure 6-1(b)).

Here I use a highly nonlinear optical fibre (HNLF) as the Kerr-medium and a nanostructured plasmonic metamaterial as the thin absorber. Using self-phase modulation in the HNLF to control absorption in the metamaterial, I demonstrate optical limiting and contrast enhancement between the intensity of optical pulses and background noise as well as picosecond (ps) pulse restoration/cleaning. Exploiting cross-phase modulation, I demonstrate all-optical transfer of few picosecond pulses from one carrier wavelength to another.

Thus, the next subsection reports on experiments that exploit self-phase modulation arising from Kerr nonlinearity and investigates their potential for noise suppression applications and cleaning of short optical pulses.

6.3.3 Signal-to-noise contrast enhancement, optical limiting and pulse shaping

Here I exploit the nonlinear phase shift introduced by pulses of different intensities propagating through a nonlinear optical fibre to control absorption in a plasmonic metamaterial absorber. The first experiment, based on self-phase modulation, was conducted in an optical fibre network containing a fully fiberized coherent absorber and a HNLF (Figure 6-2).

Macroscopically, self-phase modulation of a light beam can be understood as the phase delay (or nonlinear phase) caused by its own intensity via the Kerr effect arising from the nonlinear polarization (see section 6.1). Since the optical phase changes, this can be described as the change of the refractive index (Δn) of the propagation medium, which is given by:

$$\Delta n = n_2 I,$$

where n_2 is the nonlinear refractive index (see section 6.1) and I is the optical intensity of the light beam.

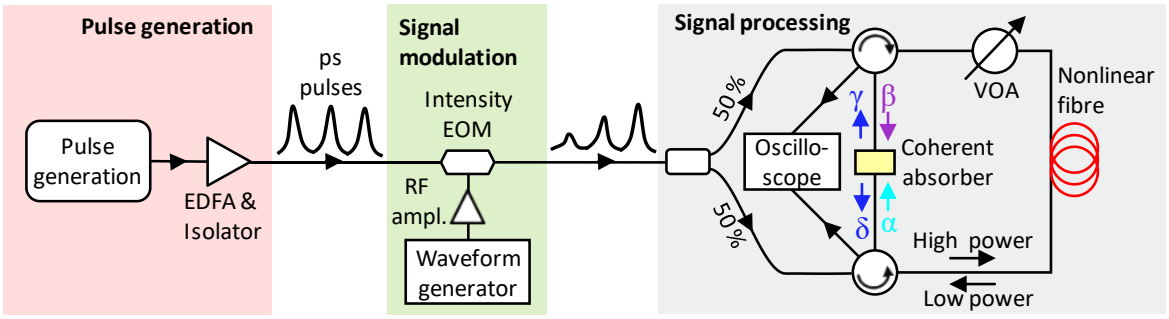

Figure 6-2 **Experimental setup used for signal-to-noise contrast enhancement and optical limiting.** Coherent nonlinear absorption arises from self-phase modulation of 1550 nm wavelength, 1.9 ps pulses interacting on a plasmonic metamaterial coherent absorber. TOF – Tuneable Optical Filter, EDFA – Erbium Doped Fibre Amplifier, EOM – Electro-Optic Modulator, VOA – Variable Optical Attenuator.

All coherent nonlinear absorption experiments were performed in a polarization-maintaining fibre interferometer using linearly polarized laser light with the electric field oriented parallel to the symmetry axis of the metamaterial unit cell. My implementations are similar to a nonlinear optical loop mirror (NOLM) [144], but in contrast to a typical NOLM they combine the signals α and β on a thin absorber (rather than a lossless coupler) that is placed outside the loop, allowing interferometer arms of different length and thus control over $\Delta\varphi_0$. The interferometer is stable on sub-second timescales, which is sufficient for proof-of-principle demonstrations. A gradual phase drift at longer timescales was exploited for switching between different characteristic cases of coherent nonlinear absorption. The laser source is a fibre-coupled tuneable CW laser (ID Photonics CoBrite-DX4) with two independent outputs. The laser output is launched into a frequency comb generator (OptoComb LP-5011) that generates ps pulses at a repetition rate of 10 GHz, which were filtered to adjust the pulse shape and duration. In order to achieve sufficient power levels, I used erbium-doped fibre amplifiers (KEOPSYS) that were protected from back-reflections using optical isolators.

Such nonlinear experiments require a considerable amount of optical power. Here, I choose to use short optical pulses, instead of CW light, that exhibit low average power but also contain enough peak power to give rise to nonlinear effects. A point that requires attention is the duration of the pulses used. In section 4.1, I extensively discussed the fundamental limitations of short pulses propagating within telecommunication networks in terms of fibre dispersion effects. Thus, 1.9 ps optical pulses are used, where peak power is enough to engage fibre nonlinearities and the pulse duration is long enough avoid significant dispersion effects.

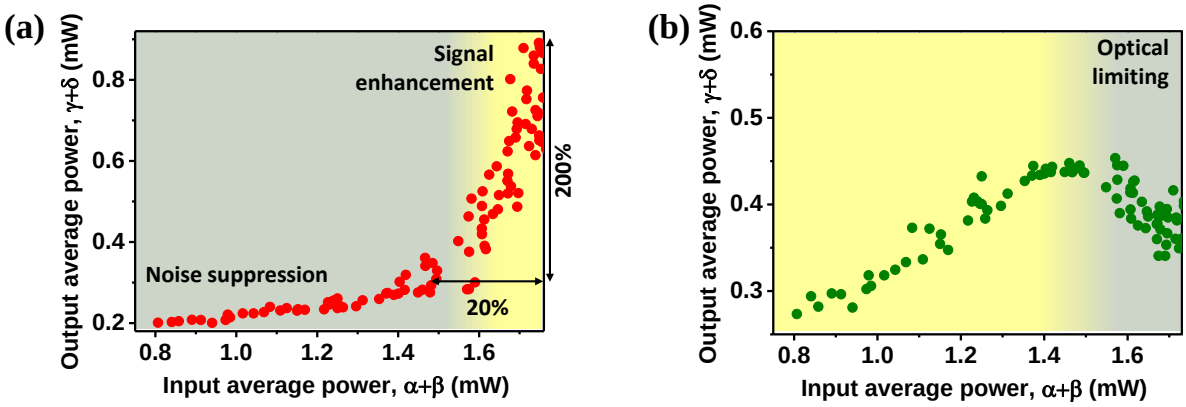

Figure 6-3 **Signal-to-noise contrast enhancement and optical limiting. (a,b)** Measurements of coherent absorber output power as a function of its input power in terms of average power. **(a)** Suppression of low-power input signals by coherent absorption ($\Delta\boldsymbol{\varphi} \approx \mathbf{0}$, grey) transitions towards relative enhancement of high-power input signals by coherent transmission (yellow) as $\Delta\boldsymbol{\varphi}$ approaches $\boldsymbol{\pi}$. **(b)** Coherent transmission ($\Delta\boldsymbol{\varphi} = \boldsymbol{\pi}$) of low power input signals transitions towards coherent absorption of high-power input signals as $\Delta\boldsymbol{\varphi}$ approaches **0** resulting in optical limiting.

The metadevice contains a plasmonic metasurface absorber fabricated on the cleaved end of a single-mode polarization-maintaining optical fibre and packaged as described in sections 2.3 and 3.7. The fibre metamaterial is an array of asymmetric split ring apertures with unit cell dimensions of 700 x 700 μm^2 that was cut into a 70-nm-thick gold film by focused ion beam milling, where the unit cell's symmetry axis is aligned with the slow axis of the fibre. At the operation wavelength of 1550 nm, for input signal entering the channel α(β) the metadevice has 24% transmission, 18% (8%) reflection and 58% (68%) absorption including coupling losses.

For the optical limiting and noise suppression experiments shown in Figure 6-3, the train of 1550 nm wavelength pulses is modulated with an intensity electro-optic modulator (EOSPACE AX-0K5-10-PFA-PFA-UL) controlled by a bit pattern generator (Tektronix AWG7122C) to produce a ramp pulse train envelope with 1 MHz repetition rate in order to probe nonlinear absorption at different pulse peak intensities. Then the signal was split along interferometer arms that introduce different nonlinear phase shifts and recombined on the coherent absorber with an intensity-dependent phase difference. The envelope of the output powers γ and δ were detected simultaneously using Erbium-doped fibre amplifiers (KEOPSYS) with the aid of an oscilloscope (Agilent Infiniium DCA-J 86100C). In order to keep the interferometer stable, the same long HNLF was part of both interferometer arms, where different nonlinear phase shifts resulted from an attenuator (light attenuation to ~3.5%) imposing different intensities of the counterpropagating signals α and β within the HNLF. An optical delay line in one interferometer arm (not shown in the figure) was used to ensure that the pulses arrive simultaneously on the metamaterial absorber. Attenuation of the absorber input signals protects the metamaterial from optical damage. The metadevice input signals are attenuated to the same average power (α = β). A power change of 620 mW within the nonlinear fibre yields a nonlinear phase change of π based on the fibre's specifications. A 620 mW change of the differential peak power of pulses propagating along the nonlinear fibre, causing a nonlinear phase change of π at the pulse peak, corresponds to a change of about 0.7 mW average power (α + β) entering the metadevice in Figure 6-3.

The HNLF (OFS) has 493 m length and an effective nonlinear coefficient γ_{NL}=10.7 (W km)$^{-1}$. We exploited the nonlinear phase shift introduced by laser pulses propagating through the HNLF to control absorption in the plasmonic metamaterial absorber. The nonlinear phase shift φ_{SPM} in the fibre that is experienced by a laser pulse of peak power P_{peak} due to self-phase modulation is:

$$\varphi_{SPM} = \gamma_{NL}\, L_{eff}\, P_{peak}\,,$$

while cross-phase modulation will introduce a phase shift φ_{XPM} (discussed in the next section) on another co-propagating signal of the same polarization and different wavelength of as:

$$\varphi_{XPM} = 2\varphi_{SPM},$$

where $L_{\text{eff}} = (1 - e^{-\alpha L})/a$ is the nonlinear effective length and a = 0.79 dB/km is the propagation loss of the HNLF [77].

There are two limiting cases of coherent nonlinear absorption, which are illustrated in Figure 6-3(a,b) in terms of output power as a function of input power of the coherent absorber metadevice. If the input optical signals α and β constructively interfere at low intensities, resulting in high absorption, the nonlinear phase shift with increasing intensity will reduce absorption, mimicking saturable absorption, Figure 6-3(a). Large absorption of low-power inputs (noise) and weak absorption of high-power input (signals) provides signal-to-noise contrast enhancement. I observe that a 20% change in input average power (between 1.5 and 1.8 mW) yields a 200% change in output average power (between 0.3 and 0.9 mW). On the other hand, if the optical signals destructively interfere at low intensities resulting in low absorption, then the nonlinear phase shift resulting from increased intensity will increase absorption, mimicking multi-photon absorption and providing an optical limiting functionality, Figure 6-3(b). In this case, I observe that the output average power peaks for a 1.45 mW input average power and then falls for a further increase of input power. I note that optical pulses (other than ideal rectangular pulses) contain a range of intensities, that lead to a range of nonlinear phase shifts and therefore different coherent absorption of low-intensity and high-intensity pulse components, which will be explored in detail below. Therefore, optical limiting results in partial absorption of Gaussian pulses, explaining why the detected average power does not (and should not) go to zero in our experiments. In addition, an ideal coherent absorber would be required for complete absorption, e.g. for complete suppression of coherent low-power noise (Figure 6-1(b)). A small background in our measurements is caused by the presence of multiple amplifiers in our setup (Figure 6-3). Nevertheless, the observed relationships of output on input average power resemble those expected for CW signals interacting on an ideal coherent absorber in a nonlinear interferometer (Figure 6-1(b)).

Such preferential absorption of either low or high power may be exploited for optical pulse shaping, such as cleaning/narrowing or splitting of pulses. In order to demonstrate this, I replaced the electro-optic modulator in Figure 6-2 with an additional nonlinear fibre (HNLF

from OFS) of 299 m length with an effective nonlinear coefficient of $\gamma = 10.4$ (W km)$^{-1}$ and spectral filtering as well as amplification were adjusted in order to create distorted pulses. Then I detected the input and output signals of the coherent absorber device with a sampling oscilloscope (EXFO PSO-102). Here, the average power at the metadevice input channel $\alpha = \beta$ is ~ 0.4 mW.

The distorted input pulses have a full width at half maximum of 5.8 ps (Figure 6-4(a-b) left panel). As the low and high power components of these pulses accumulate different nonlinear phase shifts in the HNLF, they may be selectively transmitted or absorbed by the coherent absorber. Suppression of low power by coherent absorption results in pulse narrowing and removal of low-power pulse distortions, while the highest power component of the pulse is transmitted, see right side of Figure 6-4(a). I observed an almost 3-fold pulse width reduction from 5.8 ps to 2.1 ps. In contrast, complete suppression of high power by coherent absorption while lower power is (partially) transmitted splits a single input pulse into a pair of output pulses, see right side of Figure 6-4(b).

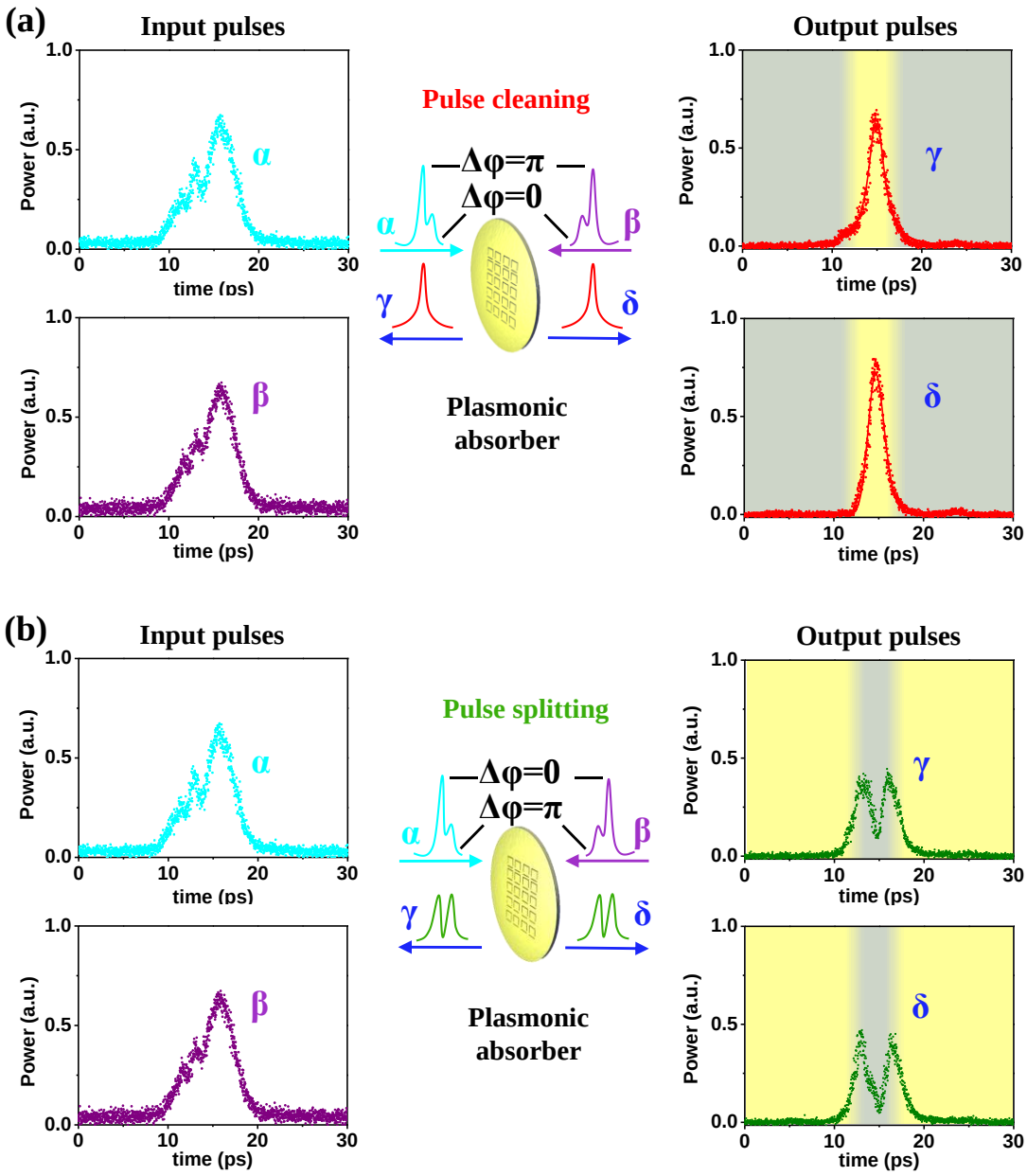

Figure 6-4 **Pulse cleaning and pulse splitting.** **(a)** Left: Distorted input pulses α (top) and β (bottom) at the coherent absorber device. Right: Output pulses γ (top) and δ (bottom) in the cases of coherent absorption (grey) of low power resulting in pulse cleaning. Yellow marks coherent transmission. **(b)** Left: Distorted input pulses α (top) and β (bottom) at the coherent absorber device. Right: Output pulses γ (top) and δ (bottom) in the cases of coherent absorption (grey) of high power, resulting in pulse splitting. The schematics indicate the phase difference $\Delta\varphi$ between the high and low power components of the distorted input pulses after propagation through the HNLF for both cases.

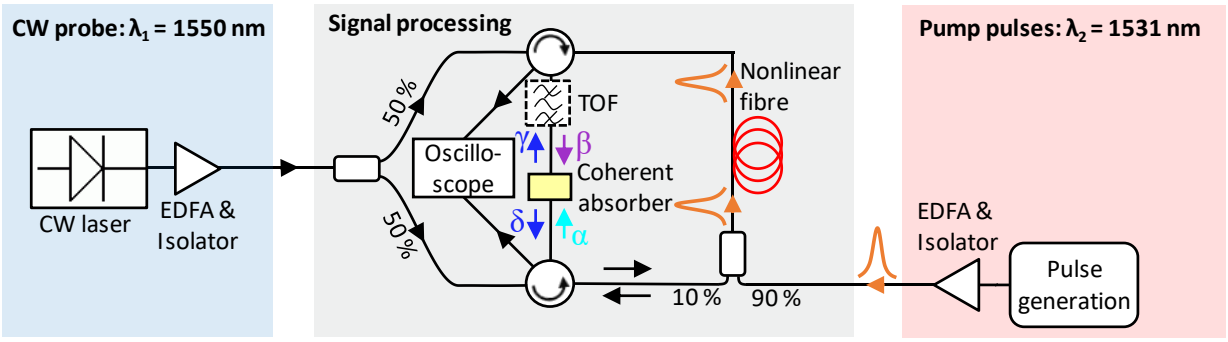

Figure 6-5 **Experimental setup for signal transfer between wavelengths.** Coherent nonlinear absorption of 1550 nm CW light (probe) on a plasmonic metasurface absorber is controlled by cross-phase modulation in a HNLF caused by 1531 nm wavelength laser pulses (pump). EDFA – Erbium Doped Fibre Amplifier, TOF – Tuneable Optical Filter.

6.3.4 Signal transfer between wavelengths

In the second experiment, I investigated all-optical signal transfer between wavelengths via cross-phase modulation. Cross-phase modulation can be understood as a nonlinear process (originating from the Kerr effect) where the optical intensity of one beam influences (or adds) phase to a second light beam that propagates within the same medium. Briefly, the intensity $I^{(2)}$ of the pump beam causes a refractive index change for the probe beam 1 as:

$$\Delta n^{(1)} = 2n_2 I^{(2)},$$

when both beams have the same polarization and overlap within the nonlinear Kerr medium [77].

This allows coherent nonlinear absorption to be used to transfer intensity modulation from one optical wavelength to another as different optical signals co-propagating along the

same HNLF modulate each other's phase by cross-phase modulation, which then controls their absorption within the coherent absorber. In order to demonstrate this, I combined ~10 ps pump laser pulses at 1531 nm wavelength propagating along one interferometer arm with 1550 nm CW probe laser light propagating along both interferometer arms [145], as illustrated by Figure 6-5. The pump pulses are injected before the HNLF and filtered out thereafter. Within the HNLF, presence of a pump pulse causes an instantaneous refractive index change that is proportional to the light intensity (Kerr effect). Therefore, CW light that propagates together with a laser pulse along the nonlinear fibre experiences a phase shift (see subsection 6.3.3). This controls CW light absorption when the interferometer arms, that contain probe light without (α channel) and with (β channel) such phase modulation, recombine on the coherent absorber device. Figure 6-6(a) and Figure 6-6(c) show the coherent absorber outputs, γ and δ, for the characteristic cases, where a nonlinear phase shift of about 45 degrees caused by a pump pulse with about 77 mW peak power decreases (panel (a)) or increases (panel (c)) coherent absorption of probe light. In case of Figure 6-6(a), probe light is coherently absorbed, except when a pump-pulse-induced phase distortion (Figure 6-6(b)) makes the coherent absorber (partially) transparent, resulting in bright output pulses, γ and δ, at the probe wavelength. In case of Figure 6-6(c), probe light is (partially) transmitted, except when a pump-pulse-induced phase distortion (Figure 6-6(d)) triggers coherent absorption, resulting dark output pulses within the bright CW background at the probe wavelength. These observations demonstrate transfer of pulses into bright or dark 10 ps pulses between telecommunications wavelengths with a spectral separation of 19 nm with a bandwidth of at least 100 GHz.

For the cross-phase modulation experiments shown by Figure 6-6, the average probe power at the metasurface absorber device inputs, α and β, was 69 μW and 78 μW, respectively. The pump pulse peak power in the HNLF was 77 mW. The CW probe power entering the HNLF within the two interferometer arms was much lower, 18.5 mW and 1.4 mW for α and β, respectively, where the difference arises from the 90:10 splitter that injects the pump pulses into the loop. See Figure 6-5 for more information.

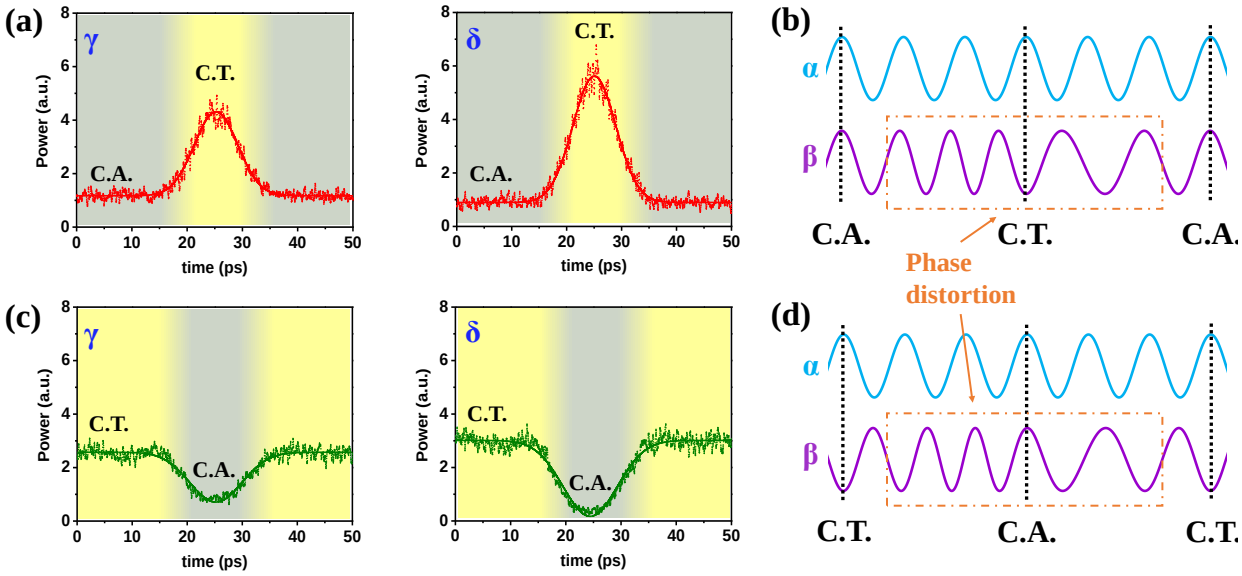

Figure 6-6 **Signal transfer between wavelengths.** **(a)** Time traces of the probe output channels (γ and δ) where the nonlinear phase distortion leads to increased transparency (yellow). **(b)** Schematic explaining how the nonlinear phase affects the interference of the probe input beams α and β in case (a). **(c)** Time traces of the probe output channels where the nonlinear phase distortion leads to increased absorption (grey). **(d)** Schematic explaining how the nonlinear phase affects the interference of the probe input beams α and β in case (c). C.T. – Coherent transmission, C.A. – Coherent absorption.

6.4 Conclusions

To conclude, in this chapter I have presented basic principles of nonlinear optics and highlighted the importance of optical fibres to the observation of nonlinear processes at reasonable intensities. Thereafter, I have introduced the concept of coherent nonlinear absorption, which permits light-intensity-controlled absorption of light from 0 to 100%. The effect results from interaction of counterpropagating mutually coherent light waves on a thin absorber with a nonlinear phase difference. I demonstrate coherent nonlinear absorption in a fibre-based Sagnac loop, where nonlinear phase shifts occur in a nonlinear fibre and absorption occurs in a plasmonic metasurface coherent absorber. I exploit the nonlinearity to perform nonlinear all-optical signal processing functions, including all-optical limiting, 10-fold contrast enhancement of signal to noise, as well as cleaning, narrowing and splitting of 5.8 ps pulses and transfer of optical signals between different telecommunications wavelengths with at least 100 GHz bandwidth. I argue that coherent nonlinear absorption can provide all-optical solutions for optical telecommunications and data processing, where limiting prevents optical damage, noise reduction increases data capacity in classical [125] and quantum [126] channels, signal regeneration enables long transmission lines, and signal transfer between different wavelength division multiplexing (WDM) channels is essential.

Chapter 7 Single photon coherent perfect absorption in a fibre network

My contribution to the work and results discussed in this chapter is the fabrication of fibre-metamaterials, the encapsulation and packaging of such metamaterials resulting in fully-integrated fibre metadevices and the assistance that I provided during the assembly of the fibre-optic setup for single photon experiments when I was a visiting scholar at Nanyang Technological University (NTU) in Singapore in May 2017. All experimental measurements and data analysis reported here were conducted by my colleagues Dr. Anton Vetlugin, Salih Yanikgonul and Dr. Ruixiang Guo at the Centre for Disruptive Photonic Technologies (CDPT) of NTU in Singapore.

7.1 Introduction

In this Thesis the advantages of coherent control of light absorption are highlighted. Since the physics of the underlying phenomenon are truly linear I expect that it can operate extremely fast and at extremely low power. I have shown in Chapter 4 that it is possible to switch ON and OFF light with ps pulses in in-fibre schemes resulting in THz bandwidth [76]. Here we investigate all-optical functionalities of coherent control of absorption down to the quantum regime. We have shown that this concept can be integrated with standard telecommunication optical fibres and, thus, pave the way for energy efficient quantum light processing architectures.

Earlier work [35] has shown that extending the concept of coherent control of absorption to low intensities, signals of few photons, is possible. Moreover, the authors provided evidence that while the absorption from a travelling photon wave is probalistic,

standing wave absorption can be seen deterministically. Their findings have shown that is possible for photons to be coupled into modes of the material (metasurface in our case) such as plasmon resonances in a way that mimicks coherent control experiments with classical light on plasmonic metasurfaces [31, 48, 50, 63].

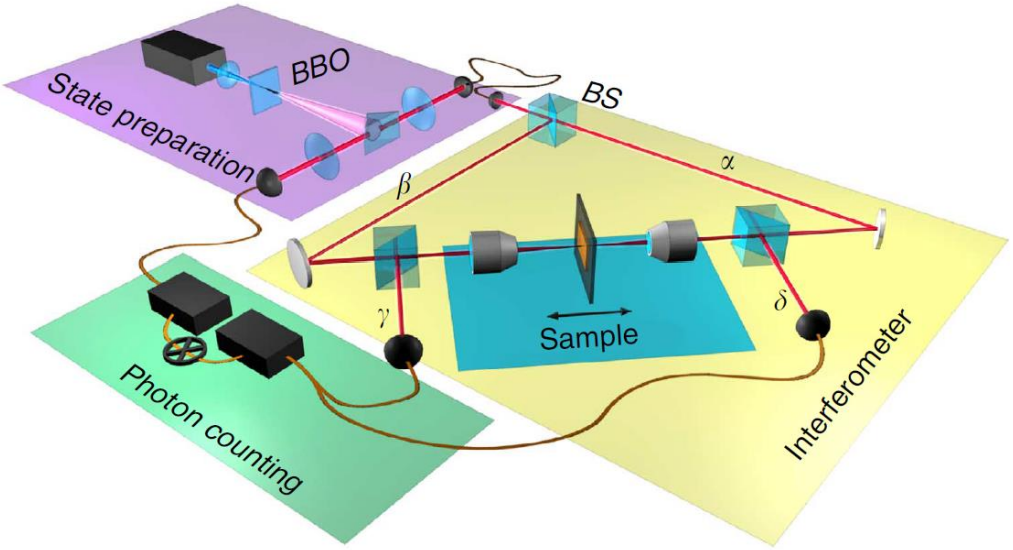

Figure 7-1 **Coherent perfect absorption of single photons in free space.** The plasmonic absorber is placed in the middle point of the free-space interferometer and translated along the optic axis by a piezoelectrically actuated stage. The single photons of the input channels are focused onto the sample by 10x objectives. Photons are then detected in coincidence with the heralding photon at outputs γ and δ [35]. Figure adapted from Ref. [35].

Accordingly, in classical wave optics (as discussed in all previous chapters of this Thesis), a thin film (thin compared to the operation wavelength) experiences no Joule losses if placed at a standing wave node, which is formed by two co-polarized and counterpropagating waves of the same wavelength. On the contrary, if the film is placed at a standing wave anti-node, it will experience strong light-matter interactions since the amplitude of the electric field has its maximum at the anti-node. In the previous chapters, I investigated modulation of light-matter interactions by changing the phase of one input and thus changing the position of the standing wave with respect to the steady metasurface. In this prior work the authors exploited an alternative scheme where the standing wave remains steady and the position of the plasmonic absorber changes [35].

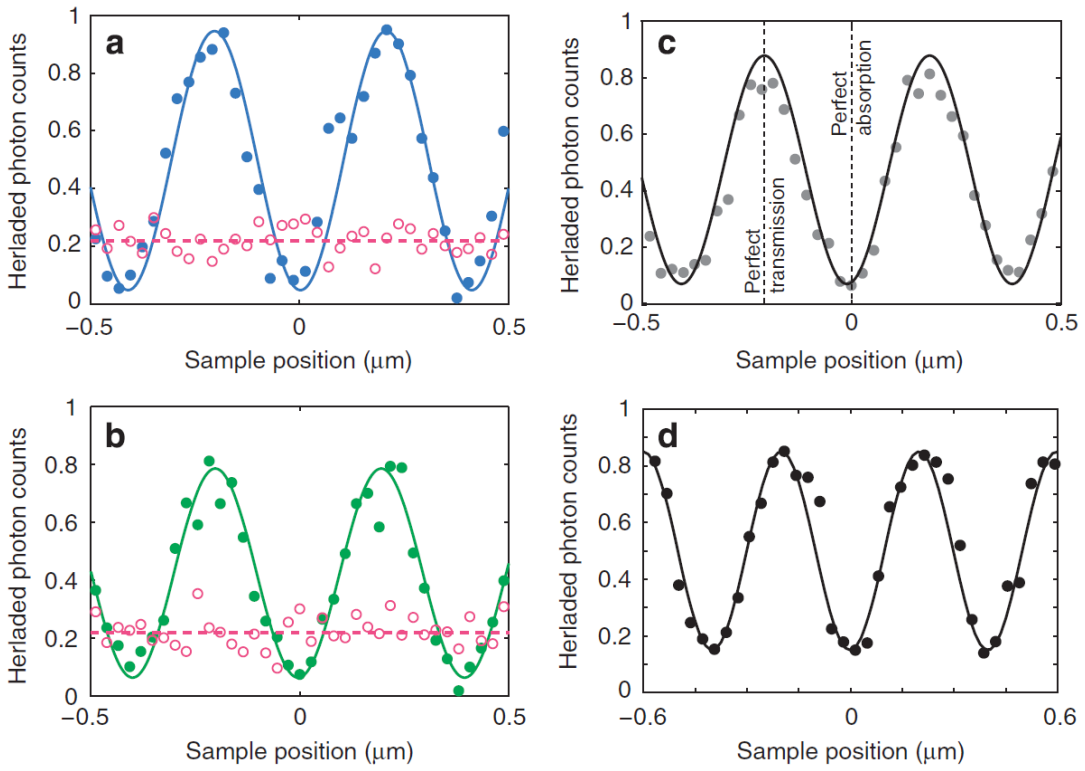

Figure 7-2 **Single-photon coherent absorption at a wavelength of 810 nm. (a,b)** The normalized output photon count rates in channels γ (a) and δ (b) as a function of the plasmonic absorber position along the standing wave (blue and green full circles). Also shown is the behavior of the output channels when input channel β is blocked (pink open circles and dashed horizontal fitting lines). **(c)** Half-sum of the normalized rates in channels γ and δ. The vertical dotted lines indicate the positions of nodes and antinodes, corresponding to perfect transmission and absorption regimes, respectively. **(d)** Half-sum of the normalized rates in channels γ and δ for a 50% absorber made of a 30-layer graphene film [35]. Figure adapted from Ref. [35].

In more details, entangled photons pairs, at a wavelength of 810 nm, were created by spontaneous parametric down conversion (SPDC) of laser light at a wavelength of 405 nm by illumination of a beta-barium borate (BBO) crystal. Then, as shown in the the photon pair was separated by a knife edge prism and, consequently, one photon of the correlated pair was launched into a photon counter to herald the presence of the other photon that was launched into the interferometer [35]. The single photon experiments comprise two input (α and β) and two output (γ and δ) channels (four-port optical device). The input single photons were focused on the metasurface sample and the output channels were detected with single-photon avalanche detectors (SPDs). The metasurface structure consists of asymmetric split

ring resonators (similar to the metasurfaces used in previous chapters) with a unit cell size of 350 x 350 nm^2.

Figure 7-2(d) shows the modulation of absorption using an alternative sample for thin absorber. Here, thirty layers of graphene were used, which absorb about 50% of a single beam of incident light. Any materials of deeply sub-wavelength thickness with this level of absorption can replicate such performance. It is important to note that the use of metasurfaces offers a controllable way to shift the optical properties by scaling up or down the structural parameters as well as the size of the unit cell of the metasurface.

So, in this section, we reported on recent findings of coherent control of absorption down to the quantum regime. Prior work has shown that a travelling photon can be coupled into a plasmon resonance of a metasurface. The demonstration of control of quanta of light with light on a metasurface took place in a free-space setup and it was shown that any thin material with the ideal optical properties can replicate such performance (i.e. multi-layer graphene). In the next section, we report on how this approach can be integrated with optical fibre technology with potential applications in coherent quantum signal processing networks.

7.2 Coherent control of single photons in optical fibre networks

In the previous section it was shown that coherent control of absorption in a film of sub-wavelength thickness holds at the quantum level and that a single photon can be deterministically coupled to a plasmonic mode of a metasurface. Coherent control of light absorption is a concept that can support all-optical signal processing (see Chapter 3). In this way, single photons can trigger or eliminate absorption in a thin material. Consequently, the integration of coherent control of light with light with telecommunication optical fibres opens new paths for ultrafast information processing with power consumption at the lowest possible level. Here we report on the first demonstration of a plasmonic fibre-integrated metadevice that supports optical signal processing functions down to the quantum regime.

Although, there are some challenges that one should address. Firstly, the current SPDC process generates photon pairs at a wavelength of 810 nm, while all metadevices shown in previous chapters concern applications in the telecommunication C-band. Moreover, the micro-lenses used, for light collimation and focusing, operate around 1550 nm wavelength with huge losses at 810 nm (see section 2.3). Secondly, the phase instabilities within the fibre network. Quantum measurements require more time for signal detection and stability of our fibre interferometers on sub-second timescales is not sufficient for recording enough photons.

Here, we report on how these challenges can be addressed. In subsection 7.2.1, we present a metadevice, where no microcollimator lenses used, with operation wavelength at 810 nm. Moreover, we propose a post-processing data interpretation technique where random phase fluctuation of the fibre interferometer can be excluded. In subsection 7.2.2, we investigate an active stabilization scheme that can eliminate random phase drifts on demand for hours.

7.2.1 Coherent perfect absorption of single photons in a fibre network

Here we demonstrate the phenomenon of coherent perfect absorption of single photons in a fully-fiberized ultrathin plasmonic metasurface fabricated on the end face of an optical fibre. Continuous control of single-photon absorption probability is achieved by driving the network between the regimes of coherent perfect absorption and coherent perfect transmission. To overcome phase fluctuations in optical fibre networks, we implemented a reference-based post selection technique, which yielded interference fringe visibility comparable to that of free-space experiments [35].

Our fibre interferometers are stable on second timescales, which is sufficient for proof-of-principle demonstrations (see previous chapters) although for quantum experiments the acquisition time needed for collection of enough photons exceeds such time scales.

Conventionally, active stabilization of a fibre interferometer comprises a feedback loop (a reference laser at a different wavelength and photodetectors, for detection of power fluctuations, driving an additional phase modulator to compensate for the random phase drift) that increases the setup's complexity. Here, we propose a simplified data processing method, where the data is acquired during time intervals, which are shorter than the characteristic phase fluctuation time.

In this work, entangled single photon pairs are generated, by SPDC, at a wavelength of 810 nm, see Figure 7-3(a). Thus, the metamaterial was fabricated with a scaled down unit cell size of 360 x 360 nm^2 in order to shift its optical response to the desired wavelength (Figure 7-3(b)). Moreover, in section 2.3 the encapsulation and packaging technique of such fibre metamaterials was discussed. Briefly, the fibre metamaterial was coupled to another bare fibre by bringing the fibre ends together and attaching them gently, in order to avoid damage of the metasurface, within a fibre micro-ferrule. Then, additional glass ferrules were added and UV-cured adhesive was applied in every step. Finally, the resulting assembly was placed in a protective stainless steel package (inset in Figure 7-3(a)). The resulting metadevice has fibre-pigtails and is fully compatible with standard fibre-optic components.

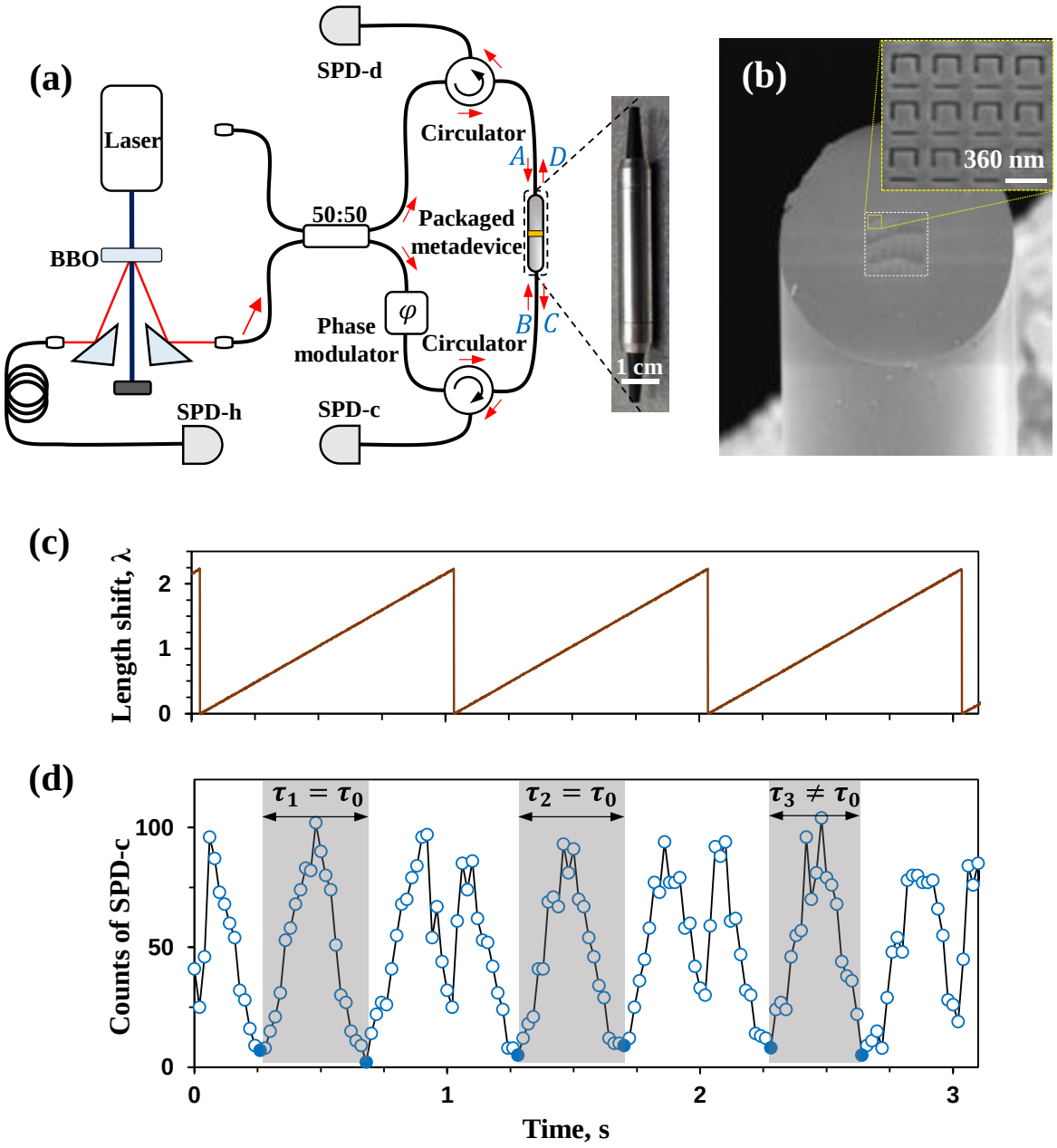

Figure 7-3 **Fiberized setup for studying coherent absorption of single photons and reference-based post-selection technique**. **(a)** Schematic of the fiberized quantum network. The inset shows a photograph of the packaged metadevice. **(b)** SEM images of the fibre metamaterial fabricated on the end face of an optical fibre and its unit cell. **(c)** Periodic length changes of one arm of the interferometer plotted in photon wavelength units (λ=810 nm) and applied using a fibre-stretcher. **(d)** Total single photon counts measured at the detector SPD-c. Minima correspond to the coherent absorption regime (filled dots). The time intervals τ_i between these points (shaded regions) are compared with the expected value τ_0 in the absence of noise. Time intervals $\tau_i \approx \tau_0$ are unlikely to be affected by thermal phase fluctuations of the interferometer and thus used for further data analysis. Data measured by Dr. Anton Vetlugin.

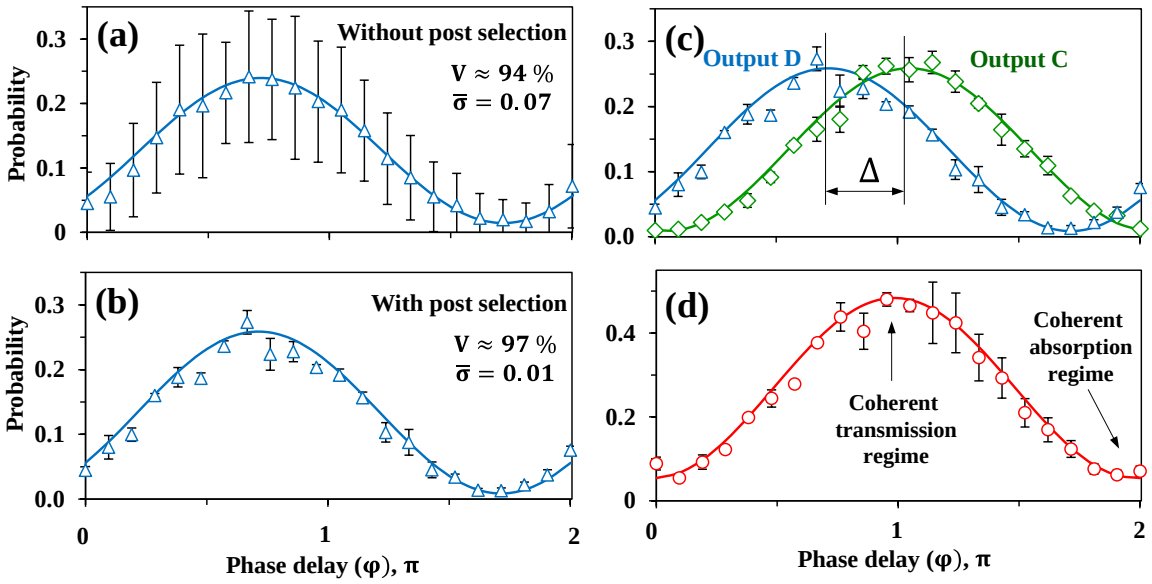

Figure 7-4 **Detection of single photon coherent absorption with a reference-based post-selection technique**. Probability to detect heralded single photons at output channel D without **(a)** and with **(b)** post selection. The visibility (V) and average standard deviation ($\bar{\sigma}$) are shown for each graph. Solid curves show fittings of the data. **(c)** Measured probabilities of the heralded photons to be measured in output C (rhombi) and output D (triangles) as a function of the relative phase between the two arms of the interferometer. The non-zero phase shift between the two outputs (Δ) is explained by metadevice fabrication imperfections and by its structural asymmetry due to the fabrication of the metasurface on the end face of an optical fibre. **(d)** Total single-photon detection (circles) probabilities (D+C) as a function of the relative phase between the two arms of the interferometer. For analytical expressions of the fitting lines see 7.2.4. Data measured by Dr. Anton Vetlugin.

The data processing technique used here is the reference-based post selection. In details, the length of one arm of the interferometer is periodically modulated at a rate that is faster than the characteristic timescale of thermal drift. A piezoelectric fibre stretcher, with a fibre stretch of 0.14 μm/V, was placed in the one arm of the interferometer. The fibre stretcher was used as phase modulator to produce a phase delay (φ) between the two arms of the interferometer. The modulation amplitude (in terms of voltage applied to the fibre stretcher) that we chose exceeds two wavelengths of light (Figure 7-3(c)), thus, in each modulation cycle the interferometer reaches the condition of coherent absorption (filled points in Figure 7-3(d)) twice. The time interval τ_i (where i stands for the number of measurements) is the time required for one full oscillation (period), marked by two points of

coherent absorption, and should be equal to an expected value τ_0 (Figure 7-3(d)). If this is the case, then the data obtained during such intervals are unlikely to be affected by the thermal phase fluctuation and are used to characterize the photon absorption. Importantly, our data analysis considers only time intervals of $t_i \approx \tau_0$. Briefly, the data are post-selected after recording a large number of modulation cycles (~ 200). Moreover, the coincidence counts between photon detectors SPD-h and SPD-c (SPD-d), recorded during noise-free intervals, are used to characterize the probability of a heralded single photon to be detected in the output C (D).

To validate the efficiency of the reference-based post selection technique we recorded interference fringes of output D without (Figure 7-4(a)) and with Figure 7-4(b)) data processing applied. The post-selection resulted in reduction of the average standard deviation by 7 times (up to 30 times for some measurement points) and improvement of the visibility of modulation by 3%. By applying post-selection, we demonstrated the quantum regimes of coherent absorption and transmission in a fibre network. We measured the probabilities p_c and p_d of detecting a heralded single photon at outputs C and D of the metamaterial absorber, respectively (Figure 7-4(c)). By scanning phase, we observed periodic, close to in-phase, oscillation of probabilities in a good agreement with previous work [35]. The phase shift Δ between the output probabilities C and D can be attributed to the asymmetric structure of the metadevice that contains a metasurface fabricated on top of one of the two coupled fibre ends. The total probability p, where $p = p_C + p_D$ (see 7.2.4), of the heralded single photon detection (Figure 7-4(d)) is modulated between 0.05 and 0.48 with the lowest (highest) value corresponding to the coherent absorption (transmission) regime. Modulation amplitudes below 0.5 of p_c, p_d (below 1of p) can be attributed to fibre-to-fibre coupling losses and fabrication imperfections of the fibre metamaterial. Nevertheless, this does not affect the visibility of the curves much, which is as high as 90% for p_c and p_d and equals to 80% for p.

In summary, we have demonstrated continuous control over single-photon absorption probability in a fully-fiberized quantum network with a high visibility. The coherent absorber was a fibre-integrated plasmonic metamaterial. In order to overcome thermal phase drifts, without increasing the setup's complexity, we developed a data processing procedure that uses the total counts of single photon detectors as a reference. We anticipate that such post-processing techniques may be used for applications where impractical increases of setup complexity would arise from other approaches such as active stabilization.

7.2.2 Active stabilization of coherent fibre networks

In this subsection, we propose a simple method for active phase stabilization of coherent fibre networks operating at a single-photon level. The proposed approach is based on the single-photon signal itself, therefore, it requires no additional optical elements and equipment that induces losses and degradation of the quantum signal. While the method is slow compared to conventional stabilization techniques, it offers significant simplification of the stabilization scheme and, thus, increases the overall efficiency of the quantum network. Thereafter, we demonstrate all-optical single-photon switching in a stabilized quantum network by exploiting coherent absorption.

Active phase stabilization techniques are required in setups, especially in fibre-optic ones, where thermally induced phase fluctuations affect the measurements signal. These techniques, based on a feedback loop, exploit an additional CW laser with a distinct degree of freedom (wavelength, polarization etc.), which propagates within the same optical path where quantum light propagates [146-148]. Briefly, laser light passing through different components of the network acquires information on the phase relation between these parts, which can be extracted by measuring the light power distribution between the output channels (C or D) of the network. Any phase fluctuation changes this distribution. This change is used to generate a feedback signal. Then, the signal is sent to a phase modulator resulting in compensation of the phase fluctuations. In order to separate quantum and CW laser light, multiplexers (e.g. wavelength division multiplexers, dichroic mirrors, polarizers) and photodetectors are required as well as filtering in quantum channels in order to remove CW laser light. This leads to a combination of coupling-insertion losses between the additional fibre-optic components and, consequently, to degradation of the quantum signal.

Here, we propose a more simple stabilization technique. In order to test our stabilization scheme, we replaced the metadevice with a 50:50 coupler. In details, we launched a strongly attenuated CW laser light into the fibre-optic network (see Figure 7-5(a)), where the first 50:50 coupler splits the photon wavefunction into a superposition of two spatial modes, describing propagation in the two arms of the interferometer. The fibre interferometer is composed of polarization maintaining (PM) single-mode fibres (as all previous experiments) with a length of each arm of the interferometer of around 15 meters. Due to interference on

the second coupler, the probability of the photon to take one of that beamsplitter's outputs depends on the phase retardation between two optical paths. To estimate this probability, the distribution of photons at the output ports is measured by SPDs during a time interval t_o. To set t_o, in this experiment, we first measured the phase fluctuations which affect the network. The typical spectrum of the fluctuations is measured by launching light from a CW-laser of μW power through the interferometer (shown in the inset of Figure 7-5(b)). The noise is present at frequencies up to $\Delta f_N \approx 1\,Hz$ with no significant contribution above this frequency. Thus, it allows us to operate at $t_o = 24\,ms$ ($t_o \ll 1/\Delta f_N$).

Regarding the stabilization now, let us assume that the number of photons N_c (N_d) detected by SPD-c (SPD-d) during a time interval t_o, which is proportional to the probability p_c (p_d) of the photon to leave the interferometer through the corresponding output channel, is given by:

$$N_c(\varphi) = N \cdot p_c(\varphi)$$

$$N_d(\varphi) = N \cdot p_d(\varphi)\,,$$

where $N = N_c(\varphi) + N_d(\varphi)$ is the total detected output photon number. For lossless beamsplitters N is independent of phase retardation φ between the two arms of the interferometer. Probabilities p_c and p_d are defined as in section 7.2.4:

$$p_c(\varphi) = (1 + \sin\varphi)/2$$

$$p_d(\varphi) = (1 - \sin\varphi)/2.$$

If the phase retardation is fixed, $\varphi = \varphi_{fix}$, and system is not affected by phase noise, N_c is constant and equal to the set value $N_c^{fix} = N_c(\varphi_{fix})$. More specifically, the number of detected photons should be within a Poisson distribution centred at N_c^{fix}, considering the random nature of the laser source (N fluctuates). We normalize the N_c (within a range) to account for the laser power fluctuations by measuring the laser power with a reference photodiode. If the interferometer is affected by phase noise during t_o, then the difference

$N_c - N_c^{fix}$ becomes noticeable. We set $N_c^{fix} \approx N/2$ (in the middle of the sinusoid), so that the sign of $N_c - N_c^{fix}$ tells us in which direction the phase has changed, and an appropriate feedback signal (voltage) is applied to the phase modulator, in order to compensate for the fluctuation, minimizing $|N_c - N_c^{fix}|$. Here, a fibre stretcher used as phase modulator, which induces a phase shift proportional to the applied voltage V, so that phase retardation becomes a function of V, $\varphi = \varphi(V)$.

The performance of the method was tested for fourteen hours (Figure 7-5(b). The fibre-optic setup was stabilized during the first seven hours followed by seven hours of a free running regime with stabilization turned off (only the first hour of free running is shown). Each point, in Figure 7-5(b) (left), is shown as a number of single-photon counts detected by SPD-c during $t_o = 24\,ms$. The sampling period is set to 10 seconds. The active stabilization scheme leads to a significant reduction of phase fluctuations: the standard deviation of 850 counts for the free running regime is reduced to 100 counts for the stabilized regime. The performance of the method in terms of phase stability is shown in Figure 7-5(b) (right top) with the phase distribution shown in Figure 7-5(b) (right bottom). The Gaussian fit with rms width $\sigma = 0.07$ rad implies that the optical path length fluctuation between the interferometer arms is less than 10 nm. This value is comparable with conventional stabilization schemes [146-148]. Although, we note that the length of the interferometer is significantly shorter than in other experiments. In the case of a long-distance fibre-based quantum communication channel, the network may require multi-step control sequences for the compensation of the fiber path-length difference. While, our stabilization scheme satisfies the phase stability required for interferometers as long as tens of meters, its bandwidth is limited by the single-photon integration time and may not satisfy the stringent requirement of a long-distance fibre quantum network suffering from high frequency noise.

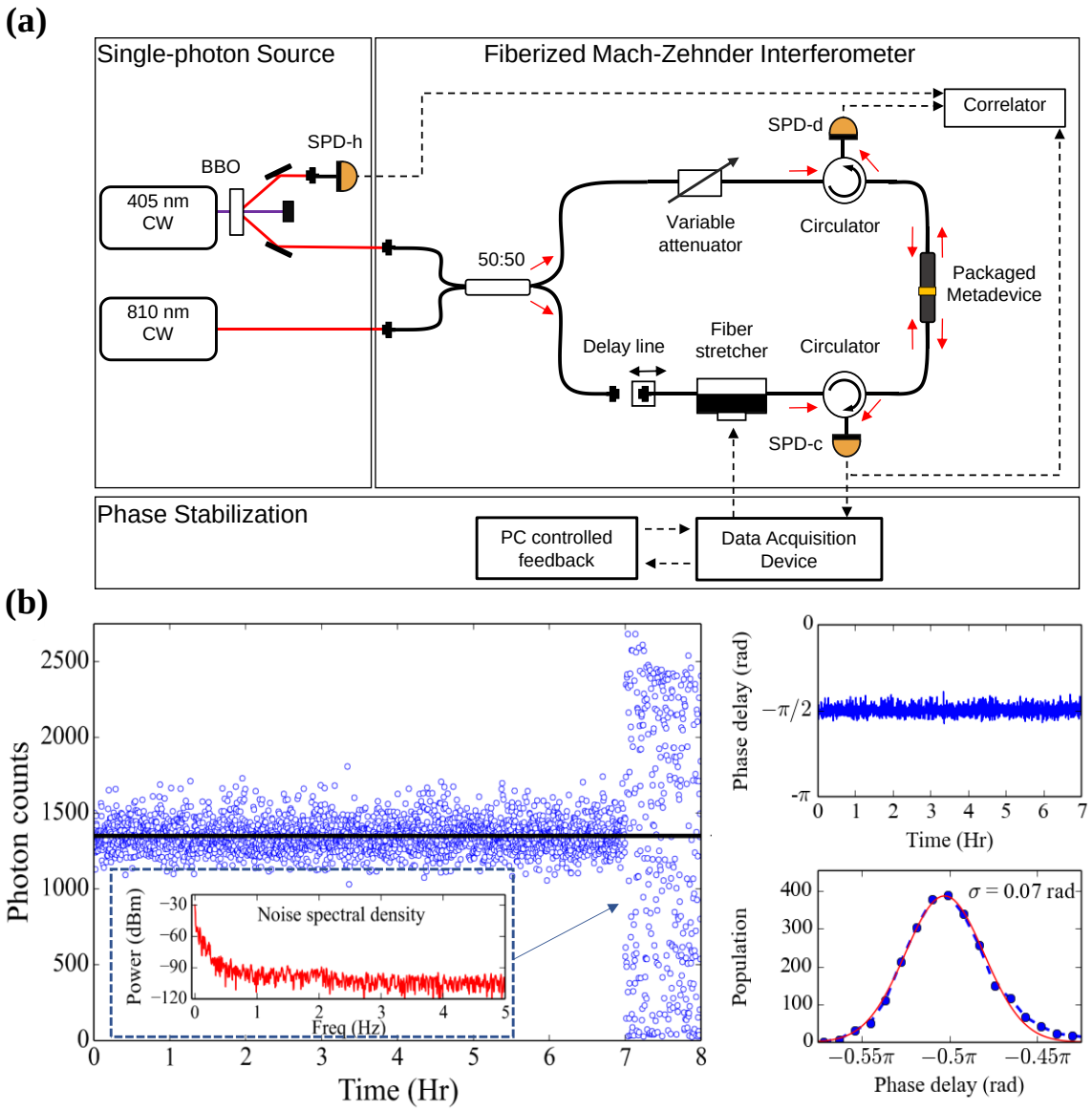

Figure 7-5 **Fiberized interferometric network for active stabilization down to the quantum regime. (a)** A CW laser at a wavelength of 405 nm pumps a BBO crystal to generate entangled photon pairs at a wavelength of 810 nm (for measurements with strongly attenuated light a CW laser at a wavelength of 810 nm is used). Then, one photon is detected by SPD-h and one photon is launched into the interferometer, then its wavefunction is split with a 50:50 beamsplitter and recombined at the packaged metadevice. Output signals are collected via circulators, detected by SPD-c and SPD-d that were connected to a photon counter (correlator) and an acquisition device that drives the fibre stretcher. **(b)** Left: Interferometer output SPD-c as a function of time, where the fibre network was stabilized for 7 hours and then the stabilization was switched off. The inset shows the noise spectral density of phase fluctuations when the stabilization is turned off. Right: (top) The performance of the method in terms of phase stability with its phase distribution (bottom), where the red line is a Gaussian fit with rms width of $\sigma = 0.07$ rad, which indicates that the optical path length fluctuates by around 10 nm. Data measured by Salih Yanikgonul and Dr. Ruixiang Guo.

7.2.3 Controlling single photon interference and all-optical switching

Moreover, we have tested the stabilization scheme in a single-photon interference experiment. We performed measurements of single-photon interference (Figure 7-6(a)) according to the p_c and p_d equations (see above) in the following way. First, the voltage at the fibre stretcher is adjusted to $V = V_{fix}$ so that $\varphi(V_{fix}) = \varphi_{fix}$ and $N_c(\varphi_{fix}) = N_c^{fix}$, accordingly. The network is stabilized at this point by the introduced feedback system. Then, the feedback is switched off for a time period of t_o, during which the phase is shifted in a discrete way,

$$\varphi_n = \varphi(V_{fix} + n \cdot \Delta V) = \varphi_{fix} + n \cdot \Delta\varphi$$

where $\Delta\varphi = 0.1\pi$ and $n = 0, \pm1, \pm2, \ldots$ The number of photons $N_c^n = N_c(\varphi_n)$ and $N_d^n = N_d(\varphi_n)$ at the output channel detectors SPD-c and SPD-d is recorded, respectively. Then, the fibre stretcher if shifted back to $V = V_{fix}$, and, if required, the voltage is adjusted to bring the photon counts of SPD-c close to N_c^{fix} (so, V_{fix} changes in time, compensating phase fluctuations, which guarantees that we set each φ_n starting from the same initial phase). The procedure is repeated with the next value of n in the equation above. An excellent agreement between experimental data (points in Figure 7-6(a) (top) and theoretical predictions of p_c and p_d (lines) proves the consistency of the proposed stabilization technique.

Controllable photon absorption, shown in Figure 7-6(a) (bottom), can be used to implement single-photon switching devices (complete dissipation of single photons), which is not possible with a beamsplitter that, in fact, redirects the input light to two output channels. Coherent perfect absorption takes place when the 50:50 beamsplitter is replaced by an absorber/lossy beamsplitter with, in the ideal case, $t = -r = 1/2$ (t and r – field transmission and reflection coefficients). Probabilities of photon detection at output channels of the absorber are defined (for the probabilities of a lossless beamsplitter see 7.2.4), as:

$$p_c(\varphi) = p_d(\varphi) = (1 - \cos\varphi)/4,$$

with a total absorption probability, $p = 1 - (p_c + p_d)$, varying from 1 to 0. Here we used a setup with phase stabilization (Figure 7-5(a)), which allows us to overcome the phase fluctuation problem and manipulate photons in a controllable way.

The stabilization procedure is the same as described in the previous subsection, but as a reference for the feedback system we use the total counts of SPD-c and SPD-d,

$$N_{ref} = N_c + N_d = N \cdot (1 - \cos\varphi)/2,$$

since, N_c and N_d are expected to have the same phase-dependence. Here N is the total photon number detected by both SPD-c and SPD-d in the case that the metadevice is replaced by a bare fibre. The stabilization point, N_{ref}^{fix}, is set in the middle, $N_{ref}^{fix} \approx N/2$. The result of stabilization is similar to the one shown in Figure 7-5(b).

After stabilizing the system, we measured the interference pattern (N_c and N_d), see Figure 7-6(a) (bottom). Here, each point corresponds to a single measurement with no post-processing, which is only possible with active phase stabilization. As the network is driven to the coherent absorption regime, by changing the phase of one of the interferometer arms by $\pi/2$, the input photons are dissipated by the metadevice and the total number of counts ($N_c + N_d$) reaches a minimum. If the phase is changed by $-\pi/2$, then the network is in the coherent transmission regime, where the input photons are transmitted through the metadevice, resulting in a maximized total number of counts. We obtained visibilities of 0.89 ± 0.05 and 0.86 ± 0.05 for $p_d(\varphi)$ and $p_c(\varphi)$, respectively, and a visibility of 0.73 ± 0.03 for the total detection probability ($p_c + p_d$). This value is lower than the visibility of ~ 0.8 reported in subsection 7.2.1, because the former is obtained from a single-run measurement, whereas the latter was achieved by averaging many runs. The reason for non-zero minimum total counts is mainly due to the fabrication imperfections of the metadevice, which results in the $\pi/4$ phase shift between $p_c(\varphi)$ and $p_d(\varphi)$ Figure 7-6(a) (bottom)), and due to the dark count of the single-photon detectors. The experimental results (data points) agree with predictions (fitting dashed lines).

Thereafter, we investigated the reproducibility of the phase stabilization scheme. We drove the network from the coherent absorption to the coherent transmission regimes and vice versa, as described above. Figure 7-6(b) (left) shown transitions between the coherent states in terms of including the recorded coincident photon counts. The flux of randomly arriving photons is transmitted at coherent transmission regimes while it is almost totally absorbed at the coherent absorption regimes, showing effective all-optical single-photon switching. Blue lines represent a coincidence detection of photons between the photon detectors SPD-h−SPD-c and SPD-h−SPD-d in time. The red line highlights the corresponing coherent phase stabilized states of the fibre-optic network. In details, the visibility is enhanced from 0.73 to almost 0.80 due to the coincidence nature of the signal, which excludes the dark counts of the detectors within the coincidence time window of 3.24 ns (chosen accordingly). We obtained mean photon numbers of 1.00 (7.97) with a standard deviation of 0.99 (2.82) for the coherent absorption (transmission) regimes, see Figure 7-6(b) (right). These results are in good agreement with the expected mean photon number of 0.92 (8.2). The photon numbers follow a Poisson distribution.

To conclude, we have presented a simplified technique for active phase stabilization of coherent fibre networks that can operate with single photon signals. Our approach does not require an additional laser source and fibre-optic components, and thus does not increase losses. The output photon flux can be used as a feedback mechanism, directly. More specifically, we achieved phase stability of 0.07 rad, which corresponds to, approximately, 10 nm optical path length fluctuation. Thereafter, we tested the reproducibility of the phase stabilization scheme resulting in visibility as high as 0.8 by exploiting quantum coherent absorption, which reaches the visibility values for free-space experiments [35]. While our method is slow compared to conventional stabilization schemes, it offers significant simplification of the stabilization process and increases the overall efficiency (low loss) of the quantum channels.

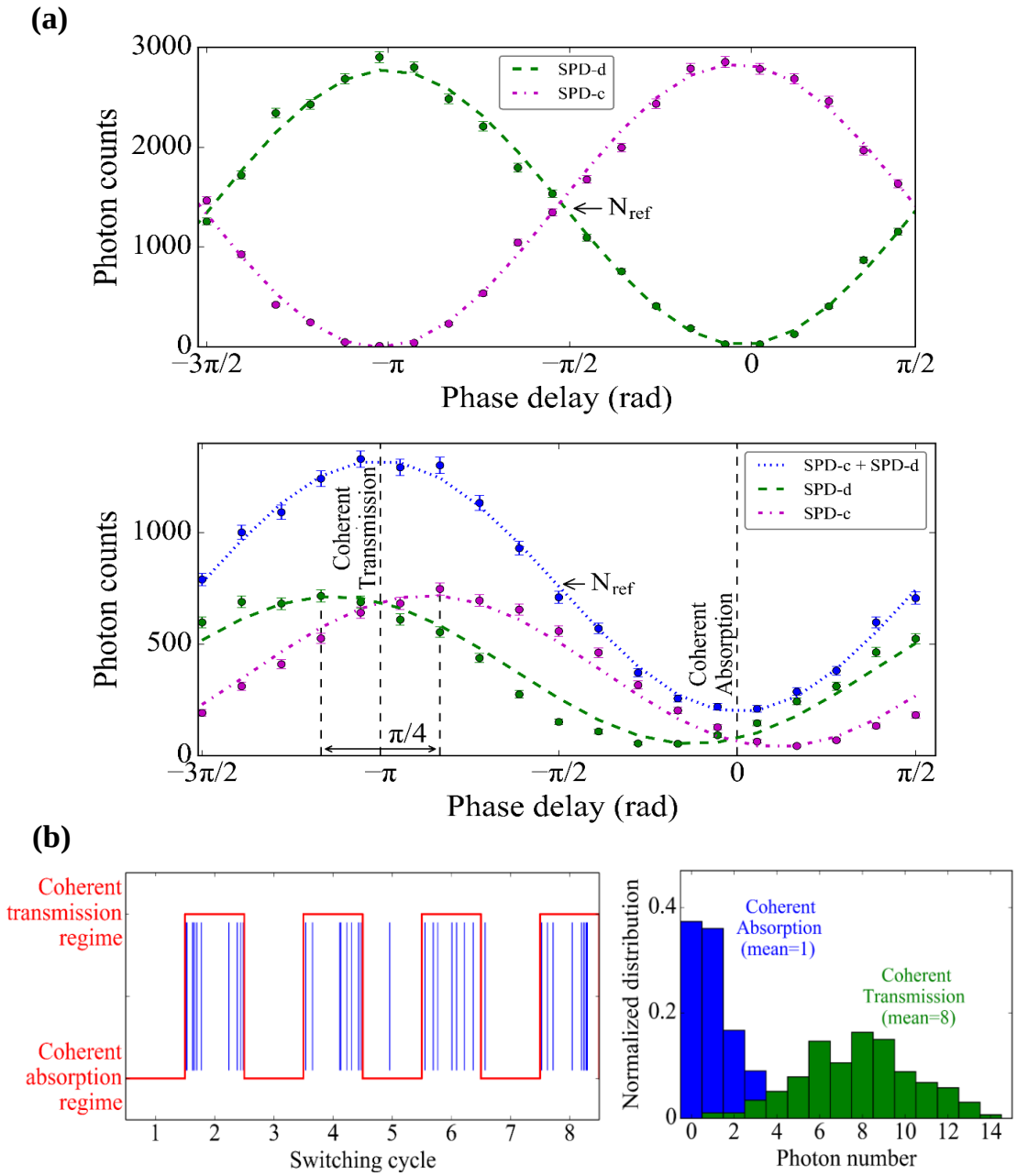

Figure 7-6 **Active control of absorption and transmission of photons.** **(a)** Top: Photon counts of the output channels C and D as a function of the relative phase for a low loss beamsplitter. Bottom: Photon counts of the output channels C and D as a function of the relative phase of the input wavefunctions for the coherent absorber metadevice. **(b)** Left: Following the stabilization of the network, the feedback is switched off and the system is driven between the coherent transmission and absorption regimes for t_o by applying voltage to the fiber stretcher that results in $\varphi_{fix} + n \cdot (\pi/2)$ phase shift, where $n = \pm 1$. The graph shows single photon detection events during these regimes. Right: Statistics of photon detections, which follow a Poisson distribution. The mean numbers of photons detected in the coherent absorption and transmission regimes are ~ 1 and ~ 8 photons, respectively. Data measured by Salih Yanikgonul and Dr. Ruixiang Guo.

7.2.4 Photon interference on a lossy beam splitter

For fitting the experimental data in Figure 7-6 we have used the following consideration. In order to introduce quantum regimes of perfect absorption and perfect transmission let us consider an ultrathin lossy beamsplitter, or absorber, that produces a π-phase shift between transmitted and reflected fields [35, 44]. If such a beamsplitter is interrogated with a single photon, the wavefunction of which is split beforehand and recombined at the beamsplitter, the two opposite outcomes are possible, depending on the phase shift φ between two "parts" of the split photon's wavefunction at the thin absorber: 1) constructive interference of reflected and transmitted fields if $\varphi = \pm\pi$, and 2) destructive interference when $\varphi = 0$. In the first case the photon passes through the absorber without disturbance, while in the second case it is absorbed (the absorption probability in a standing wave reaches unity if absorption of the beamsplitter in a traveling wave is 50%). These two limited cases are known as coherent perfect transmission and coherent perfect absorption, respectively. In more detail, the quantum state of the photon under consideration is described by a path-entangled wave function:

$$|\psi\rangle = \frac{1}{\sqrt{2}}\left(|1\rangle_A|0\rangle_B + e^{i\varphi}|0\rangle_A|1\rangle_B\right), \quad (1)$$

where index $A(B)$ corresponds to the top (bottom) input field of the absorber in Figure 7-3(a) and is related to the annihilation operator $\hat{a}$ ($\hat{b}$), satisfying commutation relations, $[\hat{a}, \hat{a}^\dagger] = [\hat{b}, \hat{b}^\dagger] = 1$, $[\hat{a}, \hat{b}^\dagger] = 0$. The wave function $|\psi\rangle$ also contains a controllable relative phase φ, which is accumulated during propagation through the arms of the interferometer. A thin lossy beamsplitter mixes the input amplitudes and adds the Langevin noise operators $\hat{f}_c$ and $\hat{f}_d$ which are responsible for commutation relations conservation [149, 150]:

$$\hat{c} = t\hat{a} + r\hat{b} + \hat{f}_c, \quad \hat{d} = r\hat{a} + t\hat{b} + \hat{f}_d.$$

Here $\hat{c}$ ($\hat{d}$) is the annihilation operator related to the bottom (top) output field of the absorber in Figure 7-3(a), and t (r) is the field transmission (reflection) coefficient of the

traveling waves. It is straightforward to calculate the probabilities p_c and p_d of detecting a photon at the corresponding output ports of the absorber as:

$$p_c = \langle \hat{c}^\dagger \hat{c} \rangle = (|t|^2 + |r|^2 + 2|t||r| \cos(\varphi - \Delta_{tr}))/2, \quad (2)$$

$$p_d = \langle \hat{d}^\dagger \hat{d} \rangle = (|t|^2 + |r|^2 + 2|t||r| \cos(\varphi + \Delta_{tr}))/2, \quad (3)$$

where $t = |t|e^{i\theta_t}, r = |r|e^{i\theta_r}$ and $\Delta_{tr} = \theta_t - \theta_r$ and quantum mechanical averaging is performed with initial state (1). We note that averaging of any contributions containing noise operators is equal to zero [149]. Assuming $|r| = |t|$, (2) and (3) simplify as:

$$p_c = |t|^2(1 + \cos(\varphi - \Delta_{tr})), \quad (4)$$

$$p_d = |t|^2(1 + \cos(\varphi + \Delta_{tr})). \quad (5)$$

In the case of a lossless beamsplitter, where $|r| = |t| = 1/\sqrt{2}$ and $\Delta_{tr} = \pm\pi/2$, the probabilities p_c and p_d oscillate (with continuous modulation of φ) out of phase – a well-known single photon interference effect. On the contrary, for an ideal lossy beamsplitter with $|r| = |t| = 1/2$ and $\Delta_{tr} = \pm\pi$, the probabilities p_c and p_d oscillate in phase, both varying in the range of $0 - 0.5$ with total detection, or total transmission probability p, given by:

$$p \equiv p_c + p_d = (1 - \cos\varphi)/2. \quad (6)$$

From the above analysis, we concluded that for $\varphi = \pm\pi$ the transmission probability (6) is equal to one and the photon passes through the absorber without losses, while for $\varphi = 0$ the transmission probability is equal to zero and the photon is absorbed, deterministically.

7.3 Conclusions

Here we proved that coherent control of light with light in planar metasurfaces holds down to the quantum regime. Moreover, we presented findings that the aforementioned concept can be integrated with fibre technology resulting in fibre metadevices that are compatible with standard fibre-optic components. Random phase drift introduced by thermal expansion of the optical fibres is the major drawback throughout this Thesis. Here we have provided two methods that one can use to overcome such problems. First, a post-processing analysis, which excludes the random phase drifts by taking into account only collected data within a specified time window. Second, an active phase stabilization that uses the output photon flux as a feedback mechanism to drive a phase modulator that can compensate for photon count fluctuation. Such stabilized fibre-optic interferometers may find applications in quantum information networks, cryptography as well as all-optical data processing architectures.

Chapter 8 Conclusion and outlook

8.1 Summary

In order to pass from the "age" of metamaterials to that of metadevices, active metasurfaces that can be integrated with standard technology are needed. Until now the area of metamaterials was considered an exotic research field that can offer solutions but is limited by its low integrability. This Thesis provided evidence that metasurfaces can be used and implemented in optical fibre technology. More specifically, here I used coherent control of absorption of light to demonstrate all-optical functions that may find a plethora of applications (see previous chapters). Extremely low power consumption (single photon signals) and THz modulation rates are proven and most importantly, the technology implementation can be achieved with conventional equipment. Here I reported on:

- The fabrication and integration as well as the theoretical characterization of the first fibre-optic metadevice. The metadevice comprises standard fibre-micro-optics and it is compatible with standard fibre-optics components.

- Optical signal processing that is superior to electronic signal processing in terms of bandwidth and energy consumption. In Chapter 3 I have shown all-optical signal switching, effective nonlinearity and logical functions XOR, NOT and AND, which were performed within a coherent fibre network at wavelengths between 1530 and 1565 nm. The metadevice has been tested at up to 40 Gbit/s with energy consumption as low as 2.5 fJ/bit. Such all-optical signal processing may find applications in "photonic circuits" where a light beam can control another light beam.

- The fastest, to my knowledge, selective transmission/absorption in the telecommunications C-band with 1 THz bandwidth in a fibre-optic scheme. In Chapter 4 I demonstrated pulse shaping and converted bright pulses into dark pulses.

Such dark-pulse generation could be applied to any pulse sequence, shape and repetition rate. Lastly, I have shown that the operation of the metasurface absorber (lossy beamsplitter) is different from a coupler (lossless beamsplitter), resulting in two synchronously and asynchronously modulated outputs, respectively.

- The first demonstration of a fibre-optic plasmonic metadevice for data security applications using optical signals with strong phase correlation. In Chapter 5 I introduced the concept of coherent cryptography, an optical layer secure communication protocol that does not rely on nonlinear optical processes but instead uses energy redistribution of coherent optical waves interacting on a metasurface absorber. I demonstrated different types of encryption modes and reported a scheme providing perfect secrecy in a fully-fiberized network at a bit-rate of 3 Gbit/s at the telecommunications wavelength of 1550 nm.

- In Chapter 6, I performed nonlinear control of coherent absorption in a nonlinear fibre network containing a plasmonic metasurface absorber. I exploited power-dependent phase retardation arising from the Kerr effect, and more specifically self- and cross-phase modulation, for all-optical noise suppression, power-limiting, pulse restoration, pulse splitting and signal transfer between carrier wavelengths. The findings indicate that nonlinear control of coherent absorption can imitate and outperform saturable and multi-photon absorption in coherent light applications.

- Lastly, I have developed fibre metadevices with operation wavelength at 800 nm, which enabled the first demonstration of coherent perfect absorption and transmission of single photons in a stabilized quantum fibre network (see Chapter 7).

In conclusion, this Thesis merged the physics of metamaterials with optical fibre technology. I have demonstrated low-power and THz-bandwidth all-optical signal processing applications within fibre networks. I have applied metamaterials technology to different research fields ranging from all-optical modulation to optical encoding and pulse shaping. Beyond fibre technology, I anticipate that such metadevices may be integrated with other photonic platforms i.e. silicon photonics.

8.2 Outlook

In this Thesis, I mainly discussed the possibilities/applications enabled by a single metasurface patterned directly on the top of a single optical fibre. However, more complex geometries are important in fibre technology. For example, multi-core fibres, hollow-core fibres and few fibres bonded together, where metasurfaces with a range of different functionalities could be fabricated on the top of each fibre core. Thereafter, the fibre-metasurface hybrids could be integrated in a way similar to that shown in section 2.3.

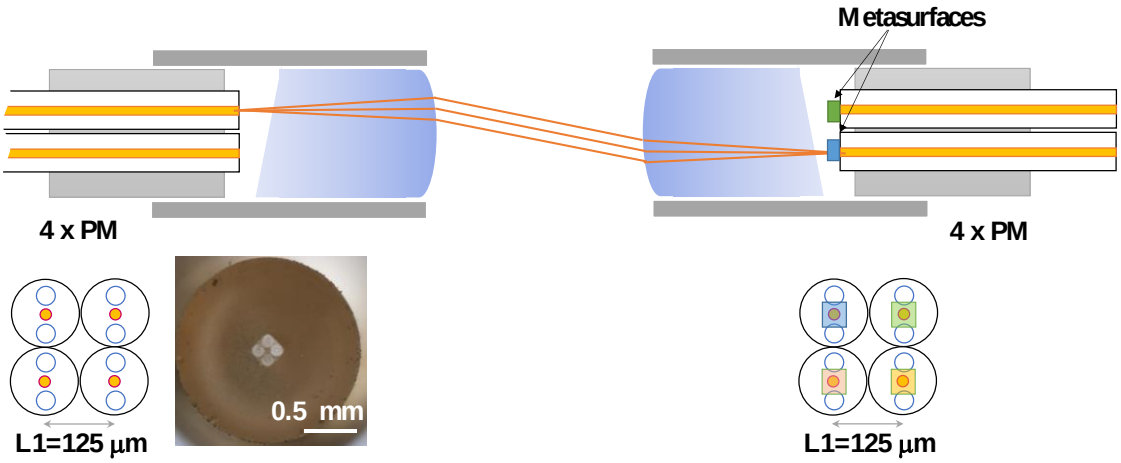

Figure 8-1 **Multi-fibre polarization-maintaining packaging.** The schematic shows four polarization maintaining fibres coupled together with a set of microcollimator lenses. Focusing can be adjusted to ensure that light coming out from a bare fibre is efficiently coupled into the corresponding metamaterial fibre. The distance between the cores L1 is 125 µm. Schematics show the polarization-maintaining fibres where boxes of different color stand for metasurfaces with different optical properties. The inset shows an optical microscope photograph of a multi-fibre facet [151]. PM – Polarization-maintaining optical fibre.

Here, I propose how such fibre metadevices may be realised. Figure 8-1 shows a schematic illustration of a fibre-optic arrangement where four single-mode polarization-maintaining fibres are coupled together [151]. Each fibre has a metasurface (that can be plasmonic or dielectric) fabricated on its end face. The optical properties or the function of each metasurface can be different from the others. All fibres can be aligned to match the operating polarization of the metasurfaces. Interestingly, such metadevices can contain

metasurfaces optimized for different wavelength ranges. Thus, the user can pick the fibre that corresponds to the desired wavelength. In this way, all-optical functions could be performed at any wavelength across the telecommunication bands. Each fibre could have a pigtailed connector.

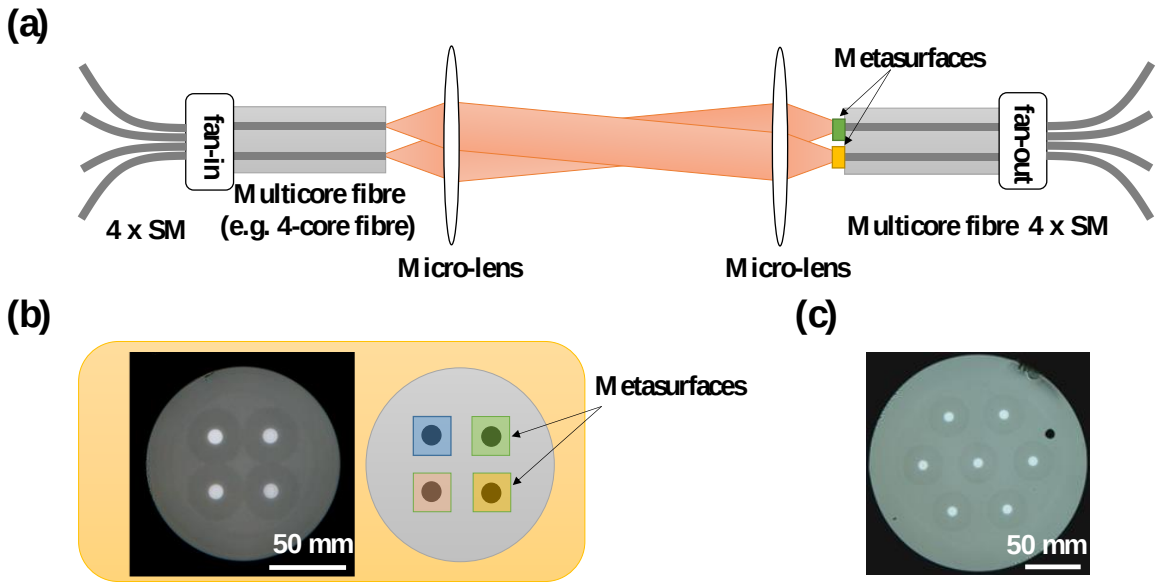

Figure 8-2 **Multi-core single-mode fibre packaging. (a)** The schematic shows four single-mode fibres inserted to a common cladding layer. **(b)** Left: An optical microscope photograph of the end face of an optical fibre with four single-mode cores. Right: A schematic showing how polarization insensitive metasurfaces can be positioned on the cleaved end of the multi-core fibre [151]. **(c)** An optical microscope photograph of a multi-core fibre that contains seven individual single-mode cores. SM – Single-mode fibre

Moreover, for applications that need more than four fibre cores and for metasurfaces that are polarization insensitive one can use multi-core fibres that can have independent pigtail connectors as well. Of course, polarization can be adjusted here as well by placing a free-space polarizer in between the two micro-lenses. Figure 8-2(a) shows a schematic of the fibre-optic packaging, Figure 8-2(b) (left) shows an optical microscope photograph of a four core fibre and (right) a schematic explains how the metasurfaces can be positioned on the cleaved end of the multi-core fibre [151]. Figure 8-2(c) shows an example of a seven core fibre. In Chapter 5, I have shown how metadevices can be cascaded to perform multiple steps of all-optical signal processing. Here this can be done much easier by connecting fibre connectors associated with different cores.

Lastly, multi-core fibre metasurface packages could find applications that exploit other metasurface properties, such as nonlinearity for e.g. second harmonic generation. One can cascade metasurfaces to enhance the overall nonlinear performance. Moreover, such multi-fibre metadevices can considerably decrease the size of the experimental setup (in terms of meters of fibre) and minimize relative phase fluctuation of different signals if they propagate in different cores of the same fibre. Phase fluctuations are associated with thermal expansion of the fibres that always is a drawback of long fibre interferometers.

Appendix A Relative permittivity of gold

Below one can see the real (Figure A-1(a)) and the imaginary (Figure A-1(b)) parts of the complex permittivity of gold from Palik's handbook [49] that I assumed in my calculations (in subsection 2.2.4). For comparison, this is shown alongside the relative permittivity from Johnson-Christy's paper [152] that corresponds to deposited gold films.

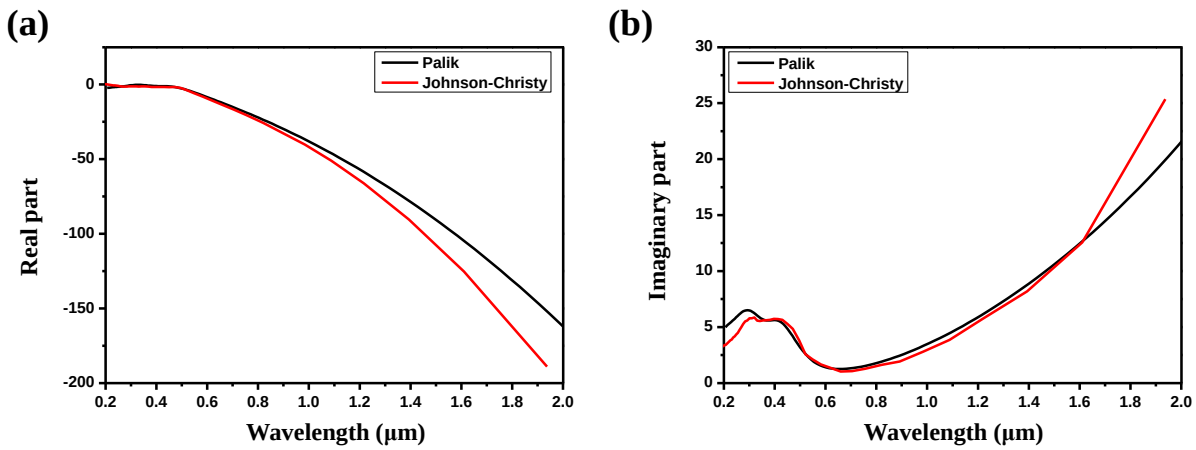

Figure A-1 **Relative permittivity of gold.** The real (a) and imaginary (b) parts of the complex relative permittivity. Black and red lines correspond to data from Palik's handbook [49] and the Johnson-Christy paper [152], respectively.

Appendix B Publications

B.1 Published articles

- **Cryptography in coherent optical information networks using dissipative metamaterial gates**. A. Xomalis, I. Demirtzioglou, Y. Jung, E. Plum, C. Lacava, P. Petropoulos, D. J. Richardson, and N. I. Zheludev. *APL Photonics*, **4**, 046102 (2019) [APL Photonics Editor's Pick]

- **Picosecond all-optical switching and dark pulse generation in a fibre-optic network using a plasmonic metamaterial absorber**. A. Xomalis, I. Demirtzioglou, Y. Jung, E. Plum, C. Lacava, P. Petropoulos, D. J. Richardson, and N. I. Zheludev. *Appl. Phys. Lett.* **113**, 051103 (2018)

- **Fibre-optic metadevice for all-optical signal modulation based on coherent absorption**. A. Xomalis, I. Demirtzioglou, E. Plum, Y. Jung, V. Nalla, C. Lacava, K. F. MacDonald, P. Petropoulos, D. J. Richardson, and N. I. Zheludev. *Nature Communications* **9**, 182 (2018)

- **Nonlinear control of coherent absorption and its optical signal processing applications**. A. Xomalis, Y. Jung, I. Demirtzioglou, C. Lacava, E. Plum, P. Petropoulos, D. J. Richardson, and N. I. Zheludev. *APL Photonics*, in press (2019)

- **Coherent perfect absorption of single photons in a fibre network**. A.N. Vetlugin, R. Guo, A. Xomalis, S. Yanikgonul, G. Adamo, C. Soci, N. I. Zheludev. *Appl. Phys. Lett.*, in press (2019)

- **Coherent fibre network stabilization with single photons and demonstration of all-optical single-photon switching**. S. Yanikgonul, R. Guo, A. Xomalis, A.N. Vetlugin, G. Adamo, C. Soci, N. I. Zheludev. Submitted (2019)

B.2 Conference contributions

- (invited) **Quantum light manipulation with fiberized metamaterial perfect absorber**. A. N. Vetlugin, S. Yanikgonul, R. Guo, A. Xomalis, G. Adamo, C. Soci, and N. I. Zheludev. SPIE Optics & Photonics 2019, San Diego, CA, USA, 11 - 15 Aug 2019

- **Quantum state filtering of dual-rail photons with fiberized plasmonic metamaterial.** S. Yanikgonul, A. N. Vetlugin, R. Guo, A. Xomalis, G. Adamo, C. Soci, and N. I. Zheludev. CLEO 2019, San Jose, CA, USA, 5 - 10 May 2019

- **Coherent fibre network stabilized with single-photons** S. Yanikgonul, R. Guo, A. N. Vetlugin, A. Xomalis, G. Adamo, C. Soci, and N. I. Zheludev. Institute of Physics Singapore (IPS) Meeting 2019, Singapore, 13 - 15 Mar 2019

- **Metamaterial absorber for dual-rail photonic qubit filtering**. A. N. Vetlugin, S. Yanikgonul, R. Guo, A. Xomalis, G. Adamo, C. Soci, and N. I. Zheludev. Institute of Physics Singapore (IPS) Meeting 2019, Singapore, 13 - 15 Mar 2019

- **Coherent cryptography with dissipative all-optical metamaterial gates**. A. Xomalis, I. Demirtzioglou, Y. Jung, E. Plum, C. Lacava, P. Petropoulos, D. J. Richardson, and N. I. Zheludev. Nanometa 2019, Seefeld, Austria, 3 - 6 Jan 2019

- **Filtering of quantum states with plasmonic metamaterial absorber**. A. N. Vetlugin, S. Yanikgonul, R. Guo, A. Xomalis, G. Adamo, C. Soci, and N. I. Zheludev. Nanometa 2019, Seefeld, Austria, 3 - 6 Jan 2019

- (poster) **Optical limiting and noise suppression in fiber network through coherent control of absorption in plasmonic metamaterial**. A. Xomalis, I. Demirtzioglou, Y. Jung, E. Plum, C. Lacava, P. Petropoulos, D. J. Richardson, and N. I. Zheludev. Nanometa 2019, Seefeld, Austria, 3 - 6 Jan 2019

- **Plasmonic coherent perfect absorption and switching in a fiberized quantum network**. A. N. Vetlugin, S. Yanikgonul, A. Xomalis, R. Guo, G. Adamo, C. Soci,

and N. I. Zheludev. Quantum Technology International Conference (QTech), Paris, France, 5 – 7 Sept 2018

- **Coherent perfect absorption and switching in a fiberized quantum network with plasmonic metadevice**. A. N. Vetlugin, R. Guo, A. Xomalis, S. Yanikgonul, G. Adamo, C. Soci, and N. I. Zheludev. Metamaterials 2018, Finland, 27 Aug – 1 Sept 2018

- **A fiberized metadevice for ultrafast all-optical signal processing and picosecond dark pulse generation.** A. Xomalis, I. Demirtzioglou, Y. Jung, E. Plum, C. Lacava, P. Petropoulos, D. J. Richardson, and N. I. Zheludev. Metamaterials 2018, Espoo, Finland, 27 Aug – 1 Sept 2018

- **Stabilized dissipative single-photon switch for fiberized quantum networks**. S. Yanikgonul, R. Guo, A. Xomalis, A. N. Vetlugin, G. Adamo, C. Soci, and N. I. Zheludev. 1st Advances in Quantum Engineering International Meeting (AQE2018), Singapore, 25 – 27 June 2018

- **Fibre-optic metadevice for signal processing with 1 THz bandwidth**. A. Xomalis, I. Demirtzioglou, E. Plum, Y. Jung, C. Lacava, K. F. MacDonald, P. Petropoulos, D. J. Richardson, and N. I. Zheludev. SPIE Photonics Europe 2018, Strasbourg, France, 22-26 Apr 2018

- (poster) **Fully fiberized dissipative single photon switch**. A. N. Vetlugin, S. Yanıkgönül, A. Xomalis, R. Guo, C. Soci, and N. I. Zheludev. Quantum and Topological Nanophotonics (QTN) 2018, Singapore, 5-7 Apr 2018

- **A fiberized metamaterial device for ultrafast control of coherent optical signals**. I. Demirtzioglou, A. Xomalis, E. Plum, Y. Jung, C. Lacava, K. F. MacDonald, P. Petropoulos, D. J. Richardson, and N. I. Zheludev. 2018 Optical Fiber Communication Conference (OFC), San Diego, CA, USA, 11-15 Mar 2018

- (invited) **Coherent information processing on metasurfaces at 40 Gbit/s and beyond**. E. Plum, M. Papaioannou, A. Xomalis, A. Karvounis, V. Nalla, I. Demirtzioglou, Y. Jung, K. F. MacDonald, C. Lacava, P. Petropoulos, D. J. Richardson, and N. I. Zheludev. PIERS 2017, Singapore, Singapore, 19 - 22 Nov 2017

- **Fiber-integrated quantum switch**. N. I. Zheludev, R. Guo, C. M. X. Altuzarra, A. Xomalis, and C. Soci. SPIE Optics & Photonics 2017, San Diego, CA, USA, 06 - 10 Aug 2017

- **Fiber-integrated, ultrafast classical and non-local quantum switches**. R. Guo, C. M. X. Altuzarra, A. Xomalis, Y. Jung, I. Demirtzioglou, E. Plum, K. F. MacDonald, P. Petropoulos, D. J. Richardson, C. Soci, and N. I. Zheludev. SPIE Optics & Photonics 2017, San Diego, CA, USA, 06 - 10 Aug 2017

- (post-deadline) **Fibre-optic metadevice for all-optical coherent signal processing at 40 Gbit/s**. A. Xomalis, I. Demirtzioglou, V. Nalla, E. Plum, Y. Jung, C. Lacava, K. F. MacDonald, P. Petropoulos, D. J. Richardson, and N. I. Zheludev. CLEO-PR, OECC & PGC 2017, Singapore 31 Jul - 4 Aug 2017

- (invited) **Merging metamaterial and optical fiber technologies**. N. I. Zheludev, K. F. MacDonald, E. Plum, A. Karvounis, D. Piccinotti, A. Xomalis, I. Demirtzioglou, V. Savinov, B. Gholipour, Y. Jung, P. Petropoulos, and D. J. Richardson. META2017, Seoul, South Korea, 25 - 28 Jul 2017

- (poster) **Coherent all-optical information processing on metasurfaces**. E. Plum, M. Papaioannou, A. Xomalis, Y. Jung, I. Demirtzioglou, E. T. F. Rogers, K. F. MacDonald, P. Petropoulos, David J. Richardson, and N. I. Zheludev. META2017, Seoul, South Korea, 25 - 28 Jul 2017

- (invited) **Merging photonic metamaterial and optical fiber technologies**. A. Xomalis, D. Piccinotti, A. Karvounis, I. Demirtzioglou, V. Savinov, B. Gholipour, J. Y. Ou, Y. Jung, E. Plum, P. Petropoulos, K. F. MacDonald, D. J. Richardson, and N. I. Zheludev. Integrated Photonics Research, Silicon, and Nano-Photonics, New Orleans, LA, USA, 24 - 27 Jul 2017

- **Dissipative optical switch for coherent fibre networks with 100 THz bandwidth**. A. Xomalis, Y. Jung, I. Demirtzioglou, V. Nalla, E. Plum, K. F. MacDonald, P. Petropoulos, D. J. Richardson, and N. I. Zheludev. CLEO Europe - EQEC 2017 , Munich, Germany 25 - 29 Jun 2017

- (invited) **Merging metamaterial and fiber technologies**. J. Y. Ou, A. Karvounis, A. Xomalis, V. Savinov, E. Plum, K. F. MacDonald, and N. I. Zheludev. 8th

International Conference on Surface Plasmon Photonics (SPP8), Taipei, Taiwan, 22-26 May 2017

- (invited) **Active metasurfaces: Optical properties on demand**. E. Plum, M. Papaioannou, P. Cencillo-Abad, J. Y. Ou, A. Xomalis, E. T. F. Rogers, K. F. MacDonald, and N. I. Zheludev. Rank Prize Symposium on Electromagnetic Metasurfaces, Grasmere, UK, 13 - 16 Mar 2017

- (poster) **Fibre-integrated metadevice for all-optical data processing**. A. Xomalis, Y. Jung, E. Plum, K. F. MacDonald, and N. I. Zheludev. International Workshop on Emerging Applications of Optical Nanostructures, Tel Aviv, Israel, 19 - 23 Feb 2017

- **Fibre-coupled photonic metadevices**. A. Xomalis, D. Piccinotti, A. Karvounis, H. Zhang, V. Savinov, B. Gholipour, Y. Jung, A. C. Peacock, E. Plum, K. F. MacDonald, D. J. Richardson, and N. I. Zheludev. Nanometa 2017, Seefeld, Austria, 4 - 7 Jan 2017

List of References

1. A. Alù and N. Engheta, "Achieving transparency with plasmonic and metamaterial coatings," Physical Review E **72**, 016623 (2005).

2. G. Dolling, M. Wegener, C. M. Soukoulis, and S. Linden, "Negative-index metamaterial at 780 nm wavelength," Optics letters **32**, 53-55 (2007).

3. J. K. Gansel, M. Thiel, M. S. Rill, M. Decker, K. Bade, V. Saile, G. von Freymann, S. Linden, and M. Wegener, "Gold helix photonic metamaterial as broadband circular polarizer," Science **325**, 1513-1515 (2009).

4. C. Pfeiffer and A. Grbic, "Metamaterial Huygens' surfaces: tailoring wave fronts with reflectionless sheets," Physical review letters **110**, 197401 (2013).

5. J. Valentine, S. Zhang, T. Zentgraf, E. Ulin-Avila, D. A. Genov, G. Bartal, and X. Zhang, "Three-dimensional optical metamaterial with a negative refractive index," nature **455**, 376 (2008).

6. V. Veselago, "Electrodynamics of substances with simultaneously negative ε and μ," Usp. Fiz. Nauk **92**, 517 (1967).

7. R. A. Shelby, D. R. Smith, and S. Schultz, "Experimental verification of a negative index of refraction," Science **292**, 77-79 (2001).

8. N. I. Zheludev, "What diffraction limit?," Nature Materials **7**, 420 (2008).

9. J. B. Pendry, A. J. Holden, D. J. Robbins, and W. Stewart, "Magnetism from conductors and enhanced nonlinear phenomena," IEEE transactions on microwave theory and techniques **47**, 2075-2084 (1999).

10. D. R. Smith, J. B. Pendry, and M. C. Wiltshire, "Metamaterials and negative refractive index," Science **305**, 788-792 (2004).

11. J. B. Pendry, "Negative refraction makes a perfect lens," Physical review letters **85**, 3966 (2000).

12. J. B. Pendry, D. Schurig, and D. R. Smith, "Controlling electromagnetic fields," Science **312**, 1780-1782 (2006).

13. U. Leonhardt and D. R. Smith, "Focus on cloaking and transformation optics," New Journal of Physics **10**, 115019 (2008).

14. E. Plum, V. Fedotov, and N. Zheludev, "Asymmetric transmission: a generic property of two-dimensional periodic patterns," Journal of Optics **13**, 024006 (2010).

15. G. Kenanakis, A. Xomalis, A. Selimis, M. Vamvakaki, M. Farsari, M. Kafesaki, C. M. Soukoulis, and E. N. Economou, "Three-dimensional infrared metamaterial with asymmetric transmission," ACS Photonics **2**, 287-294 (2015).

16. G. Li, S. Zhang, and T. Zentgraf, "Nonlinear photonic metasurfaces," Nature Reviews Materials **2**, 17010 (2017).

17. A. S. Schwanecke, V. Fedotov, V. Khardikov, S. Prosvirnin, Y. Chen, and N. Zheludev, "Optical magnetic mirrors," Journal of Optics A: Pure and Applied Optics **9**, L1 (2006).

18. T. Driscoll, H.-T. Kim, B.-G. Chae, B.-J. Kim, Y.-W. Lee, N. M. Jokerst, S. Palit, D. R. Smith, M. Di Ventra, and D. N. Basov, "Memory Metamaterials," Science **325**, 1518 (2009).

19. B. Gholipour, J. Zhang, K. F. MacDonald, D. W. Hewak, and N. I. Zheludev, "An All-Optical, Non-volatile, Bidirectional, Phase-Change Meta-Switch," Advanced Materials **25**, 3050-3054 (2013).

20. Z. L. Sámson, K. F. MacDonald, F. De Angelis, B. Gholipour, K. Knight, C. C. Huang, E. Di Fabrizio, D. W. Hewak, and N. I. Zheludev, "Metamaterial electro-optic switch of nanoscale thickness," Applied Physics Letters **96**, 143105 (2010).

21. A. Tittl, A.-K. U. Michel, M. Schäferling, X. Yin, B. Gholipour, L. Cui, M. Wuttig, T. Taubner, F. Neubrech, and H. Giessen, "A Switchable Mid-Infrared Plasmonic Perfect Absorber with Multispectral Thermal Imaging Capability," Advanced Materials **27**, 4597-4603 (2015).

22. A. Karvounis, B. Gholipour, K. F. MacDonald, and N. I. Zheludev, "All-dielectric phase-change reconfigurable metasurface," Applied Physics Letters **109**, 051103 (2016).

23. N. I. Zheludev and E. Plum, "Reconfigurable nanomechanical photonic metamaterials," Nature Nanotechnology **11**, 16 (2016).

24. J. Y. Ou, E. Plum, L. Jiang, and N. I. Zheludev, "Reconfigurable Photonic Metamaterials," Nano Letters **11**, 2142-2144 (2011).

25. J. Valente, J.-Y. Ou, E. Plum, I. J. Youngs, and N. I. Zheludev, "Reconfiguring photonic metamaterials with currents and magnetic fields," Applied Physics Letters **106**, 111905 (2015).

26. J. Valente, J.-Y. Ou, E. Plum, I. J. Youngs, and N. I. Zheludev, "A magneto-electro-optical effect in a plasmonic nanowire material," Nature communications **6**, 7021 (2015).

27. J. Y. Ou, E. Plum, J. Zhang, and N. I. Zheludev, "Giant nonlinearity of an optically reconfigurable plasmonic metamaterial," Advanced Materials **28**, 729-733 (2016).

28. O. Buchnev, J. Y. Ou, M. Kaczmarek, N. I. Zheludev, and V. A. Fedotov, "Electro-optical control in a plasmonic metamaterial hybridised with a liquid-crystal cell," Optics Express **21**, 1633-1638 (2013).

29. A. Minovich, J. Farnell, D. N. Neshev, I. McKerracher, F. Karouta, J. Tian, D. A. Powell, I. V. Shadrivov, H. H. Tan, C. Jagadish, and Y. S. Kivshar, "Liquid crystal based nonlinear fishnet metamaterials," Applied Physics Letters **100**, 121113 (2012).

30. D. G. Baranov, A. Krasnok, T. Shegai, A. Alù, and Y. Chong, "Coherent perfect absorbers: linear control of light with light," Nature Reviews Materials **2**, 17064 (2017).

31. E. Plum, K. F. MacDonald, X. Fang, D. Faccio, and N. I. Zheludev, "Controlling the Optical Response of 2D Matter in Standing Waves," ACS Photonics **4**, 3000-3011 (2017).

32. C. Lacava, M. J. Strain, P. Minzioni, I. Cristiani, and M. Sorel, "Integrated nonlinear Mach Zehnder for 40 Gbit/s all-optical switching," Optics Express **21**, 21587-21595 (2013).

33. C. Lacava, S. Stankovic, A. Z. Khokhar, T. D. Bucio, F. Y. Gardes, G. T. Reed, D. J. Richardson, and P. Petropoulos, "Si-rich Silicon Nitride for Nonlinear Signal Processing Applications," Scientific Reports **7**, 22 (2017).

34. Q. Xu and M. Lipson, "All-optical logic based on silicon micro-ring resonators," Optics Express **15**, 924 (2007).

35. T. Roger, S. Vezzoli, E. Bolduc, J. Valente, J. J. F. Heitz, J. Jeffers, C. Soci, J. Leach, C. Couteau, N. I. Zheludev, and D. Faccio, "Coherent perfect absorption in deeply subwavelength films in the single-photon regime," Nat. Commun. **6**, 7031 (2015).

36. V. Nalla, J. Valente, H. Sun, and N. I. Zheludev, "11-fs dark pulses generated via coherent absorption in plasmonic metamaterial," Opt. Express **25**, 22620-22625 (2017).

37. E. Hecht, *Optics* (Addison-Wesley, 2002).

38. L. E. Huygens C, Mewes R. , *Abhandlung Über Das Licht: Worin Die Ursachen Der Vorgänge Bei Seiner Zurückwerfung Und Brechung Und Besonders Bei Der Eigenthümlichen Brechung Des Isländischen Spathes Dargelegt Sind.* (BiblioBazaar, 2010 [reprint]).

39. X. Fang, M. Lun Tseng, J.-Y. Ou, K. F. MacDonald, D. Ping Tsai, and N. I. Zheludev, "Ultrafast all-optical switching via coherent modulation of metamaterial absorption," Applied Physics Letters **104**, 141102 (2014).

40. X. Fang, M. L. Tseng, D. P. Tsai, and N. I. Zheludev, "Coherent excitation-selective spectroscopy of multipole resonances," Physical Review Applied **5**, 014010 (2016).

41. S. A. Mousavi, E. Plum, J. Shi, and N. I. Zheludev, "Coherent control of birefringence and optical activity," Applied Physics Letters **105**, 011906 (2014).

42. J. Shi, X. Fang, E. T. Rogers, E. Plum, K. F. MacDonald, and N. I. Zheludev, "Coherent control of Snell's law at metasurfaces," Optics express **22**, 21051-21060 (2014).

43. S. A. Mousavi, E. Plum, J. Shi, and N. I. Zheludev, "Coherent control of optical polarization effects in metamaterials," Scientific reports **5**, 8977 (2015).

44. S. Thongrattanasiri, F. H. Koppens, and F. J. G. De Abajo, "Complete optical absorption in periodically patterned graphene," Physical review letters **108**, 047401 (2012).

45. C. Hägglund, S. P. Apell, and B. Kasemo, "Maximized optical absorption in ultrathin films and its application to plasmon-based two-dimensional photovoltaics," Nano letters **10**, 3135-3141 (2010).

46. T. V. Teperik, F. G. De Abajo, A. Borisov, M. Abdelsalam, P. Bartlett, Y. Sugawara, and J. Baumberg, "Omnidirectional absorption in nanostructured metal surfaces," Nature photonics **2**, 299 (2008).

47. E. Plum, K. Tanaka, W. T. Chen, V. A. Fedotov, D. P. Tsai, and N. Zheludev, "A combinatorial approach to metamaterials discovery," Journal of Optics **13**, 055102 (2011).

48. J. Zhang, K. F. MacDonald, and N. I. Zheludev, "Controlling light-with-light without nonlinearity," Light Sci. Appl. **1**, e18 (2012).

49. E. D. Palik, *Handbook of optical constants of solids* (Academic press, 1998), Vol. 3.

50. A. Xomalis, I. Demirtzioglou, E. Plum, Y. Jung, V. Nalla, C. Lacava, K. F. MacDonald, P. Petropoulos, D. J. Richardson, and N. I. Zheludev, "Fibre-optic metadevice for all-optical signal modulation based on coherent absorption," Nat. Commun. **9**, 182 (2018).

51. P. Singh, D. K. Tripathi, S. Jaiswal, and H. Dixit, "All-optical logic gates: designs, classification, and comparison," Advances in Optical Technologies **2014**(2014).

52. R. W. Boyd, *Nonlinear optics* (Elsevier, 2003).

53. V. R. Almeida, C. A. Barrios, R. R. Panepucci, and M. Lipson, "All-optical control of light on a silicon chip," Nature **431**, 1081 (2004).

54. K. Nozaki, T. Tanabe, A. Shinya, S. Matsuo, T. Sato, H. Taniyama, and M. Notomi, "Sub-femtojoule all-optical switching using a photonic-crystal nanocavity," Nature Photonics **4**, 477 (2010).

55. A. E. Willner, S. Khaleghi, M. R. Chitgarha, and O. F. Yilmaz, "All-optical signal processing," Journal of Lightwave Technology **32**, 660-680 (2014).

56. X. Fang, K. F. MacDonald, and N. I. Zheludev, "Controlling light with light using coherent metadevices: all-optical transistor, summator and invertor," Light Sci. Appl. **4**, e292 (2015).

57. G. Pirruccio and J. G. Rivas, "Modulated light absorption and emission of a luminescent layer by phase-controlled multiple beam illumination," Optics express **23**, 18166-18180 (2015).

58. G. Pirruccio, M. Ramezani, S. R.-K. Rodriguez, and J. G. Rivas, "Coherent control of the optical absorption in a plasmonic lattice coupled to a luminescent layer," Physical review letters **116**, 103002 (2016).

59. S. Kita, K. Takata, M. Ono, K. Nozaki, E. Kuramochi, K. Takeda, and M. Notomi, "Coherent control of high efficiency metasurface beam deflectors with a back partial reflector," APL Photonics **2**, 046104 (2017).

60. S. M. Rao, A. Lyons, T. Roger, M. Clerici, N. I. Zheludev, and D. Faccio, "Geometries for the coherent control of four-wave mixing in graphene multilayers," Sci. Rep. **5**, 15399 (2015).

61. T. Roger, S. Restuccia, A. Lyons, D. Giovannini, J. Romero, J. Jeffers, M. Padgett, and D. Faccio, "Coherent absorption of N00N states," Physical review letters **117**, 023601 (2016).

62. C. Altuzarra, S. Vezzoli, J. Valente, W. Gao, C. Soci, D. Faccio, and C. Couteau, "Coherent perfect absorption in metamaterials with entangled photons," ACS Photonics **4**, 2124-2128 (2017).

63. M. Papaioannou, E. Plum, J. Valente, E. T. Rogers, and N. I. Zheludev, "Two-dimensional control of light with light on metasurfaces," Light: Science & Applications **5**, e16070 (2016).

64. M. Papaioannou, E. Plum, J. Valente, E. T. Rogers, and N. I. Zheludev, "All-optical multichannel logic based on coherent perfect absorption in a plasmonic metamaterial," APL Photonics **1**, 090801 (2016).

65. E. Plum and N. Zheludev, "Chirality and anisotropy of planar metamaterials," (2011).

66. S. M. Rao, J. J. Heitz, T. Roger, N. Westerberg, and D. Faccio, "Coherent control of light interaction with graphene," Optics letters **39**, 5345-5347 (2014).

67. X. Fang, K. F. MacDonald, and N. I. Zheludev, "Controlling Light with Light via Interference on Photonic Metamaterials," in *Quantum Photonics: Pioneering Advances and Emerging Applications* (Springer, 2019), pp. 239-265.

68. M. Nakazawa, K. Kikuchi, and T. Miyazaki, *High spectral density optical communication technologies* (Springer Science & Business Media, 2010), Vol. 6.

69. R. Slavík, F. Parmigiani, J. Kakande, C. Lundström, M. Sjödin, P. A. Andrekson, R. Weerasuriya, S. Sygletos, A. D. Ellis, and L. Grüner-Nielsen, "All-optical phase and amplitude regenerator for next-generation telecommunications systems," Nature Photonics **4**, 690 (2010).

70. D. E. Crivelli, M. R. Hueda, H. S. Carrer, M. Del Barco, R. R. López, P. Gianni, J. M. Finochietto, N. Swenson, P. Voois, and O. E. Agazzi, "Architecture of a Single-Chip 50 Gb/s DP-QPSK/BPSK Transceiver With Electronic Dispersion Compensation for Coherent Optical Channels," IEEE Trans. on Circuits and Systems **61**, 1012-1025 (2014).

71. P. Dong, X. Liu, S. Chandrasekhar, L. L. Buhl, R. Aroca, and Y.-K. Chen, "Monolithic silicon photonic integrated circuits for compact 100$^{+} $ Gb/s coherent optical receivers and transmitters," IEEE Journal of Selected Topics in Quantum Electronics **20**, 1-8 (2014).

72. A. Xomalis, I. Demirtzioglou, Y. Jung, E. Plum, C. Lacava, P. Petropoulos, D. J. Richardson, and N. I. Zheludev, "Cryptography in coherent optical information networks using dissipative metamaterial gates," APL Photonics **4**, 046102 (2019).

73. J. Zeng, X. Wang, J. Sun, A. Pandey, A. N. Cartwright, and N. M. Litchinitser, "Manipulating complex light with metamaterials," Scientific reports **3**, 2826 (2013).

74. N. Yu and F. Capasso, "Optical metasurfaces and prospect of their applications including fiber optics," Journal of Lightwave Technology **33**, 2344-2358 (2015).

75. M. Principe, M. Consales, A. Micco, A. Crescitelli, G. Castaldi, E. Esposito, V. La Ferrara, A. Cutolo, V. Galdi, and A. Cusano, "Optical fiber meta-tips," Light: Science & Applications **6**, e16226 (2017).

76. A. Xomalis, I. Demirtzioglou, Y. Jung, E. Plum, C. Lacava, P. Petropoulos, D. J. Richardson, and N. I. Zheludev, "Picosecond all-optical switching and dark pulse

generation in a fibre-optic network using a plasmonic metamaterial absorber," Appl. Phys. Lett. **113**, 051103 (2018).

77. G. Agrawal, *Nonlinear Fiber Optics* (Elsevier Science, 2012).

78. D. Cotter, R. Manning, K. Blow, A. Ellis, A. Kelly, D. Nesset, I. Phillips, A. Poustie, and D. Rogers, "Nonlinear optics for high-speed digital information processing," Science **286**, 1523-1528 (1999).

79. C. Lacava, M. Ettabib, and P. Petropoulos, "Nonlinear silicon photonic signal processing devices for future optical networks," Applied Sciences **7**, 103 (2017).

80. D. Krökel, N. Halas, G. Giuliani, and D. Grischkowsky, "Dark-pulse propagation in optical fibers," Physical review letters **60**, 29 (1988).

81. D. Meshulach and Y. Silberberg, "Coherent quantum control of two-photon transitions by a femtosecond laser pulse," Nature **396**, 239 (1998).

82. J. Zimmermann, S. T. Cundiff, G. von Plessen, J. Feldmann, M. Arzberger, G. Böhm, M.-C. Amann, and G. Abstreiter, "Dark pulse formation in a quantum-dot laser," Applied Physics Letters **79**, 18-20 (2001).

83. H. Zhang, D. Tang, L. Zhao, and X. Wu, "Dark pulse emission of a fiber laser," Physical Review A **80**, 045803 (2009).

84. M. Feng, K. L. Silverman, R. P. Mirin, and S. T. Cundiff, "Dark pulse quantum dot diode laser," Optics express **18**, 13385-13395 (2010).

85. X. Li, S. Zhang, Y. Meng, and Y. Hao, "Harmonic mode locking counterparts of dark pulse and dark-bright pulse pairs," Optics express **21**, 8409-8416 (2013).

86. H. Liu and K. Chow, "Dark pulse generation in fiber lasers incorporating carbon nanotubes," Optics express **22**, 29708-29713 (2014).

87. W. Liu, L. Pang, H. Han, W. Tian, H. Chen, M. Lei, P. Yan, and Z. Wei, "Generation of dark solitons in erbium-doped fiber lasers based Sb 2 Te 3 saturable absorbers," Optics express **23**, 26023-26031 (2015).

88. X. Xue, "X. Xue, Y. Xuan, Y. Liu, P.-H. Wang, S. Chen, J. Wang, DE Leaird, M. Qi, and AM Weiner, Nat. Photonics 9, 594 (2015)," Nat. Photonics **9**, 594 (2015).

89. J. Liu, X. Li, S. Zhang, H. Zhang, P. Yan, M. Han, Z. Pang, and Z. Yang, "Polarization domain wall pulses in a microfiber-based topological insulator fiber laser," Scientific reports **6**, 29128 (2016).

90. A. Hasegawa and F. Tappert, "Transmission of stationary nonlinear optical pulses in dispersive dielectric fibers. II. Normal dispersion," Applied Physics Letters **23**, 171-172 (1973).

91. A. Weiner, J. Heritage, R. Hawkins, R. Thurston, E. Kirschner, D. Leaird, and W. Tomlinson, "Experimental observation of the fundamental dark soliton in optical fibers," Physical review letters **61**, 2445 (1988).

92. A. Weiner, R. Thurston, W. Tomlinson, J. Heritage, D. Leaird, E. Kirschner, and R. Hawkins, "Temporal and spectral self-shifts of dark optical solitons," Optics letters **14**, 868-870 (1989).

93. W. Zhao and E. Bourkoff, "Propagation properties of dark solitons," Optics letters **14**, 703-705 (1989).

94. I. Kaminow, "Polarization in optical fibers," IEEE Journal of Quantum Electronics **17**, 15-22 (1981).

95. Y. S. Kivshar and B. Luther-Davies, "Dark optical solitons: physics and applications," Physics reports **298**, 81-197 (1998).

96. R. Schoenlein, S. Chattopadhyay, H. Chong, T. Glover, P. Heimann, C. Shank, A. Zholents, and M. Zolotorev, "Generation of femtosecond pulses of synchrotron radiation," Science **287**, 2237-2240 (2000).

97. F. Miller, *Telegraphic code to insure privacy and secrecy in the transmission of telegrams* (C.M. Cornwell, New York, 1882).

98. G. S. Vernam, "Secret signaling system," Secret signaling system **US1310719A** (1919).

99. G. S. Vernam, "Cipher printing telegraph systems: For secret wire and radio telegraphic communications," Journal of the A.I.E.E. **45**, 109-115 (1926).

100. D. R. Stinson, *Cryptography: theory and practice* (CRC press, 2005).

101. C. E. Shannon, "Communication Theory of Secrecy Systems," Bell Syst. Tech. J. **28**, 656-715 (1949).

102. W. Tuchman, "A brief history of the data encryption standard," in *Internet besieged*, E. D. Dorothy and J. D. Peter, eds. (ACM Press/Addison-Wesley Publishing Co., 1998), pp. 275-280.

103. J. Daemen and V. Rijmen, *The design of Rijndael: AES-the advanced encryption standard* (Springer Science & Business Media, 2013).

104. D. Bouwmeester, A. K. Ekert, and A. Zeilinger, *The physics of quantum information: quantum cryptography, quantum teleportation and quantum computation* (Springer Science & Business Media, 2013).

105. C. H. Bennett and G. Brassard, "Quantum cryptography: Public key distribution and coin tossing," Theor. Comput. Sci. **560**, 7-11 (2014).

106. P. W. Shor and J. Preskill, "Simple Proof of Security of the BB84 Quantum Key Distribution Protocol," Phys. Rev. Lett. **85**, 441-444 (2000).

107. R. L. Rivest, A. Shamir, and L. Adleman, "A method for obtaining digital signatures and public-key cryptosystems," Commun. ACM **21**, 120-126 (1978).

108. M. P. Fok, Z. Wang, Y. Deng, and P. R. Prucnal, "Optical Layer Security in Fiber-Optic Networks," IEEE Trans. Inf. Forensics Secur. **6**, 725-736 (2011).

109. A. Argyris, D. Syvridis, L. Larger, V. Annovazzi-Lodi, P. Colet, I. Fischer, J. García-Ojalvo, C. R. Mirasso, L. Pesquera, and K. A. Shore, "Chaos-based communications at high bit rates using commercial fibre-optic links," Nature **438**, 343 (2005).

110. B. Wu, Z. Wang, Y. Tian, M. P. Fok, B. J. Shastri, D. R. Kanoff, and P. R. Prucnal, "Optical steganography based on amplified spontaneous emission noise," Opt. Express **21**, 2065-2071 (2013).

111. J. A. Salehi, "Code division multiple-access techniques in optical fiber networks. I. Fundamental principles," IEEE Trans. Comm. **37**, 824-833 (1989).

112. P. C. Teh, P. Petropoulos, M. Ibsen, and D. J. Richardson, "Phase encoding and decoding of short pulses at 10 Gb/s using superstructured fiber Bragg gratings," IEEE Photon. Tech. Lett. **13**, 154-156 (2001).

113. P. R. Prucnal, *Optical Code Division Multiple Access: Fundamentals and Applications* (CRC Press, 2005).

114. K. Kikuchi, "Fundamentals of Coherent Optical Fiber Communications," J. Lightwave Technol. **34**, 157-179 (2016).

115. F. Buchali, F. Steiner, G. Böcherer, L. Schmalen, P. Schulte, and W. Idler, "Rate Adaptation and Reach Increase by Probabilistically Shaped 64-QAM: An Experimental Demonstration," J. Lightwave Technol. **34**, 1599-1609 (2016).

116. G. Rademacher, R. S. Luís, B. J. Puttnam, T. A. Eriksson, E. Agrell, R. Maruyama, K. Aikawa, H. Furukawa, Y. Awaji, and N. Wada, "159 Tbit/s C+L Band Transmission over 1045 km 3-Mode Graded-Index Few-Mode Fiber," Optical Fiber Communication Conference (OFC) (Postdeadline Papers) Th4C.4 (2018).

117. L.-S. Ma, P. Jungner, J. Ye, and J. L. Hall, "Delivering the same optical frequency at two places: accurate cancellation of phase noise introduced by an optical fiber or other time-varying path," Opt. Lett. **19**, 1777-1779 (1994).

118. S. L. Jansen, I. Morita, T. C. W. Schenk, N. Takeda, and H. Tanaka, "Coherent Optical 25.8-Gb/s OFDM Transmission Over 4160-km SSMF," J. Lightwave Technol. **26**, 6-15 (2008).

119. Y. Ma, Q. Yang, Y. Tang, S. Chen, and W. Shieh, "1-Tb/s single-channel coherent optical OFDM transmission over 600-km SSMF fiber with subwavelength bandwidth access," Opt. Express **17**, 9421-9427 (2009).

120. E. Temprana, E. Myslivets, B. P. P. Kuo, L. Liu, V. Ataie, N. Alic, and S. Radic, "Overcoming Kerr-induced capacity limit in optical fiber transmission," Science **348**, 1445 (2015).

121. I. Kanter, Y. Aviad, I. Reidler, E. Cohen, and M. Rosenbluh, "An optical ultrafast random bit generator," Nat. Photonics **4**, 58 (2009).

122. H. Rong, Y.-H. Kuo, A. Liu, M. Paniccia, and O. Cohen, "High efficiency wavelength conversion of 10 Gb/s data in silicon waveguides," Optics Express **14**, 1182-1188 (2006).

123. M. A. Foster, A. C. Turner, J. E. Sharping, B. S. Schmidt, M. Lipson, and A. L. Gaeta, "Broad-band optical parametric gain on a silicon photonic chip," Nature **441**, 960-963 (2006).

124. R. Salem, M. A. Foster, A. C. Turner, D. F. Geraghty, M. Lipson, and A. L. Gaeta, "Signal regeneration using low-power four-wave mixing on silicon chip," Nature Photonics **2**, 35 (2007).

125. R.-J. Essiambre, G. J. Foschini, G. Kramer, and P. J. Winzer, "Capacity limits of information transport in fiber-optic networks," Phys. Rev. Lett. **101**, 163901 (2008).

126. S. Lloyd, "Capacity of the noisy quantum channel," Phys. Rev. A **55**, 1613 (1997).

127. C. E. Shannon, "Communication in the presence of noise," Proceedings of the IEEE **86**, 447-457 (1998).

128. C. E. Shannon, "A mathematical theory of communication," Bell system technical journal **27**, 379-423 (1948).

129. D. Hillerkuss, R. Schmogrow, T. Schellinger, M. Jordan, M. Winter, G. Huber, T. Vallaitis, R. Bonk, P. Kleinow, and F. Frey, "26 Tbit s− 1 line-rate super-channel transmission utilizing all-optical fast Fourier transform processing," Nature photonics **5**, 364 (2011).

130. D. Hillerkuss, M. Winter, M. Teschke, A. Marculescu, J. Li, G. Sigurdsson, K. Worms, S. Ben Ezra, N. Narkiss, W. Freude, and J. Leuthold, "Simple all-optical FFT scheme enabling Tbit/s real-time signal processing," Optics Express **18**, 9324-9340 (2010).

131. H. S. Chung, H. Park, and K. J. Kim, "Apparatus and method for reducing signal noise and OCDMA receiver and method," US20070097854A1 (2008).

132. S. Jacobs, M. Sargent III, J. F. Scott, and M. O. Scully, "Laser applications to optics and spectroscopy," Laser Applications to Optics and Spectroscopy (1975).

133. S. J. Wawilow and W. L. Lewschin, "Die Beziehungen zwischen Fluoreszenz und Phosphoreszenz in festen und flüssigen Medien," Z. Physik **35**, 920-936 (1926).

134. U. Keller, K. J. Weingarten, F. X. Kartner, D. Kopf, B. Braun, I. D. Jung, R. Fluck, C. Honninger, N. Matuschek, and J. A. Der Au, "Semiconductor saturable absorber mirrors (SESAM's) for femtosecond to nanosecond pulse generation in solid-state lasers," IEEE J. Sel. Top. Quantum Electron. **2**, 435-453 (1996).

135. P. Guerreiro, S. Ten, N. Borrelli, J. Butty, G. Jabbour, and N. Peyghambarian, "PbS quantum-dot doped glasses as saturable absorbers for mode locking of a Cr: forsterite laser," Appl. Phys. Lett. **71**, 1595-1597 (1997).

136. S. Y. Set, H. Yaguchi, Y. Tanaka, and M. Jablonski, "Laser mode locking using a saturable absorber incorporating carbon nanotubes," J. Lightwave Technol. **22**, 51 (2004).

137. A. Martinez and S. Yamashita, "Multi-gigahertz repetition rate passively modelocked fiber lasers using carbon nanotubes," Opt. Express **19**, 6155-6163 (2011).

138. V. V. Dvoyrin, V. Mashinsky, and E. Dianov, "Yb-Bi pulsed fiber lasers," Opt. Lett. **32**, 451-453 (2007).

139. S. Kawata, H.-B. Sun, T. Tanaka, and K. Takada, "Finer features for functional microdevices," Nature **412**, 697 (2001).

140. F. Helmchen and W. Denk, "Deep tissue two-photon microscopy," Nature Methods **2**, 932 (2005).

141. M. Ren, B. Jia, J. Y. Ou, E. Plum, J. Zhang, K. F. MacDonald, A. E. Nikolaenko, J. Xu, M. Gu, and N. I. Zheludev, "Nanostructured plasmonic medium for terahertz bandwidth all-optical switching," Adv. Mater. **23**, 5540-5544 (2011).

142. A. Hayat, A. Nevet, P. Ginzburg, and M. Orenstein, "Applications of two-photon processes in semiconductor photonic devices: invited review," Semicond. Sci. Technol. **26**, 083001 (2011).

143. M. Pu, Q. Feng, M. Wang, C. Hu, C. Huang, X. Ma, Z. Zhao, C. Wang, and X. Luo, "Ultrathin broadband nearly perfect absorber with symmetrical coherent illumination," Opt. Express **20**, 2246-2254 (2012).

144. N. Doran and D. Wood, "Nonlinear-optical loop mirror," Opt. Lett. **13**, 56-58 (1988).

145. T. Sakamoto, F. Futami, K. Kikuchi, S. Takeda, Y. Sugaya, and S. Watanabe, "All-optical wavelength conversion of 500-fs pulse trains by using a nonlinear-optical loop mirror composed of a highly nonlinear DSF," IEEE Photon. Technol. Lett. **13**, 502-504 (2001).

146. G. B. Xavier and J. P. von der Weid, "Stable single-photon interference in a 1 km fiber-optic Mach–Zehnder interferometer with continuous phase adjustment," Optics Letters **36**, 1764-1766 (2011).

147. S.-B. Cho and H. Kim, "Active stabilization of a fiber-optic two-photon interferometer using continuous optical length control," Optics Express **24**, 10980-10986 (2016).

148. S.-B. Cho and T.-G. Noh, "Stabilization of a long-armed fiber-optic single-photon interferometer," Optics Express **17**, 19027-19032 (2009).

149. S. M. Barnett, J. Jeffers, A. Gatti, and R. Loudon, "Quantum optics of lossy beam splitters," Physical Review A **57**, 2134-2145 (1998).

150. J. Jeffers, "Interference and the lossless lossy beam splitter," Journal of Modern Optics **47**, 1819-1824 (2000).

151. Y. Jung, J. Hayes, S.-U. Alam, and D. Richardson, "Multicore fibre fan-in/fan-out device using fibre optic collimators," in *2017 European Conference on Optical Communication (ECOC)*, (IEEE, 2017), 1-3.

152. P. B. Johnson and R.-W. Christy, "Optical constants of the noble metals," Physical review B **6**, 4370 (1972).